NEAR-FIELD THERMAL RADIATIVE EMISSION OF MATERIALS DEMONSTRATING NEAR INFRARED SURFACE POLARITON RESONANCE

by

Spencer Justin Petersen

A dissertation submitted to the faculty of
The University of Utah
in partial fulfillment of the requirements of the degree of

Doctor of Philosophy

Department of Mechanical Engineering

The University of Utah

December 2016

The University of Utah Graduate School

STATEMENT OF DISSERTATION APPROVAL

The dissertation of **Spencer Justin Petersen**

has been approved by the following supervisory committee members:

Mathieu Francoeur	, Chair	**9 Sept. 2016** Date Approved
Bart Raeymaekers	, Member	**9 Sept. 2016** Date Approved
Timothy A. Ameel	, Member	**9 Sept. 2016** Date Approved
David Alan Schurig	, Member	**9 Sept. 2016** Date Approved
Soumyadipta Basu	, Member	**18 Sept. 2016** Date Approved

and by **Timothy A. Ameel** , Chair/Dean of

the Department/College/School of **Mechanical Engineering**

and by David B. Kieda, Dean of The Graduate School.

ABSTRACT

Surface polariton mediated near-field radiative transfer exceeds the blackbody limit by orders of magnitude and is quasimonochromatic. Thermophotovoltaic (TPV) power generation consists of converting thermal radiation into useful electrical energy and exhibits a peak performance near the TPV cell bandgap, which is typically located within the near infrared bandwidth. Therefore, an ideal emission source for a nanoscale gap TPV device, in which the emitter and cell are separated by no more than one peak emitted wavelength, will sustain surface polariton resonance at or near the TPV cell bandgap in the near infrared. To date, few materials have been identified that satisfy this requirement.

The first objective of this dissertation is to theoretically explore dielectric Mie resonance-based (DMRB) electromagnetic metamaterials for the potential to sustain near infrared surface polariton resonance. Electromagnetic metamaterials are composite media, consisting of subwavelength, repeating unit structures called “meta-atoms.” The microscopic configuration of the meta-atom can be engineered, dictating the effective macroscale electromagnetic properties of the bulk metamaterial, including the surface polariton resonance wavelength. DMRB metamaterials consist of dielectric nanoparticles within a host medium and are analyzed using an effective medium theory. The local density of electromagnetic states, an indicator of possibly harvestable energy near an emitting surface, is calculated for two DMRB metamaterials: spherical nanoparticles of

1) silicon carbide, and 2) silicon embedded in a host medium. Results show that the surface polariton resonance of these metamaterials is tunable and, for the silicon metamaterial only, is found in the near infrared bandwidth, making it a viable candidate for use in a nano-TPV device.

In order to demonstrate the practicality thereof, the second objective is to fabricate and characterize DMRB metamaterials. Specimens are fabricated by hand mixing and sonicating nanoparticles with two part epoxy resins. Transmission measurements of the specimens reveal divergence from the theoretical predictions. Microscopic inspection suggests insufficient nanoparticle dispersion within the host resin medium. All results indicate that enhanced fabrication techniques must be developed to improve nanoparticle dispersion in DMRB metamaterials prior to further electromagnetic characterization.

The lack of success with the second objective drives a third: theoretically explore various forms of indium tin oxide (ITO) for the potential to sustain near infrared surface polariton resonance. ITO is an electron doped metallic oxide, the electromagnetic properties of which depend highly on the fabrication process, that has been shown to exhibit surface polariton resonance in the near infrared. Analyses similar to those performed under the first objective are performed on ITO. Results indicate that ITO indeed exhibits near infrared surface polariton resonance, making it a viable candidate for use in a nano-TPV device.

For Eliza Rose: our angel.

C is for cookie. That's good enough for me.

- Cookie Monster

CONTENTS

ABSTRACT iii

ACKNOWLEDGEMENTS ix

1. INTRODUCTION 1

1.1 Fundamentals of Near-Field Radiative Heat Transfer and Its Application to Nanoscale Gap Thermophotovoltaic (Nano-TPV) Technology 1
1.2 Application of Electromagnetic Metamaterials in the Manipulation of Thermal Radiative Emission 5
1.3 Objective and Organization of the Dissertation 6
1.4 References 9

2. NEAR-FIELD THERMAL EMISSION FROM METAMATERIALS 12

2.1 Abstract 13
2.2 Introduction 13
2.3 Geometry and Formulation 15
2.4 Results 17
2.5 Conclusions 23
2.6 Appendix 23
2.7 References 25

3. TUNING NEAR-FIELD THERMAL RADIATIVE PROPERTIES BY QUANTIFYING SENSITIVITY OF MIE RESONANCE-BASED METAMATERIAL DESIGN PARAMETERS 28

3.1 Abstract 29
3.2 Introduction 29
3.3 Physical and Mathematical Description of the Problem 31
3.4 Results 32
3.5 Fabrication of Mie Resonance-Based Metamaterials 36
3.6 Conclusions 37
3.7 Acknowledgements 37
3.8 References 37

4. FABRICATION AND CHARACTERIZATION OF THREE-DIMENSIONAL MACROSCALE DIELECTRIC MIE RESONANCE-BASED METAMATERIALS 39

4.1 Experimental Characterization and Theoretical Calculations 41

4.2 Fabrication 42
4.3 Characterization 44
4.4 Particle Dispersion 50
4.5 Conclusion 52
4.6 References 52

5. NEAR-FIELD RADIATIVE EMISSION DUE TO SURFACE POLARITON RESONANCE FROM AN INDIUM TIN OXIDE BULK IN THE NEAR INFRARED 54

5.1 Introduction 54
5.2 Problem Description 58
5.3 Results 61
5.4 Conclusions 70
5.5 References 71

6. CONCLUSIONS 74

6.1 Exploration of DMRB Metamaterials as Candidate Emission Sources in Nano-TPV Power Generation 74
6.2 Fabrication of 3D Macroscale DMRB Metamaterials 77
6.3 Exploration of ITO as Candidate Emission Source in Nano-TPV Power Generation 79
6.4 References 80

ACKNOWLEDGEMENTS

Firstly, many thanks go to Mathieu Francoeur. He has offered and continues to offer me wise counsel in the field of academic research. It has been my great pleasure and honor to work with him as we resolved many problems together. And I appreciate his pleasant attitude regardless of the difficulties we faced.

Thanks to Bart Raeymaekers for his similarly wise counsel with regard to the experimental portion of my research. Thanks to Soumyadipta Basu for his assistance in developing theoretical calculations. Thanks to David Schurig for the many enjoyable discussions we had about the physics of electromagnetic metamaterials. And thanks to Tim Ameel for always being a faithful academic advisor. I consider every member of my committee a friend.

I will always treasure the time I spent working alongside my lab-mates. I enjoyed learning new things with them and being taught by them. We came from different parts of the world and different walks of life. But I have felt and always will feel connected to them.

At this point, it is important to note that this academic pursuit came at a very difficult time of my life – a time similar to which a good friend of mine did not survive – making the solemnity of these acknowledgements that much more poignant.

Thanks to the Mt. Ogden Ward of the Ogden Utah East Stake of the Church of Jesus Christ of Latter-day Saints. I was almost constantly upheld by their thoughtfulness and prayers as I sometimes crawled through this journey.

Thanks to all those who have ever participated in the Petersen House of Pain (PHoP). The communal suffering we endured, often chorused with laughter, strengthened me more than you know.

Thanks to my coworkers at Orbital ATK. I will always treasure the friendship I share with them and the lessons they have taught me.

Thanks to my children: Jonathan, Emeline, Sam, and Eliza. I am grateful for their patience and goodness, in spite of their nearly absent father. And I am grateful for the priceless memories offered up whenever I had a moment to spare with my kids.

Words cannot sufficiently express my gratitude to my beautiful wife, Julie. She is patient, forgiving, and caring, each of which was severely tested during these last few years. Unquestionably, I could not have accomplished this work without her perfect presence.

I am grateful to my Heavenly Father for His tender mercies, especially that of little lights in dark tunnels.

Last but not least, I acknowledge the support of the National Science Foundation under grant no. DMR 11-21252.

CHAPTER 1

INTRODUCTION

1.1 Fundamentals of Near-Field Radiative Heat Transfer and Its Application to Nanoscale Gap Thermophotovoltaic (Nano-TPV) Power Generation

When a body is heated, it produces electromagnetic waves, some of which propagate from the heated surface. This form of energy transfer is the traditional view of radiative heat transfer, and is limited by the Planck blackbody distribution [1,2]. Other evanescent, electromagnetic waves that can contribute to energy exchange do not propagate away from the heated surface; instead, they propagate only along the surface, i.e., they fully decay within approximately one dominant emitting wavelength from the surface. Therefore, evanescent exchange may only occur when the heated body is within one wavelength from another body, as defined by Wien's law $\lambda_{max} \cdot T = 2898\ \mu m \cdot K$, where λ_{max} is the dominant emitting wavelength and T is the temperature [1]. Evanescent waves may be sustained along the outer surface of a heated body when propagating waves, generated within said body, attempt to exit at an incident angle greater than the critical angle defined by Snell's law: $\theta_{cr} = \arcsin(n_2/n_1)$ with n_1 and n_2 as the refractive indices of the heated body and the surrounding medium, respectively [3]. Evanescence may also be sustained by the mechanical oscillations of electric dipoles such as free electrons in surface plasmon-polaritons (SPPs) and transverse optical phonons in surface phonon-polaritons (SPhPs) [4]. With surface polaritons (SPs), evanescent waves reside

on both sides of the heated surface. Energy exchange due to evanescent wave modes may result in exceeding the blackbody limit.

The three types of electromagnetic wave modes that occur at the outer surface of a heated body are shown in Figure 1.1: transmission (propagating waves on both sides of the interface), total internal reflection (propagating waves within and evanescent waves outside of the body), and SPs (evanescent waves on both sides of the interface). Since evanescent waves exert an influence within approximately one dominant wavelength from the surface of the heated body and thermal radiation principally occurs in the near infrared, the tunneling of thermally generated evanescent waves may only occur when separated from an absorbing body by distances on the order of 100 nm or less.

Thermal radiation is in the near field when the contribution of evanescent modes is significant, i.e., exchanging bodies are within approximately one dominant emitting wavelength. Traditional thermal radiation analysis techniques – based on Planck's framework [1,2] – are not applicable in this regime. Instead, fluctuational electrodynamics is employed to model near-field thermal radiation [1,2,5–8]. An example of the contribution of near-field thermal exchange on heat flux between two bulks is

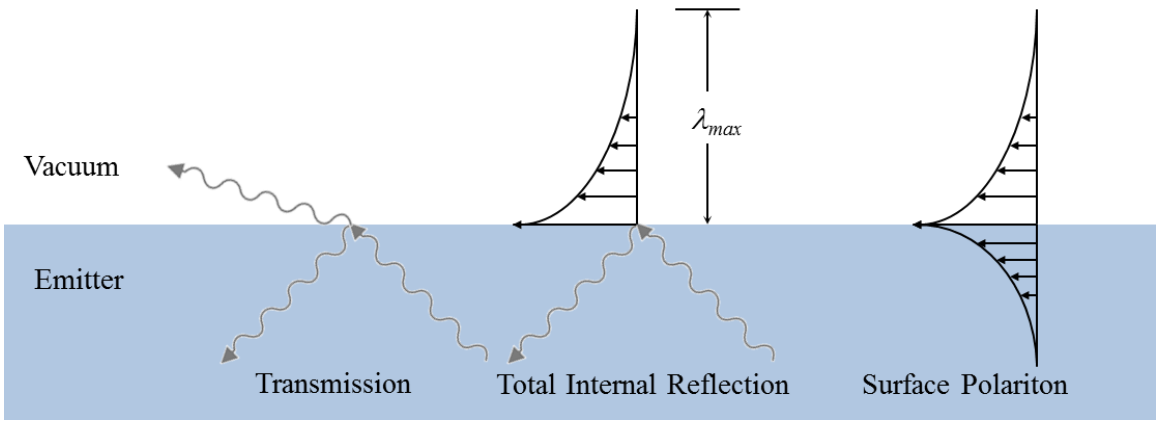

Figure 1.1. Wave modes at an emitter-vacuum interface.

demonstrated in Figure 1.2, where the heat flux between two bulks of intrinsic silicon (Si) at differing temperatures is charted as a function of the vacuum separation gap distance *d*. As *d* decreases to 10 nm, the predicted net radiative flux increases to over 11 times that of the blackbody limit and 20 times that due to propagating modes.

Intrinsic Si cannot sustain SPs; therefore, the aforementioned energy exchange enhancement is due solely to total internal reflection. When SPs are sustained, the energy exchange between two bodies is even greater. Figure 1.3 compares the spectral radiative transfer between two bulks of Si, between two bulks of silicon carbide (SiC), and between two blackbodies. In all cases, the bulks are separated by vacuum at a distance of 150 nm and the temperatures of the two bulks are 300 and 500 K. The Si spectrum is relatively broadband whereas that of the SiC is nearly monochromatic, an artifact of SPhP-mediated energy exchange. The SPhP-mediated radiative transfer between two SiC bulks is an order of magnitude greater than between two blackbodies and more than 30%

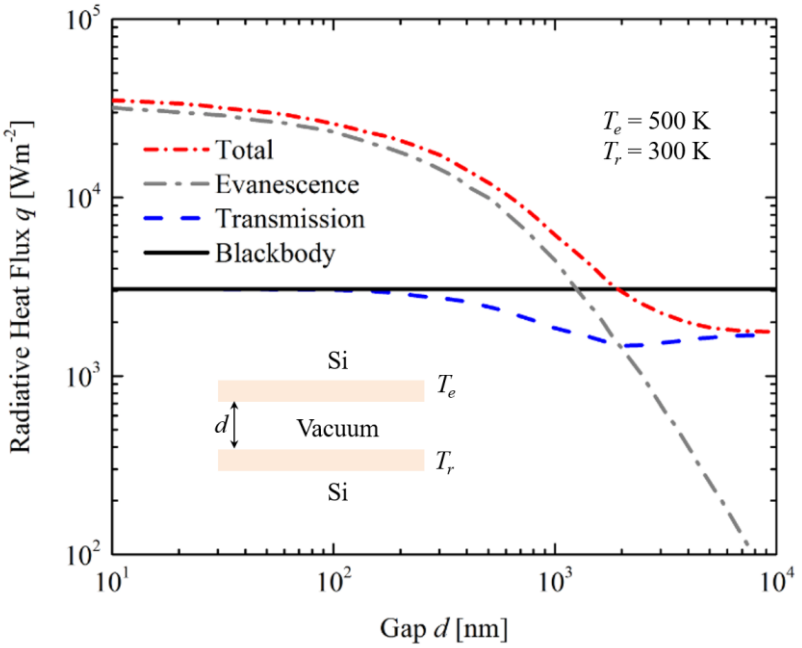

Figure 1.2. Radiative heat flux *q* between two Si bulks vs. separation distance *d*.

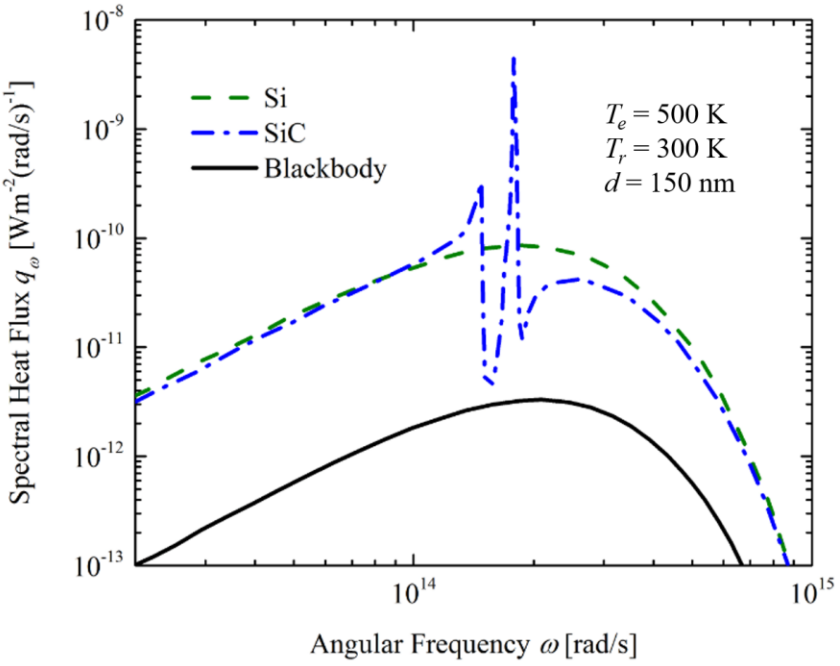

Figure 1.3. Spectral radiative heat flux q between two Si bulks, between two SiC bulks, and between two blackbodies.

greater than between two intrinsic Si bulks.

Whale and Cravalho [9,10] were the first to propose that near-field thermal radiative effects be utilized in a thermophotovoltaic power generation cell by placing the emission source within a dominant emitting wavelength of the absorber, thus originating the nano-TPV system. Thermophotovoltaic cells absorb incoming radiation – optimally at the bandgap wavelength, which is typically in the near infrared (NIR) – and convert it to useful electricity [9,10].

Since they approach optimal performance when absorbing radiation at the cell bandgap, nano-TPV systems may undergo significant performance increases with a NIR radiation source [11,12]. Such a material requires specific electromagnetic – or thermal radiative – properties that are not found in naturally occurring materials. Researchers have recently explored the manipulation of thermal radiative properties, primarily various

combinations of layered films [13–18]. This method relies heavily on the limited inherent electromagnetic properties of the materials involved, consequently limiting the control they offer over thermal radiative properties.

1.2 Application of Electromagnetic Metamaterials in the Manipulation of Thermal Radiative Emission

Metamaterials are composite man-made media that demonstrate exotic electromagnetic – and, hence, thermal radiative – properties that are not found in naturally occurring materials. For example, some metamaterials exhibit negative refractive index while others, consisting solely of nonmagnetic media (relative magnetic permeability is unity), exhibit effective permeabilities greater or less than one. Metamaterials consist of subwavelength, repeated unit structures termed "meta-atoms," the geometry and constituents of which drive the macroscale effective electromagnetic properties of the medium. With current micro and nanoscale fabrication techniques, the configuration of meta-atoms is readily controlled, paving the way for engineering thermal radiative properties of materials. Efforts to tune thermal emission using metamaterials have involved the study of a number of different configurations including photonic crystals [19], gratings [20], rod-like structures [21], and split-ring resonators [22,23].

The meta-atoms in dielectric Mie resonance-based (DMRB) metamaterials are dielectric inclusions, e.g., spheres, cylinders, or cubes, embedded in a dielectric host medium [24]. A few of the advantages of employing this type of metamaterial in thermal applications are: fabrication that is potentially inexpensive and easily scaled to the dimensions of a practically sized thermal system; isotropic electromagnetic response; and low losses. Since most of the parameters that define Mie meta-atoms can be manipulated via current fabrication techniques, engineering thermal radiative properties is possible

with DMRB metamaterials. Wheeler et al. [25] were the first to fabricate a three-dimensional macroscale DMRB metamaterial, which consisted of SiC particles within a potassium bromide host medium. They observed electric and magnetic dipole resonances in their metamaterial specimens using spectroscopy that agreed well with theoretical predictions.

1.3 Objective and Organization of the Dissertation

As mentioned in Section 1.1, to optimize the performance of nano-TPV devices, it is crucial that a nearly monochromatic NIR emission source be established. Therefore, the overarching goal of this PhD research project is to theoretically and experimentally explore material(s) for potential to sustain near infrared SP resonance. Pursuant to this goal, the results of the dissertation are divided into three objectives, which are described below.

The first objective of this dissertation is to theoretically explore the capability of DMRB metamaterials to sustain near infrared SP resonance. In the near field, SP mediated thermal radiative exchange is quasimonochromatic and exceeds the far-field blackbody distribution by orders of magnitude [1,26]. The SP resonance frequency depends entirely on the electric permittivity and magnetic permeability of a material. Francoeur et al. [27] performed the first theoretical near-field thermal analysis of DMRB metamaterials. They calculated radiative heat flux between metamaterials consisting of SiC spheres within a host medium of potassium bromide and were the first to show the tunability of near-field thermal radiative properties by adjusting the design parameters of meta-atoms.

The calculations performed by Francoeur et al. relied heavily on an effective

medium theory, the Clausius-Mossotti mixing relation [28], which is used to approximate the microscopically discrete composite mixture as a macroscopically homogeneous, isotropic medium. Commensurate with this theory is the assumption that the dimensions of the meta-atom are much smaller than the wavelength of interest. As this assumption becomes less valid, i.e., meta-atom dimensions approach the dominant emitting wavelength, conclusions drawn from the effective medium results are weakened. Since the geometric extent of the near field (hundreds of nanometers) is on the order of the size of the meta-atom, a similar lack of confidence is inherent to the conclusions related to the radiative heat flux calculations. Additionally, researchers have questioned the validity of effective medium theory in near-field calculations [29–32].

The typical approach for analyzing near-field thermal phenomena is to calculate the radiative heat flux between two bulks of the material of interest [23,27,33–35]. Heat flux can differ greatly with changes to the material receiving the radiative flux. The local density of electromagnetic states (LDOS) quantifies the energy that is potentially harvestable from an emitting surface, independent of the receiving material. Therefore, Chapter 2 outlines the analysis of the same metamaterial as described by Francoeur et al., in addition to another that has been analyzed thermally by Joulain et al. [33], by calculating the LDOS instead of the heat flux. As a result, the LDOS equation is derived for arbitrarily magnetic media. Additionally, a SP dispersion relation analysis technique is developed that accounts for losses in the emitting medium, as all other similar analyses to that point have been performed assuming no losses. This chapter was published in *Photonics and Nanostructures: Fundamentals and Applications* in 2013 [36].

Although Francoeur et al. and Chapter 2 both show that the effective properties of

metamaterials can be engineered, the metamaterials explored therein are not optimal for nano-TPV devices. Namely, they do not provide monochromatic emission in the NIR. In Chapter 3, another DMRB metamaterial is explored with the intent to remedy this deficiency. An analysis is conducted on a Si DMRB metamaterial to determine the sensitivity of a few meta-atom design parameters on SP resonance frequencies. These metamaterials show near-field thermal radiative properties that better qualify them for potential nano-TPV device application than those studied in Chapter 2. Also in Chapter 3, a technique is proposed for the fabrication of DMRB metamaterials. The contents of Chapter 3 were published in the *Journal of Quantitative Spectroscopy and Radiative Transfer* in 2013 [37].

In spite of, but not to detract from, the importance of theoretically exploring the potential application of DMRB metamaterials in nano-TPV systems, it is crucial that these materials also be analyzed experimentally. Therefore, the second objective of this dissertation is to demonstrate the fabrication and characterization of this type of metamaterial. Chapter 4 is a summary of experimental results for some DMRB metamaterials. Metamaterial specimens were fabricated by mixing dielectric nanoparticles into two part, room temperature curing epoxy resins. The fabrication process for these metamaterials evolved as transmission measurements were compared with theoretical calculations, each fabrication attempt revealing an additional level of scrutiny essential for the successful fabrication of a DMRB metamaterial with NIR SP resonance.

With the evident difficulty of fabricating the type of metamaterials analyzed theoretically in Chapters 2 and 3, Chapter 5 documents the pursuit of a third objective:

exploring the capability of another material for the potential of sustaining NIR SP resonance. Indium tin oxide (ITO) is a naturally occurring material, the electromagnetic properties of which are heavily dependent on the fabrication method [38]. An analysis similar to that described in Chapter 3 is detailed in Chapter 5 and ITO is shown to be an adequate candidate for use in nano-TPV devices, with careful attention to the fabrication process. The contents of Chapter 5 will be submitted for publication in a technical journal.

Finally, Chapter 6 summarizes the findings of this dissertation.

1.4 References

[1] J.R. Howell, M.P. Mengüç, and R. Siegel, *Thermal Radiation Heat Transfer*, 6th ed. (CRC Press, Boca Raton, 2015).

[2] M.F. Modest, *Radiative Heat Transfer*, 3rd ed. (Academic Press, San Diego, 2013).

[3] E. Hecht, *Optics*, 5th ed. (Pearson Education, New York, 2015).

[4] J.-P. Mulet, K. Joulain, R. Carminati, and J.-J. Greffet, Nanosc. Microsc. Therm. **6**, 1703 (2006).

[5] D. Polder and V. Van Hove, Phys. Rev. B **4**, 3303 (1971).

[6] S.M. Rytov, Y.A. Kravtsov, and V.I. Tatarskii, *Principles of Statistical Radiophysics 3: Elements of Random Fields*, (Springer, New York, 1989).

[7] L. Novotny and B. Hecht, *Principles of Nano-Optics*, (Cambridge University Press, New York, 2006).

[8] Z.M. Zhang, *Micro/Nanoscale Heat Transfer*, (McGraw-Hill, New York, 2007).

[9] M.D. Whale, *A Fluctuational Electrodynamics Analysis of Microscale Radiative Heat Transfer and the Design of Microscale Thermophotovoltaic Devices*, PhD Thesis, (Massachusetts Institute of Technology, Cambridge, 1997).

[10] M.D. Whale and E.G. Cravalho, IEEE T. Energy Conver. **17**, 130 (2002).

[11] M. Laroche, R. Carminati, and J.-J. Greffet, J. Appl. Phys. **100**, 063704 (2006).

[12] M. Francoeur, R. Vaillon, and M.P. Mengüç, IEEE T. Energy Conver. **26** 686

(2011).

[13] B.J. Lee, L.P. Wang, and Z. M. Zhang, Opt. Express **16** 11328 (2008).

[14] S.-A. Biehs, D. Reddig, and M. Holthaus, Eur. Phys. J. *B* **55** 237 (2007).

[15] K. Joulain and C. Henkel, Appl. Phys. B **93** 151 (2008).

[16] P. Ben-Abdallah, K. Joulain, J. Drevillon, and G. Domingues, Appl. Phys. Lett. **94** 15117 (2009).

[17] M. Francoeur, M.P. Mengüç, and R. Vaillon, Appl. Phys. Lett. **93** 143109 (2008).

[18] C.J. Fu and W.C. Tan, J. Quant. Spectrosc. Ra. **110** 1027 (2009).

[19] P.W. Mauriz, M.S. Vasconcelos, F.F. de Medeiros, and E.L. Albuquerque, Microelectr. J. **40** 848 (2009).

[20] Z. Wei, Y. Cao, J. Han, C. Wu, Y. Fan, and H. Li, Appl. Phys. Lett. **97** 141901 (2010).

[21] X. Liu, T. Tyler, T. Starr, A.F. Starr, N.M. Jokerst, and W.J. Padilla, Phys. Rev. Lett. **107** 045901 (2011).

[22] V.M. Shalaev, W. Cai, U.K. Chettiar, H.-K. Yuan, A.K. Sarychev, V.P. Drachev, and A.V. Kildishev, Opt. Lett. **24** 3356 (2005).

[23] Z. Zheng and Y. Xuan, Chinese Sci. Bull. **56** 2312 (2011).

[24] Q. Zhao, L. Kang, B. Du, H.-J. Zhao, Q. Xie, B. Li, J. Zhou, L.-T. Li, and Y.-G. Meng, Chinese Sci. Bull. **53** 3272 (2008).

[25] M.S. Wheeler, J.S. Aitchison, J.I.L. Chen, G.A. Ozin, and M. Mojahedi, Phys. Rev. B **79** 073103 (2009).

[26] S. Basu, Z.M. Zhang, and C.J. Fu, Int. J. Energ. Res. **33** 1203 (2009).

[27] M. Francoeur, S. Basu, and S.J. Petersen, Opt. Express **19** 18774 (2011).

[28] M.S. Wheeler, *A Scattering-Based Approach to the Design, Analysis, and Experimental Verification of Magnetic Metamaterials Made from Dielectrics*, PhD Thesis (University of Toronto, Toronto, 2010).

[29] B. Liu and S. Shen, Phys. Rev. B **87** 115403 (2013).

[30] M. Tschikin, S.A. Biehs, R. Messina, P. Ben-Abdallah, J. Opt. **15** 105101 (2013).

[31] X.L. Liu, T.J. Bright, and Z.M. Zhang, J. Heat Transf. **136** 092703 (2014).

[32] A. Didari and M.P. Mengüç, Opt. Express **23** A547 (2015).

[33] K. Joulain, J. Drevillon, and P. Ben-Abdallah, Phys. Rev. B **81** 165119 (2010).

[34] Z. Zheng and Y. Xuan, Int. J. Heat Mass Tran. **54** 1101 (2011).

[35] S. Basu and M. Francoeur, Appl. Phys. Lett. **99** 143107 (2011).

[36] S.J. Petersen, S. Basu, and M. Francoeur, Photonic. Nanostruct. **11** 167 (2013).

[37] S.J. Petersen, S. Basu, B. Raeymaekers, and M. Francoeur, J. Quant. Spectrosc. Ra. **129** 277 (2013).

[38] P.R. West, S. Ishii, G.V. Naik, N.K. Emani, V.M. Shalaev, and A. Boltasseva, Laser Photon. Rev. **4** 795 (2010).

CHAPTER 2

NEAR-FIELD THERMAL EMISSION FROM METAMATERIALS

Photonics and Nanostructures – Fundamentals and Applications (2013) **11**, 167–181.

Available online at www.sciencedirect.com

SciVerse ScienceDirect

PHOTONICS AND NANOSTRUCTURES Fundamentals and Applications

Photonics and Nanostructures – Fundamentals and Applications 11 (2013) 167–181

www.elsevier.com/locate/photonics

Near-field thermal emission from metamaterials☆

Spencer J. Petersen [a,*], Soumyadipta Basu [b], Mathieu Francoeur [a,**]

[a] Radiative Energy Transfer Lab, Department of Mechanical Engineering, University of Utah, Salt Lake City, UT 84112, USA
[b] Assembly Technology Development, Intel Corporation, Chandler, AZ 85226, USA

Received 17 January 2013; received in revised form 9 March 2013; accepted 12 March 2013
Available online 17 April 2013

Abstract

A closed form expression for the local density of electromagnetic states (LDOS) due to a thermally emitting metamaterial bulk is derived from Maxwell's equations combined with fluctuational electrodynamics. The final form is the same as that for nonmagnetic materials, where the influence of the magnetic permeability is embedded in the Fresnel reflection coefficients. Spectral distributions of LDOS near metallic- and dielectric-based metamaterials are investigated. Results reveal that LDOS profiles are dominated by surface polaritons (SPs) in both TE and TM polarization states. A detailed discussion is provided on the necessary conditions for exciting TM- and TE-polarized SPs via a dispersion relation analysis that accounts for losses. Beyond the conventional conditions for excitation of SPs, the lossy dispersion relation analysis demonstrates mathematically that SPs exist when the imaginary parts of the permittivity or permeability, as well as $n'n''$, are close to zero, where n' and n'' are the real and imaginary parts of the refractive index, respectively. An asymptotic expression for the extreme near field LDOS is derived, showing a Δ^{-3} power law relationship, as for nonmagnetic media, between LDOS and distance from the emitting bulk Δ. Results obtained from this study will assist in assessing material properties of arbitrarily electromagnetic materials in applications related to energy harvesting.

Keywords: Near-field radiation; Thermal emission; Mie resonance; Local density of electromagnetic states; Dispersion relation

1. Introduction

Near-field radiative heat transfer is distinguished from the classical far-field regime when the exchanging bodies are separated by distances on the order of, or smaller than, the dominant emitting wavelength [1,2]. In the near-field regime, tunneling of evanescent modes can result in energy exchange exceeding Planck's blackbody distribution by orders of magnitude. These evanescent modes include evanescent waves generated by total internal reflection (TIR) and surface polaritons (SPs). Enhanced energy transfer at subwavelength distances may benefit numerous technological fields such as thermal rectification [3–5], thermal switches [6], imaging [7], and thermophotovoltaic (TPV) power generation [8–12], among others.

Tuning the electromagnetic response of materials is now a possibility due to the emerging field of metamaterials. Electromagnetic metamaterials consist of subwavelength unit structures referred to as meta-atoms. Exotic properties such as negative electric permittivity, magnetic permeability, and/or refractive index are achievable by manipulating these meta-atoms [13–17]. It is also possible with metamaterials to design magnetic media from nonmagnetic constituents and to tune near-field thermal radiative properties. However, the majority of the effort in this area has been toward the design of selective thermal emission and absorption in the far field [18–22].

☆ The article belongs to the special section Metamaterials.

* Corresponding author. Tel.: +1 8016904414.
** Corresponding author. Tel.: +1 8015815721.
E-mail addresses: s.j.petersen@m.cc.utah.edu (S.J. Petersen), mfrancoeur@mech.utah.edu (M. Francoeur).

1569-4410/$ – see front matter
http://dx.doi.org/10.1016/j.photonics.2013.03.002

To date, only five papers have been published regarding near-field thermal emission from metamaterials consisting of three-dimensional meta-atoms. Joulain et al. [23] were the first to study the near-field heat flux spectra between two identical metamaterials made up of an array of split-ring resonators (SRRs) and wires. Zheng and Xuan [24] calculated heat transfer between two bulks of a similar SRR-wire metamaterial, establishing a general procedure for analyzing near-field energy transfer in one-dimensional layered media of arbitrary permittivity and permeability. They expanded their effort by analyzing energy transfer between yet another SRR-wire metamaterial and other media, i.e., doped silica and aluminum [25]. Basu and Francoeur [26] calculated the penetration depth of SP mediated near-field thermal radiation when exchanged between two bulks of SRR-wire metamaterial. They observed that it was possible to achieve different penetration depths for magnetic and electric resonances depending on the material properties. Francoeur et al. [27] performed heat flux calculations between two identical metamaterials made up of silicon carbide (SiC) spheres in a potassium bromide (KBr) host medium. They concluded that near-field thermal spectra can be controlled by varying the metamaterial adjustable parameters such as the SiC sphere diameter. All four groups identified an additional channel through which significant energy exchange can occur with electromagnetic metamaterials: TE-polarized SPs. This phenomenon occurs only when the materials involved are effectively magnetic. Note that in all these aforementioned studies, the effective medium theory (EMT) was employed for predicting the effective electric permittivity and magnetic permeability of metamaterials.

Smith and Schurig [28] introduced the idea of indefinite media with hyperbolic dispersion, or hyperbolic metamaterials, and identified one-dimensional layered media (i.e., one-dimensional meta-atoms) as an avenue for generating such a metamaterial. Recently, the application of hyperbolic metamaterials to near-field thermal emission has attracted considerable interest [29–35]. Biehs et al. [30] showed that hyperbolic metamaterials can be considered the near-field analog of a blackbody, since the near-field enhancement from such structures is broadband. Tschikin et al. [35] questioned the validity of the EMT for hyperbolic metamaterials made of thin films and observed that the EMT did not provide accurate results in the near field when SPs are present. Similar results were shown by Guo et al. [32] in their study on hyperbolic metamaterials. This conclusion was drawn by comparing EMT results against direct near-field thermal emission predictions based on an S-matrix approach [36–45].

This paper focuses on near-field thermal emission by metamaterials comprised of three-dimensional subwavelength inclusions. While hyperbolic metamaterials made of thin films are easier to fabricate than the structures considered here, the broadband enhancement of the near-field thermal spectrum is not suitable for applications such as nanoscale-gap TPV (nano-TPV) power generators [12]. Three-dimensional meta-atomic structures, such as those discussed in Refs. [23–27], are preferable in order to achieve quasi-monochromatic near-field thermal emission, which is needed for viable and highly efficient nano-TPV power generation [10,12]. Direct calculation of near-field thermal emission by metamaterials consisting of three-dimensional meta-atoms, i.e., particulate media, is currently intractable. As such, near-field thermal emission is predicted in this paper using the local density of electromagnetic states (LDOS) with electric permittivity and magnetic permeability calculated from the EMT. The results thus obtained will provide general trends and significant insights into the near-field thermal spectra emitted by metamaterials. Additionally, these predictions will be crucial in assessing the validity of the EMT when direct calculation of near-field thermal emission by particulate media will be possible.

The LDOS has been used to quantify the near-field radiative characteristics of thermal systems in various configurations. It has been calculated due to free emission near a bulk [46], near a film [36], between two identical bulks [47], between two identical films [41,48], and near layered media [38,49], all of which involve nonmagnetic materials. In this work, a general thermal emission LDOS expression is derived near a bulk material of arbitrary electric permittivity and magnetic permeability. The purpose of this paper is to outline the derivation of the LDOS equation and to explore the physics of TM- and TE-polarized near-field thermal emission by metamaterials via a dispersion relation analysis that accounts for losses. Such a study will provide general trends for the evaluation of candidate materials for use in near-field energy exchange applications, such as nano-TPV power generators.

In Section 2, the equation for LDOS due to thermal emission is rigorously derived from first principles. Section 3 discusses near-field emission for two different metamaterial configurations and includes an exploration of the LDOS results with an accompanying lossy SP dispersion relation analysis. Finally, conclusions are provided in Section 4. Further details regarding the derivation of the LDOS expression are provided in Appendix.

2. Geometry and formulation

2.1. Configuration

Herein is considered the LDOS at a distance Δ from a bulk material emitting into vacuum, as shown schematically in Fig. 1. Throughout this derivation and analysis, only the LDOS contributions from the emitting medium are considered. Those from free space and reflected by the interface are omitted since the primary goal is to quantify energy harvestable from the bulk. Consequently, from this point forward, LDOS due to thermal emission of a bulk will be referred to as "LDOS" for convenience. The interface between the emitter (medium 0) and the vacuum (medium 1) is smooth and the bulk is modeled as semi-infinite. The interface is infinite in the ρ-direction and symmetric in the θ-direction of a cylindrical coordinate system. Hence, variations are only manifest along the z-direction. The emitting layer is assumed to be in local thermodynamic equilibrium (LTE) at temperature T_0, homogeneous, isotropic, and described by frequency-dependent relative electric permittivity $\varepsilon_0 (= \varepsilon_0' + i\varepsilon_0'')$ and relative magnetic permeability $\mu_0 (= \mu_0' + i\mu_0'')$ local in space. From this point forward, the term "relative" will be omitted from permittivity and permeability for convenience.

2.2. Theory

The LDOS is derived using Maxwell's equations combined with fluctuational electrodynamics, where thermal emission is accounted for via stochastic current densities [50]. More specifically, stochastic currents due to electric dipole oscillations $\mathbf{J}^{r,e}$ and magnetic dipole oscillations $\mathbf{J}^{r,m}$ are added to Ampère's and Faraday's laws, respectively. Assuming a time dependence of $\exp(-i\omega t)$, with ω as the angular frequency and t as time, the thermally generated electric and magnetic fields can be expressed as [27]:

$$\mathbf{E}(\mathbf{r},\omega) = i\omega\mu_0\mu_v \int_V \overline{\overline{\mathbf{G}}}^{Ee}(\mathbf{r},\mathbf{r}',\omega)\cdot\mathbf{J}^{r,e}(\mathbf{r}',\omega)dV' - \int_V \overline{\overline{\mathbf{G}}}^{Em}(\mathbf{r},\mathbf{r}',\omega)\cdot\mathbf{J}^{r,m}(\mathbf{r}',\omega)dV' \tag{1a}$$

$$\mathbf{H}(\mathbf{r},\omega) = \int_V \overline{\overline{\mathbf{G}}}^{He}(\mathbf{r},\mathbf{r}',\omega)\cdot\mathbf{J}^{r,e}(\mathbf{r}',\omega)dV' + i\omega\varepsilon_0\varepsilon_v \int_V \overline{\overline{\mathbf{G}}}^{Hm}(\mathbf{r},\mathbf{r}',\omega)\cdot\mathbf{J}^{r,m}(\mathbf{r}',\omega)dV' \tag{1b}$$

where ε_v and μ_v are the free space permittivity and permeability, respectively. The terms $\overline{\overline{\mathbf{G}}}^{E(H)e(m)}$ are the dyadic Green's functions (DGFs) relating the electric E (magnetic H) field at frequency ω observed at location $\mathbf{r}$ to an electric e (magnetic m) source at $\mathbf{r}'$. The DGFs for layered media of arbitrary permittivity and permeability are available in Refs. [23,24].

The monochromatic near-field energy density at location $\mathbf{r}$ in vacuum is calculated by computing the time-averaged sum of the squared magnitudes of the electric and magnetic fields [51]:

$$\langle u_\omega(\mathbf{r},T_0)\rangle = \varepsilon_v\left\langle|\mathbf{E}(\mathbf{r},\omega)|^2\right\rangle + \mu_v\left\langle|\mathbf{H}(\mathbf{r},\omega)|^2\right\rangle \tag{2}$$

where the symbol $\langle\ \rangle$ represents an ensemble average.

It is important to note that this equation is only applicable when the energy density is computed in nondispersive media [52]. An expression for the energy density for the problem shown in Fig. 1 is derived by substituting Eqs. (1a) and (1b) into Eq. (2), and by using the plane wave representation (i.e., Weyl components) of the DGFs. After application of the fluctuation–dissipation theorem (FDT) [50] and assuming the ergodic hypothesis [53], the following expression is obtained for the energy density at $z = \Delta$ from the emitting bulk:

$$\langle u_\omega(\Delta,T_0)\rangle = \frac{k_v^2\Theta(\omega,T_0)}{2\pi^2\omega}\int_{k_\rho=0}^{\infty} k_\rho dk_\rho \int_{z'=-\infty}^{0} \Big\{\varepsilon_0''\Big[k_v^2|\mu_0|^2 g_{\alpha\beta}^{Ee}(k_\rho,\Delta,z',\omega)g_{\alpha\beta}^{Ee*}(k_\rho,\Delta,z',\omega) + g_{\alpha\beta}^{He}(k_\rho,\Delta,z',\omega)g_{\alpha\beta}^{He*}(k_\rho,\Delta,z',\omega)\Big] + \mu_0''\Big[g_{\alpha\beta}^{Em}(k_\rho,\Delta,z',\omega)g_{\alpha\beta}^{Em*}(k_\rho,\Delta,z',\omega) + k_v^2|\varepsilon_0|^2 g_{\alpha\beta}^{Hm}(k_\rho,\Delta,z',\omega)g_{\alpha\beta}^{Hm*}(k_\rho,\Delta,z',\omega)\Big]\Big\}dz' \tag{3}$$

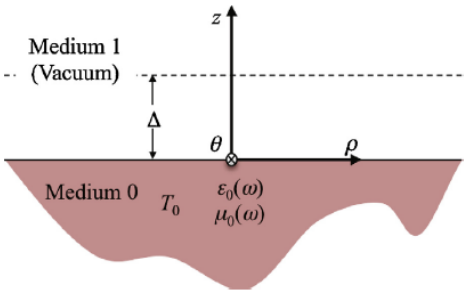

Fig. 1. Geometric configuration of the problem under consideration: the LDOS is calculated in vacuum (medium 1) at a distance Δ from an emitting bulk (medium 0) with permittivity ε_0 and permeability μ_0.

where $\Theta(\omega, T_0)$ is the mean energy of a Planck oscillator in thermal equilibrium, $k_v (= \omega/c_v)$ is the vacuum wavevector with c_v as the speed of light in vacuum, k_ρ is the tangential wavevector and is a pure real number, and $g_{\alpha\beta}^{E(H)e(m)}$ are the Weyl components of the DGFs. The subscripts α and β denote the double summation over the three coordinate axes ρ, θ, and z, while the superscript * denotes the complex conjugate. The explicit expressions for the Weyl components of the DGFs for the two layer system shown in Fig. 1 are provided in Appendix. Note that the specific form of the energy density as given by Eq. (3) assumes that ε_0'' and μ_0'' are greater than zero. For lossless media, the FDT reveals that the ensemble average of the spatial correlation function of stochastic currents is zero, thus implying that there is no thermal emission. For this particular case, Eq. (3) is not applicable and the energy density provided by Eq. (2) is simply equal to zero.

The near-field energy density is equal to the product of the LDOS and the mean energy of a Planck oscillator; the LDOS can thus be calculated from Eq. (3) as follows: $\rho_\omega(\Delta) = \langle u_\omega(\Delta, T_0)\rangle / \Theta(\omega, T_0)$. Substitution of the appropriate Weyl components of the DGFs into Eq. (3), normalized by $\Theta(\omega, T_0)$, and integration over the emitting source volume leads to the following closed form expression for the LDOS at a distance Δ from a material with arbitrary permittivity and permeability:

$$\rho_\omega(\Delta) = \frac{1}{4\pi^2\omega}\left\{k_v^2\int_0^{k_v}\frac{k_\rho dk_\rho}{|k_{z1}|}[(1-|r_{10}^{TM}|^2) + (1-|r_{10}^{TE}|^2)] + 2\int_{k_v}^{\infty}\frac{k_\rho^3 dk_\rho}{|k_{z1}|}[\mathrm{Im}(r_{10}^{TM}) + \mathrm{Im}(r_{10}^{TE})]e^{-2|k_{z1}|\Delta}\right\} \tag{4}$$

where r_{10}^{TM} and r_{10}^{TE} are the Fresnel reflection coefficients at the interface 1-0 given respectively by [54]:

$$r_{10}^{TM} = \frac{\varepsilon_0 k_{z1} - \varepsilon_1 k_{z0}}{\varepsilon_0 k_{z1} + \varepsilon_1 k_{z0}} \tag{5a}$$

$$r_{10}^{TE} = \frac{\mu_0 k_{z1} - \mu_1 k_{z0}}{\mu_0 k_{z1} + \mu_1 k_{z0}} \tag{5b}$$

In the above expressions, k_{zj} is the perpendicular component of the wavevector calculated as $k_{zj} = \pm\sqrt{\varepsilon_j\mu_j k_v^2 - k_\rho^2}$. Note that k_{zj} is calculated using the negative root only when the real part of the refractive index of medium j is negative [27,55].

In spite of normalizing the energy density by $\Theta(\omega, T_0)$ to obtain Eq. (4), temperature is still crucial to the LDOS formulation. The final equation is indeed independent of temperature. However, the FDT requires the emitting medium to be in LTE, thus necessitating a temperature to be specified. Additionally, for materials like doped silicon, the optical properties of which are a function of temperature, the LDOS does depend on the temperature of the emitting medium.

The term within the integration over k_ρ from 0 to k_v in Eq. (4) represents the contribution from propagating waves, while the term integrated from k_v to ∞ accounts for waves that are evanescent in the vacuum. For the latter modes, the exponential $\exp(-2|k_{z1}|\Delta)$ shows that this contribution to the LDOS decays exponentially normal to the surface of the thermal emitter. The physical interpretation of Eq. (4) is thus straightforward. For the propagating component of the LDOS, $(1-|r_{10}^{TM}|^2) + (1-|r_{10}^{TE}|^2)$ represents the sum of the spectral emittance/absorptance for a single bulk half-space for the two polarization states. Similarly, the term $\mathrm{Im}(r_{10}^{TM}) + \mathrm{Im}(r_{10}^{TE})$ can be interpreted as the emittance/absorptance of evanescent waves.

Note that the final form of the LDOS equation is identical to what has been obtained for nonmagnetic materials [46]. The differences lie in the Fresnel reflection coefficients, where permeability terms are found, both explicitly and in the perpendicular component of the wavevector. Details regarding the derivation of Eq. (4) are provided in Appendix.

In the extreme near field where $\Delta \to 0$, the LDOS is dominated by modes with $k_\rho \gg k_v$, such that the z-component of the wavevector in medium j can be approximated by $k_{zj} \sim ik_\rho$ Consequently, the Fresnel reflection coefficients become independent of k_ρ:

$$r_{10}^{TM} \sim \frac{\varepsilon_0 - 1}{\varepsilon_0 + 1} = \frac{2\varepsilon_0''}{|\varepsilon_0 + 1|^2} \tag{6a}$$

$$r_{10}^{TE} \sim \frac{\mu_0 - 1}{\mu_0 + 1} = \frac{2\mu_0''}{|\mu_0 + 1|^2} \tag{6b}$$

Using these approximations, the LDOS reduces to:

$$\rho_\omega(\Delta) \sim \frac{1}{\pi^2\omega}\left[\frac{\varepsilon_0''}{|\varepsilon_0+1|^2} + \frac{\mu_0''}{|\mu_0+1|^2}\right]\int_{k_v}^{\infty} k_\rho^2 e^{-2k_\rho\Delta} dk_\rho \tag{7}$$

where the contribution from propagating waves has been neglected. Using the dimensionless variable $\eta = k_\rho\Delta$, the LDOS in the extreme near field can be expressed as:

$$\rho_\omega(\Delta) \sim \frac{S(\eta_K)}{\pi^2\omega\Delta^3}\left[\frac{\varepsilon_0''}{|\varepsilon_0+1|^2} + \frac{\mu_0''}{|\mu_0+1|^2}\right] \tag{8a}$$

where

$$S(\eta_K) = \int_{\eta_K}^{\infty} \eta^2 e^{-2\eta} d\eta \tag{8b}$$

and $\eta_K = K\Delta$ such that $K \gg k_v$. For any $\eta_K \geq 0$, $S \in [0, 0.25]$, e.g., for $K = 10k_\rho$, $S = 0.22$.

The asymptotic analysis thus shows that the LDOS follows a Δ^{-3} power law as for nonmagnetic materials [46,56]. It is also clear from Eq. (8a) that resonance of the near-field thermal spectrum may arise in both polarization states, as discussed in greater detail in Section 3.

3. Results

Two metamaterial configurations are considered. The objective herein is to explore the physics of TE- and TM-polarized SP mediated near-field thermal emission via LDOS profiles and dispersion relations. Such a study is crucial in order to establish a tool for the analysis of metamaterials selectively emitting in the near field.

The EMT provides the backbone to the study of metamaterials by modeling macroscopic permittivity and permeability for a composite medium consisting of subwavelength inclusions. Various methods and models have been established [17,57,58] for approximating these effective properties, two of which are employed in this work. It is important to note that the effective medium approach provides locally averaged macroscopic properties that are independent of the distance from the metamaterial. In reality, since metamaterials are made up of unit structures, some spatial dependence of the effective properties is inevitable at distances from the metamaterial on the order of, or smaller than, the characteristic dimension of the meta-atoms. As discussed in the Introduction, since direct calculation of near-field thermal emission by particulate media is currently intractable, the EMT is employed in this work. The results thus obtained will assist in exploring the physics of SP mediated near-field thermal emission by metamaterials, and will eventually be useful for assessing the validity of the EMT in the near field of a thermal source.

The first metamaterial considered is made up of an array of metallic wires and SRRs [23–25]. The following models are used to calculate the effective permittivity and permeability of the metamaterial, respectively:

$$\varepsilon_0 = 1 - \frac{\omega_p^2}{\omega(\omega + i\gamma_e)} \tag{9a}$$

$$\mu_0 = 1 - \frac{F\omega^2}{\omega^2 - \omega_0^2 + i\gamma_m\omega} \tag{9b}$$

where ω_p is the equivalent plasma frequency, γ_e is the electric dissipation factor, F is the volume filling fraction, ω_0 is the magnetic resonance frequency, and γ_m is the magnetic dissipation factor [56,57]. For this analysis, these values are as follows: $\omega_p = 10^{14}$ rad/s, $\gamma_e = \gamma_m = 0.01\omega_p$, $F = 0.5$, and $\omega_0 = 0.4\omega_p$. Note that, in reality, this metamaterial does not lead to an isotropic electromagnetic response. Despite this limitation, the effective properties given by Eqs. (9a) and (9b) provide a reasonable model for exploring the physics of SP mediated near-field thermal emission.

A dielectric Mie resonance-based metamaterial is also considered, where the meta-atoms are SiC spherical particles in a host medium of KBr (periodic arrangement in a simple cubic lattice). Here, a sphere radius r_s of 1 μm is chosen since it is the smallest particle size that results in a TE-polarized SP [27]. The effective permittivity and permeability of the dielectric-based metamaterial are determined, respectively, by the scattering-corrected Clausius–Mossotti relations [59]:

$$\frac{\varepsilon_0}{\varepsilon_h} = 1 + N\left[\frac{k_0^3}{i6\pi}\left(\frac{1}{a_1} - 1\right) - \frac{N}{3}\right]^{-1} \tag{10a}$$

$$\frac{\mu_0}{\mu_h} = 1 + N\left[\frac{k_0^3}{i6\pi}\left(\frac{1}{b_1} - 1\right) - \frac{N}{3}\right]^{-1} \tag{10b}$$

where ε_h and μ_h are the permittivity and permeability of the host medium, respectively, $N = 1/a^3$ is the number of particles per unit volume, a is the lattice constant, k_0 is the wavevector in the host medium, and a_1 and b_1 are the first order Mie coefficients [60]. The KBr host medium permittivity ε_h is assigned a constant value of 1.22 [61]; KBr is nonmagnetic ($\mu_h = 1$). The volume filling fraction $F = 4\pi/3(r_s/a)^3$ is fixed at 0.4. Unlike the metallic-based, this Mie resonance-based metamaterial is isotropic and similar metamaterials have been shown experimentally to mimic predicted electromagnetic effective medium properties [59,61,62].

It is important to note the manner in which the sign of the refractive index is determined. Employing the complex plane representation of the permittivity $\varepsilon = |\varepsilon|\exp(i\phi_\varepsilon)$ and permeability $\mu = |\mu|\exp(i\phi_\mu)$ – where $\phi_\varepsilon = \arctan(\varepsilon''/\varepsilon')$ and $\phi_\mu = \arctan(\mu''/\mu')$ are the permittivity and permeability phase angles, respectively, and are between 0 and π (to satisfy causality) [17] – the real part of the refractive index can be calculated as $n' = \sqrt{|\varepsilon||\mu|}\cos(\phi_n)$, where $\phi_n = (\phi_\varepsilon + \phi_\mu)/2$ is the refractive index phase angle. Therefore, the refractive index is positive for $\phi_n < \pi/2$ and negative otherwise.

The phase velocity of a wave is reversed when it experiences negative refraction, thus forcing the electric

and magnetic fields to form a left-handed triplet with the phase velocity [17]. However, the wave group velocity is not reversed, keeping the energy flow in the same direction as before experiencing the refraction. Therefore, when evaluating energy-related quantities in negative index materials, the sign of the refractive index is ignored.

3.1. Spectral LDOS distributions

Spectral distributions of LDOS are calculated using Eq. (4) at distances Δ = 100, 200, and 500 nm from the metallic-based metamaterial and are presented in Fig. 2(a). Fig. 2(b) shows the same for the dielectric-based metamaterial with Δ = 10, 50, and 100 nm. The LDOS is compared with far-field and blackbody distributions in both figures.

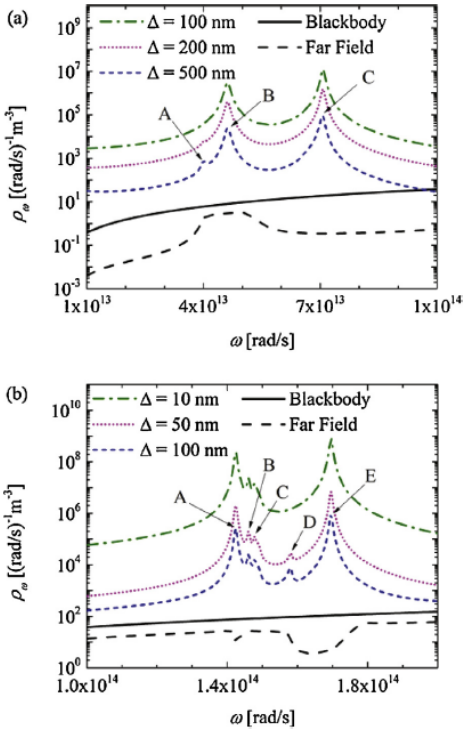

Fig. 2. Spectral LDOS of (a) metallic-based metamaterial calculated at Δ = 100, 200, and 500 nm, and (b) dielectric-based metamaterial calculated at Δ = 10, 50, and 100 nm. Far-field and blackbody distributions are also shown.

Resonance peaks are located at 4.63×10^{13} (B) and 7.07×10^{13} rad/s (C) for the metallic-based metamaterial. For the dielectric-based metamaterial, resonances are found at 1.43×10^{14} (A) and 1.70×10^{14} rad/s (E). All resonances are accompanied by a relative decrease in far-field emission with the exception of peak B for the metallic-based metamaterial. Both metamaterials also display a smaller peak that is more pronounced at larger Δ. The metallic metamaterial shows this phenomenon at 4.00×10^{13} rad/s (A), while a similar peak is located at 1.58×10^{14} rad/s (D) with the dielectric metamaterial. A pair of other smaller peaks at 1.46×10^{14} (B) and 1.48×10^{14} rad/s (C) appears for the dielectric metamaterial LDOS.

The physics behind the LDOS profiles provided in Fig. 2(a) and (b) can be better explained by analyzing the dispersion relations, as discussed below.

3.2. Dispersion relations

Dispersion relation analyses have been conducted while neglecting losses [23–25,63]. The following discussion presents an alternative method for performing SP dispersion relations while accounting for losses. SP dispersion relations are derived by exploring boundary conditions for Maxwell's equations [63], which state that the tangential component of the electromagnetic field across an interface is continuous (for TM polarization):

$$\varepsilon_1\gamma_0 + \varepsilon_0\gamma_1 = 0 \tag{11}$$

where

$$\gamma_j = -ik_{zj} = \sqrt{k_\rho^2 - n_j^2 k_v^2} \tag{12}$$

Including the complex refractive index n_j in this definition of γ_j is the heart of the lossy dispersion relation analysis since $\sqrt{\varepsilon_j'\mu_j'}$ has been used instead.

Herein, a SP is defined as an electromagnetic field that decays exponentially normal to and away from an interface in both directions. Therefore, SPs exist when both k_{z0} and k_{z1} are purely imaginary numbers or, equivalently, when both γ_0 and γ_1 are purely real and positive:

$$\gamma_0' > 0 \quad \text{and} \quad \gamma_0'' = 0 \tag{13a}$$

$$\gamma_1' > 0 \quad \text{and} \quad \gamma_1'' = 0 \tag{13b}$$

From Eq. (12), it can be seen that this is impossible, as a purely lossless medium does not exist. Additionally, a lossless medium results in zero thermal emission. However, it is safe to assume that if losses are small

enough, the significant enhancement of LDOS in the near field, characteristic of a SP, is still feasible:

$$\gamma_0' > 0 \quad \text{and} \quad \gamma_0'' \ll \gamma_0' \tag{14a}$$

$$\gamma_1' > 0 \quad \text{and} \quad \gamma_1'' \ll \gamma_1' \tag{14b}$$

From this point forward, the derivation is specialized for the case of a lossless receiving medium 1. Using Eq. (12) with $j = 1$ and $n_1 = n_1'$, Eq. (14b) is satisfied when $k_\rho > n_1' k_v$. On the other hand, Eq. (14a) is not so easily satisfied since it involves a lossy medium. By applying $j = 0$ and $n_0 = n_0' + in_0''$ to Eq. (12), and after some straightforward algebra, the result is as follows:

$$\gamma_0 = \gamma_0' + i\gamma_0'' \tag{15}$$

where

$$\gamma_0' = \sqrt{\frac{\sqrt{g^2 + h^2} + g}{2}} \tag{16a}$$

$$\gamma_0'' = \operatorname{sgn}(h)\sqrt{\frac{\sqrt{g^2 + h^2} - g}{2}} \tag{16b}$$

and

$$g = k_\rho^2 - ({n_0'}^2 - n_0''^2)k_v^2 \tag{16c}$$

$$h = -2n_0' n_0'' k_v^2 \tag{16d}$$

In order to satisfy Eq. (13a), h must equal zero. Just as before, this is not possible. Instead, a less stringent requirement can be applied with similar results, i.e., $h \ll g$. Therefore, *a SP cannot be sustained on the surface of a medium 0 within frequency bands where $n_0' n_0''$ is not close to zero.*

By expanding Eq. (11), it is easily seen that the following are also necessary conditions for the existence of SPs:

$$\varepsilon_0'' = 0 \tag{17a}$$

$$\varepsilon_1' \gamma_0 + \varepsilon_0' \gamma_1 = 0 \tag{17b}$$

Again, just as with Eqs. (13a) and (13b), Eq. (17a) is not possible. However, a relaxed requirement such as:

$$\varepsilon_0'' \ll |\varepsilon_0'| \tag{18}$$

is sufficient. This condition is independent of substrate thickness [64]. Therefore, *a TM-polarized SP cannot be sustained on the surface of a medium 0 within frequency bands where ε_0'' is not close to zero.*

The requirement described by Eq. (17b) can only be satisfied when $\varepsilon_0' \varepsilon_1' < 0$ since $\gamma_j > 0$. Substituting Eq. (12) into Eq. (17b) reveals the SP dispersion relation in terms of k_ρ:

$$k_\rho^2 = k_v^2 \frac{\varepsilon_0'^2 {n_1'}^2 - \varepsilon_1'^2 ({n_0'}^2 - n_0''^2)}{\varepsilon_0'^2 - \varepsilon_1'^2} \tag{19}$$

where it is assumed that $n_0' n_0'' \to 0$. *A TM-polarized SP cannot be sustained along a medium 0–1 interface unless Eq. (19) is satisfied.*

When it is assumed that medium 1 is vacuum, as done in this paper, substituting the dispersion relation back into Eq. (12) gives:

$$\gamma_0^2 = k_v^2 \frac{\varepsilon_0'^2 [1 - ({n_0'}^2 - n_0''^2)]}{\varepsilon_0'^2 - 1} \tag{20}$$

Here, since medium 1 is a vacuum, ε_0' must be negative for TM-polarized SPs to exist. In order that $\gamma_0^2 > 0$, either of the two following conditions must be satisfied:

$$|\varepsilon_0'| < 1 \text{ and } {n_0'}^2 - n_0''^2 > 1 \tag{21a}$$

$$|\varepsilon_0'| > 1 \text{ and } {n_0'}^2 - n_0''^2 < 1 \tag{21b}$$

Finally, *with vacuum as the receiving medium, Eq. (21a) or Eq. (21b) must be satisfied for a TM-polarized SP to exist, given that $\varepsilon_0' < 0$.*

The above discussion is equally applicable in TE polarization when ε terms are replaced with μ. It is therefore easy to understand that SPs cannot be excited in TE polarization for nonmagnetic materials.

It is important to establish a few points of interest concerning SP dispersion relations to aid in the discussion of the results. The light lines for both the emitter ($k_e = \sqrt{{n_0'}^2 - n_0''^2}\omega/c_v$) and vacuum ($k_v = \omega/c_v$) are included in the dispersion relation charts. Assuming the emitter light line is greater than that of vacuum ($k_e > k_v$), waves found to the left of the light line in vacuum ($k_\rho < k_v$) are propagating on both sides of the interface 0–1. Between the two light lines ($k_v < k_\rho < k_e$), waves experience TIR at the interface 0–1 where they propagate back into the emitter while being evanescent in the vacuum. To the right of the light line in the emitter ($k_\rho > k_e$), waves are evanescent on both sides of the interface such that SPs may exist in this region. When the emitter light line is found to the left of the vacuum light line ($k_e < k_v$), its refractive index is less than unity, eliminating the generation of evanescent waves via TIR. For this case, waves are evanescent on both sides of the interface to the right of the light line in vacuum ($k_\rho > k_v$).

It is also important to make the distinction between a SP and a resonance of the LDOS. Resonance of the LDOS occurs when a large number of modes k_ρ exist

within a narrow spectral band ($|dk_\rho/d\omega| \to \infty$). The denominator of Eq. (19) shows that when medium 1 is a vacuum, $k_\rho \to \infty$ when $\varepsilon_0' = -1$ (TM polarization) or $\mu_0' = -1$ (TE polarization), defining the existence of LDOS resonance.

The real parts of the permittivity and permeability of the metallic-based metamaterial are compared with $n_0'^2 - n_0''^2$ to explore the domain of existence of SPs in Fig. 3(a) (see Eqs. (21a) and (21b)). The spectral LDOS per unit k_ρ at $\Delta = 100$ nm is shown in Fig. 3(b). To appropriately analyze the SP dispersion relation, $n_0'n_0''$ and the imaginary parts of the permittivity and permeability are charted in Fig. 3(c).

Fig. 3(a) shows that $\varepsilon_0' = -1$ at 7.07×10^{13} rad/s and $\mu_0' = -1$ at 4.01×10^{13} and 4.63×10^{13} rad/s. From the dispersion relation in Fig. 3(b), it is apparent that these frequencies are aligned with significant $|dk_\rho/d\omega|$, showing that they are, indeed, candidate resonances. However, the TE-polarized asymptote at 4.01×10^{13} rad/s does not demonstrate significant LDOS (see Fig. 2(a)) as explained in Fig. 3(c). The large μ_0'' and $n_0'n_0''$ both result in a violation of Eq. (14a) and the TE-polarized equivalent of Eq. (18), showing that this phenomenon can be considered neither a SP nor a LDOS resonance. Therefore, the other two asymptotes only are considered resonances, which agree well with the values calculated with the spectral LDOS shown in Fig. 2(a).

This metamaterial results in negative refraction between 3.31×10^{13} and 7.95×10^{13} rad/s. A locally large k_e value (and, hence, index of refraction) peaks at 4.05×10^{13} rad/s where the emitter light line is larger than the vacuum light line. Significant LDOS is found within this TIR region, explaining peak A observed in the spectral LDOS (Fig. 2(a)) for large Δ. However, as Δ decreases the LDOS due to evanescent waves generated by TIR is overcome by the enormous LDOS contribution from the neighboring LDOS resonance.

The low-frequency LDOS resonance (4.63×10^{13} rad/s) is found within this bandwidth of relatively large negative index of refraction. This resonance corresponds with a highly absorptive region in the far field (see Fig. 2(a)), which is atypical of nonmagnetic materials such as SiC. For nonmagnetic media, LDOS resonance arises when $\varepsilon_0' = -1$ and $\varepsilon_0'' \ll |\varepsilon_0'|$. Therefore, since the phase angles $\phi_{\varepsilon,0} (= \arctan(\varepsilon_0''/\varepsilon_0')) \to \pi$ and $\phi_{\mu,0} (= \arctan(\mu_0''/\mu_0')) = 0$, the refractive index ($n_0 = \sqrt{|\varepsilon_0||\mu_0|}(\cos\phi_{n,0} + i\sin\phi_{n,0})$, where $\phi_{n,0} = (\phi_{\varepsilon,0} + \phi_{\mu,0})/2$) nearly becomes a purely imaginary number ($n_0 \to i\sqrt{|\varepsilon_0||\mu_0|}$), thus leading to a highly reflecting bandwidth in the far field. As shown in Fig. 3(a) and (c), the low-frequency resonance of the LDOS is due to SPs in TE polarization where $\varepsilon_0' < -1$ and $\mu_0' = -1$, and where ε_0'' and ε_0'' are small. Assuming that both $\varepsilon_0'' \ll |\varepsilon_0'|$ and $\mu_0'' \ll |\mu_0'|$, both phases $\phi_{\varepsilon,0}$ and $\phi_{\mu,0}$ tend to π, and the refractive index is thus negative and almost a purely real number ($n_0 \to -\sqrt{|\varepsilon_0||\mu_0|}$) resulting in a spectral band of high absorption in the far field, as observed in Fig. 2(a).

Another group of SPs results from the dispersion relation analysis that peaks at 3.95×10^{13} rad/s. However, it never reaches a resonance, i.e., $|dk_\rho/d\omega|$ does not tend to infinity. As seen in Fig. 3(b), the LDOS due to these nonresonant SPs is not negligible; however, neither is it sufficient to generate a peak in the spectral LDOS (see Fig. 2(a)). Instead, its contribution is merged with that of the neighboring TIR region and resonance.

In order to explore the domain of existence of SPs in the dielectric-based metamaterial, the real parts of the permittivity and permeability are charted and compared with $n_0'^2 - n_0''^2$ in Fig. 4(a). Fig. 4(b) shows the spectral LDOS per unit k_ρ at $\Delta = 100$ nm. The imaginary parts of the permittivity and permeability and $n_0'n_0''$ are shown in Fig. 4(c).

As seen in Fig. 4(a), $\varepsilon_0' = -1$ at 1.58×10^{14} and 1.70×10^{14} rad/s and $\mu_0' = -1$ at 1.41×10^{14} and 1.43×10^{14} rad/s. The dispersion relation in Fig. 4(b) shows that these frequencies are coincident with marked $|dk_\rho/d\omega|$. However, neither the TM- nor the TE-polarized asymptote, at 1.41×10^{14} and 1.58×10^{14} rad/s, respectively, is aligned with significant LDOS. Inspection of Fig. 4(c) reveals that at both of these frequencies significant losses are found – permittivity losses at the TM-polarized asymptote frequency and permeability losses at the TE-polarized asymptote – showing that neither of these asymptotes leads to LDOS resonance. The remaining two asymptotes (at 1.43×10^{14} and 1.70×10^{14} rad/s) are considered resonances, which agree well with the spectral LDOS results (see Fig. 2(b)).

This dielectric-based metamaterial does not show any negative refraction over the analyzed spectral band. There are two regions of significant TIR in Fig. 4(b), where the emitter light line k_e peaks at 1.41×10^{14} and 1.58×10^{14} rad/s. The former k_e peak does align with significant LDOS in the contour. However, as seen in Fig. 2(b), it never forms a peak of its own in the spectral LDOS. Instead, the influence on the LDOS of this TIR region is dominated by the neighboring SP at 1.43×10^{14} rad/s.

As mentioned in Section 3.1, two additional peaks (B and C) are found in Fig. 2(b). These peaks align well with significant LDOS in Fig. 4(b) found at 1.46×10^{14}

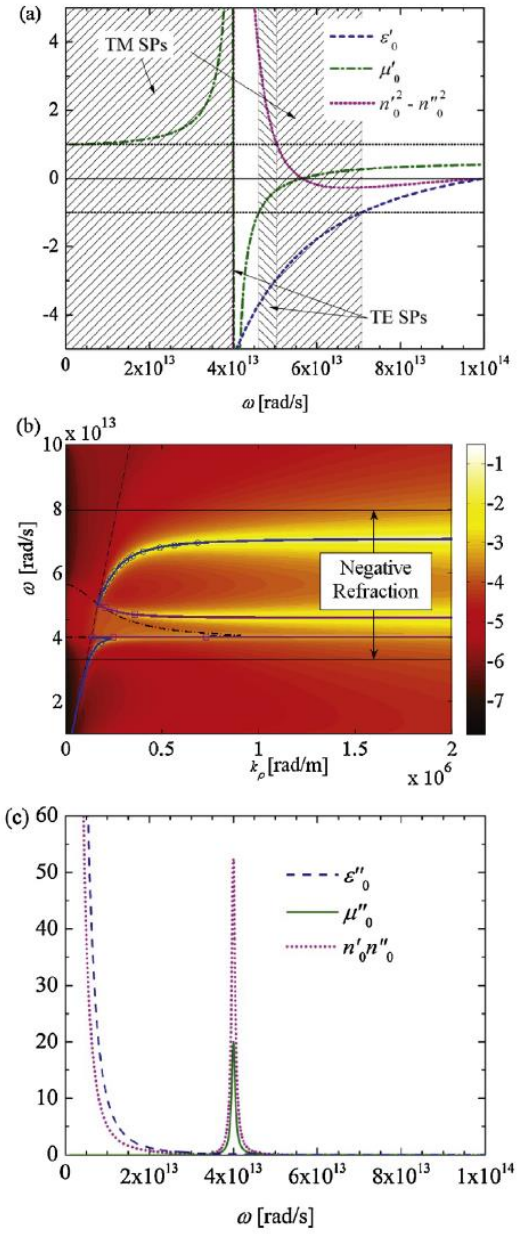

Fig. 3. (a) SP domain of existence for the metallic-based metamaterial; (b) dispersion relation – vacuum light line (black dash), emitter light line (black dash-dot), TM SPs (blue circle), and TE SPs (pink square) – and spectral LDOS per unit $k_\rho(\log(\rho_{\omega k_\rho}))$ at 100 nm from the surface; (c) losses of the metamaterial. (For interpretation of the references to color in this figure legend, the reader is referred to the web version of this article.)

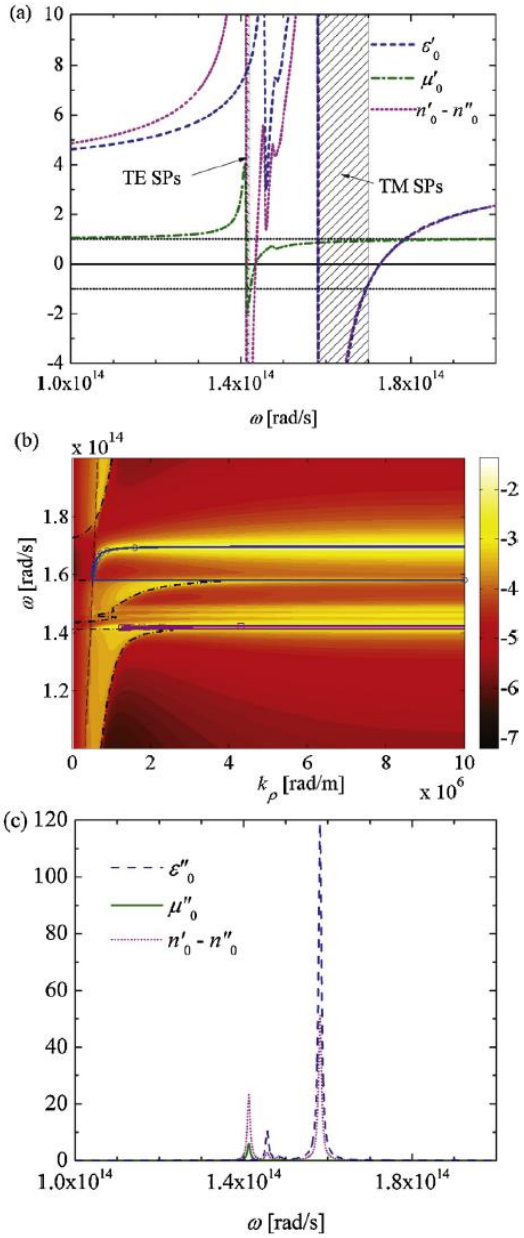

Fig. 4. (a) SP domain of existence for the dielectric-based metamaterial; (b) dispersion relation – vacuum light line (black dash), emitter light line (black dash-dot), TM SPs (blue circle), and TE SPs (pink square) – and spectral LDOS per unit $k_\rho(\log(\rho_{\omega k_\rho}))$ at 100 nm from the surface; (c) losses in the metamaterial. (For interpretation of the references to color in this figure legend, the reader is referred to the web version of this article.)

and 1.48×10^{14} rad/s, and persist in the near field regardless of Δ, a behavior characteristic of LDOS resonance. Observation of Fig. 4(a) shows that the real part of both the permittivity and permeability experience some nearly asymptotic behavior ($d\varepsilon_0'/d\omega$ and $d\mu_0'/d\omega$ are relatively large) at these frequencies. However, the corresponding losses (see Fig. 4(c)) damp the permittivity and permeability sufficiently to prevent $\varepsilon_0' = -1$ and $\mu_0' = -1$. Therefore, these LDOS peaks are due to neither LDOS resonance nor SPs, rather, a resonance-like phenomenon.

4. Conclusions

A closed form expression for the local density of electromagnetic states (LDOS) due to thermal emission of a metamaterial bulk was derived. The generality of the derivation makes this expression equally applicable to any material of arbitrary electric permittivity and magnetic permeability. The equation is identical to that of nonmagnetic media, with differences arising only in the Fresnel reflection coefficients where the permeability terms are found. An asymptotic analysis of this equation showed a Δ^{-3} power law relationship between the LDOS and the distance from the emitting bulk Δ, as for nonmagnetic materials. Using the LDOS expression and the effective medium theory (EMT), resonances in both TM and TE polarizations were predicted for two metamaterials: a metallic-based metamaterial consisting of an array of split-ring resonators and wires, and a dielectric-based metamaterial made up of silicon carbide spheres in a potassium bromide host medium.

The physics of surface polariton (SP) mediated near-field thermal emission was thoroughly explored by applying a dispersion relation analysis which accounts for losses. This study demonstrated mathematically that SPs cannot be excited if the imaginary parts of the permittivity and the permeability, as well as $n'n''$, are not close to zero, where n' and n'' are respectively the real and imaginary parts of the refractive index. Additionally, the spectral LDOS per unit tangential wavevector k_ρ was shown to align perfectly with the dispersion relation analysis for both metamaterials, explaining LDOS enhancements due to both the excitation of SPs and the real parts of permittivity or permeability approaching -1.

The validity of the EMT in the near field of metamaterials made of three-dimensional meta-atoms is questionable. But this approach is the only tool currently available for predicting near-field thermal emission by particulate media. The trends observed in this paper will provide significant insights into the near-field capabilities of metamaterials, and will eventually assist in assessing the validity of the EMT in the near field when direct calculation of near-field thermal emission by particulate media is possible.

Appendix

The derivation of the explicit, closed form expression for the LDOS due to thermal emission of a metamaterial emitting into vacuum is shown here. The aim is to determine the LDOS at a distance Δ from a semi-infinite layer according to the configuration shown in Fig. 1.

Eq. (3) is where the derivation starts, in which the near-field energy density is written in terms of the Weyl components of the DGFs. The LDOS is obtained by dividing Eq. (3) by the mean energy of an electromagnetic state $\Theta(\omega, T_0)$. The following general expression for the monochromatic LDOS is obtained by performing the double summation over α and β in Eq. (3):

$$\begin{aligned}\rho_\omega(\Delta) = \frac{k_v^2}{2\pi^2\omega}\int_{k_\rho=0}^{\infty} k_\rho dk_\rho \int_{z'=-\infty}^{0} \{\varepsilon_0''[k_v^2|\mu_0|^2(|g_{\rho\rho}^{Ee}|^2 \\ + |g_{\rho z}^{Ee}|^2 + |g_{\theta\theta}^{Ee}|^2 + |g_{z\rho}^{Ee}|^2 + |g_{zz}^{Ee}|^2) \\ + (|g_{\rho\theta}^{He}|^2 + |g_{\theta\rho}^{He}|^2 + |g_{\theta z}^{He}|^2 + |g_{z\theta}^{He}|^2)] \\ + \mu_0''[(|g_{\rho\theta}^{Em}|^2 + |g_{\theta\rho}^{Em}|^2 + |g_{\theta z}^{Em}|^2 + |g_{z\theta}^{Em}|^2) \\ + k_v^2|\varepsilon_0|^2(|g_{\rho\rho}^{Hm}|^2 + |g_{\rho z}^{Hm}|^2 + |g_{\theta\theta}^{Hm}|^2 + |g_{z\rho}^{Hm}|^2 \\ + |g_{zz}^{Hm}|^2)]\} dz'\end{aligned} \tag{A1}$$

The Weyl components contributing to the LDOS in vacuum (medium 1) near a semi-infinite bulk (medium 0) are given explicitly hereafter.

Electric field due to electric dipole oscillations:

$$g_{\rho\rho}^{Ee}(k_\rho, \Delta, z', \omega) = \frac{ik_{z1}}{2k_0k_1} t_{01}^{TM} e^{i(k_{z1}\Delta - k_{z0}z')} \tag{A2a}$$

$$g_{\rho z}^{Ee}(k_\rho, \Delta, z', \omega) = -\frac{ik_{z1}k_\rho}{2k_0k_1k_{z0}} t_{01}^{TM} e^{i(k_{z1}\Delta - k_{z0}z')} \tag{A2b}$$

$$g_{\theta\theta}^{Ee}(k_\rho, \Delta, z', \omega) = \frac{i}{2k_{z0}} t_{01}^{TE} e^{i(k_{z1}\Delta - k_{z0}z')} \tag{A2c}$$

$$g_{z\rho}^{Ee}(k_\rho, \Delta, z', \omega) = -\frac{ik_\rho}{2k_0k_1} t_{01}^{TM} e^{i(k_{z1}\Delta - k_{z0}z')} \tag{A2d}$$

$$g_{zz}^{Ee}(k_\rho, \Delta, z', \omega) = \frac{ik_\rho^2}{2k_0k_1k_{z0}} t_{01}^{TM} e^{i(k_{z1}\Delta - k_{z0}z')} \tag{A2e}$$

Magnetic field due to electric dipole oscillations:

$$g^{He}_{\rho\theta}(k_\rho,\Delta,z',\omega)=\frac{\mu_0 k_{z1}}{2\mu_1 k_{z0}}t^{TE}_{01}e^{i(k_{z1}\Delta-k_{z0}z')} \tag{A3a}$$

$$g^{He}_{\theta\rho}(k_\rho,\Delta,z',\omega)=-\frac{\mu_0 k_1}{2\mu_1 k_0}t^{TM}_{01}e^{i(k_{z1}\Delta-k_{z0}z')} \tag{A3b}$$

$$g^{He}_{\theta z}(k_\rho,\Delta,z',\omega)=\frac{\mu_0 k_1 k_\rho}{2\mu_1 k_0 k_{z0}}t^{TM}_{01}e^{i(k_{z1}\Delta-k_{z0}z')} \tag{A3c}$$

$$g^{He}_{z\theta}(k_\rho,\Delta,z',\omega)=-\frac{\mu_0 k_\rho}{2\mu_1 k_{z0}}t^{TE}_{01}e^{i(k_{z1}\Delta-k_{z0}z')} \tag{A3d}$$

Electric field due to magnetic dipole oscillations:

$$g^{Em}_{\rho\theta}(k_\rho,\Delta,z',\omega)=-\frac{k_0 k_{z1}}{2k_1 k_{z0}}t^{TM}_{01}e^{i(k_{z1}\Delta-k_{z0}z')} \tag{A4a}$$

$$g^{Em}_{\theta\rho}(k_\rho,\Delta,z',\omega)=\frac{1}{2}t^{TE}_{01}e^{i(k_{z1}\Delta-k_{z0}z')} \tag{A4b}$$

$$g^{Em}_{\theta z}(k_\rho,\Delta,z',\omega)=-\frac{k_\rho}{2k_{z0}}t^{TE}_{01}e^{i(k_{z1}\Delta-k_{z0}z')} \tag{A4c}$$

$$g^{Em}_{z\theta}(k_\rho,\Delta,z',\omega)=\frac{k_0 k_\rho}{2k_1 k_{z0}}t^{TM}_{01}e^{i(k_{z1}\Delta-k_{z0}z')} \tag{A4d}$$

Magnetic field due to magnetic dipole oscillations:

$$g^{Hm}_{\rho\rho}(k_\rho,\Delta,z',\omega)=\frac{in_0 n_1 k_{z1}}{2\varepsilon_0\mu_1 k_0 k_1}t^{TE}_{01}e^{i(k_{z1}\Delta-k_{z0}z')} \tag{A5a}$$

$$g^{Hm}_{\rho z}(k_\rho,\Delta,z',\omega)=-\frac{in_0 n_1 k_{z1}k_\rho}{2\varepsilon_0\mu_1 k_0 k_1 k_{z0}}t^{TE}_{01}e^{i(k_{z1}\Delta-k_{z0}z')} \tag{A5b}$$

$$g^{Hm}_{\theta\theta}(k_\rho,\Delta,z',\omega)=\frac{in_0 n_1}{2\varepsilon_0\mu_1 k_{z0}}t^{TM}_{01}e^{i(k_{z1}\Delta-k_{z0}z')} \tag{A5c}$$

$$g^{Hm}_{z\rho}(k_\rho,\Delta,z',\omega)=-\frac{in_0 n_1 k_\rho}{2\varepsilon_0\mu_1 k_0 k_1}t^{TE}_{01}e^{i(k_{z1}\Delta-k_{z0}z')} \tag{A5d}$$

$$g^{Hm}_{zz}(k_\rho,\Delta,z',\omega)=\frac{in_0 n_1 k_\rho^2}{2\varepsilon_0\mu_1 k_0 k_1 k_{z0}}t^{TE}_{01}e^{i(k_{z1}\Delta-k_{z0}z')} \tag{A5e}$$

where $t^{TM(TE)}_{01}$ is the Fresnel transmission coefficient at the interface 0–1 in TM (TE) polarization.

By substituting the appropriate Weyl components of the DGFs and integrating over the emitter volume, Eq. (A1) results in the following TM and TE polarization terms for each of the components (*Ee*, *He*, *Em*, *Hm*):

$$|g^{Ee}_{\rho\rho}|^2+|g^{Ee}_{\rho z}|^2+|g^{Ee}_{z\rho}|^2+|g^{Ee}_{zz}|^2=\frac{1}{8|n_0|^2k_v^4k''_{z0}}\times\left(|k_{z1}|^2+\frac{|k_{z1}|^2k_\rho^2}{|k_{z0}|^2}+k_\rho^2+\frac{k_\rho^4}{|k_{z0}|^2}\right)|t^{TM}_{01}|^2e^{-2k''_{z1}\Delta} \tag{A6a}$$

$$|g^{Ee}_{\theta\theta}|^2=\frac{1}{8k''_{z0}|k_{z0}|^2}|t^{TE}_{01}|^2e^{-2k''_{z1}\Delta} \tag{A6b}$$

$$|g^{He}_{\theta\rho}|^2+|g^{He}_{\theta z}|^2=\frac{|\mu_0|^2}{8|n_0|^2k''_{z0}}\left(1+\frac{k_\rho^2}{|k_{z0}|^2}\right)|t^{TM}_{01}|^2e^{-2k''_{z1}\Delta} \tag{A6c}$$

$$|g^{He}_{\rho\theta}|^2+|g^{He}_{z\theta}|^2=\frac{|\mu_0|^2}{8k''_{z0}|k_{z0}|^2}(|k_{z1}|^2+k_\rho^2)|t^{TE}_{01}|^2e^{-2k''_{z1}\Delta} \tag{A6d}$$

$$|g^{Em}_{\rho\theta}|^2+|g^{Em}_{z\theta}|^2=\frac{|n_0|^2}{8k''_{z0}|k_{z0}|^2}(|k_{z1}|^2+k_\rho^2)|t^{TM}_{01}|^2e^{-2k''_{z1}\Delta} \tag{A6e}$$

$$|g^{Em}_{\theta\rho}|^2+|g^{Em}_{\theta z}|^2=\frac{1}{8k''_{z0}}\left(1+\frac{k_\rho^2}{|k_{z0}|^2}\right)|t^{TE}_{01}|^2e^{-2k''_{z1}\Delta} \tag{A6f}$$

$$|g^{Hm}_{\theta\theta}|^2=\frac{|n_0|^2}{8|\varepsilon_0|^2k''_{z0}|k_{z0}|^2}|t^{TM}_{01}|^2e^{-2k''_{z1}\Delta} \tag{A6g}$$

$$|g^{Hm}_{\rho\rho}|^2+|g^{Hm}_{\rho z}|^2+|g^{Hm}_{z\rho}|^2+|g^{Hm}_{zz}|^2=\frac{1}{8k_v^4k''_{z0}}\times\left(|k_{z1}|^2+\frac{|k_{z1}|^2k_\rho^2}{|k_{z0}|^2}+k_\rho^2+\frac{k_\rho^4}{|k_{z0}|^2}\right)|t^{TE}_{01}|^2e^{-2k''_{z1}\Delta} \tag{A6h}$$

Algebraic operations on Eqs. (A6a)–(A6h) are performed while making the following distinction between propagating and evanescent waves. For $k_\rho\le k_v$, the z-component of the wavevector in vacuum is purely real, i.e., $k_{z1}=k'_{z1}$, such that waves are propagating in vacuum. For $k_\rho>k_v$, waves are evanescent in vacuum and the z-component of the wavevector is purely imaginary, i.e., $k_{z1}=ik''_{z1}$. Additionally, a number of useful identities are required for the algebraic manipulations:

$$2k'_{zi}k''_{zi}=(\varepsilon'_i\mu''_i+\varepsilon''_i\mu'_i)k_v^2 \tag{A7a}$$

$$k'_{zi}(|k_{zi}|^2 + k_\rho^2) = k_v^2 \mathrm{Re}(\varepsilon_i \mu_i k^*_{zi}) \tag{A7b}$$

$$k''_{zi}(|k_{zi}|^2 - k_\rho^2) = k_v^2 \mathrm{Im}(\varepsilon_i \mu_i k^*_{zi}) \tag{A7c}$$

$$\left|\frac{\varepsilon_j \mu_i}{\varepsilon_i \mu_j}\right| \frac{\mathrm{Re}(\varepsilon_i \mu_i k^*_{zi})}{|k_{zi}|^2} |t_{ij}^{TM}|^2 = \frac{1}{|k_{zj}|^2}[\mathrm{Re}(\varepsilon_j \mu_i k^*_{zj})(1 - |r_{ij}^{TM}|^2) + 2\mathrm{Im}(\varepsilon_j \mu_i k^*_{zj})\mathrm{Im}(r_{ij}^{TM})] \tag{A7d}$$

$$\frac{|\mu_i|^2 k'_{zi}}{|k_{zi}|^2} |t_{ij}^{TE}|^2 = \frac{1}{|k_{zj}|^2}[\mathrm{Re}(\mu_i^* \mu_j k^*_{zj})(1 - |r_{ij}^{TE}|^2) + 2\mathrm{Im}(\mu_i^* \mu_j k^*_{zj})\mathrm{Im}(r_{ij}^{TE})] \tag{A7e}$$

$$\left|\frac{\varepsilon_i \varepsilon_j \mu_i}{\mu_j}\right| \frac{k'_{zi}}{|k_{zi}|^2} |t_{ij}^{TM}|^2 = \frac{1}{|k_{zj}|^2}[\mathrm{Re}(\varepsilon_i^* \varepsilon_j k^*_{zj})(1 - |r_{ij}^{TM}|^2) + 2\mathrm{Im}(\varepsilon_i^* \varepsilon_j k^*_{zj})\mathrm{Im}(r_{ij}^{TM})] \tag{A7f}$$

$$\frac{\mathrm{Re}(\varepsilon_i \mu_i k^*_{zi})}{|k_{zi}|^2} |t_{ij}^{TE}|^2 = \frac{1}{|k_{zj}|^2}[\mathrm{Re}(\varepsilon_i \mu_j k^*_{zj})(1 - |r_{ij}^{TE}|^2) + 2\mathrm{Im}(\varepsilon_i \mu_j k^*_{zj})\mathrm{Im}(r_{ij}^{TE})] \tag{A7g}$$

The propagating and evanescent component equations for LDOS due to electric and magnetic dipole oscillations are found by substituting Eqs. (A6a)–(A6h) into Eq. (A1), and by applying the appropriate algebraic manipulations using the identities given by Eqs. (A7a)–(A7g):

$$\rho^e_{\omega,prop} = \frac{1}{4\pi^2 \omega} \frac{\varepsilon_0'' k_v^2}{\varepsilon_0' \mu_0'' + \varepsilon_0'' \mu_0'} \int_0^{k_v} \frac{k_\rho dk_\rho}{|k_{z1}|} \{\mu_0'[(1 - |r_{10}^{TE}|^2) + (1 - |r_{10}^{TM}|^2)] + 2\mu_0''[\mathrm{Im}(r_{10}^{TE}) - \mathrm{Im}(r_{10}^{TM})]\} \tag{A8a}$$

$$\rho^e_{\omega,evan}(\Delta) = \frac{1}{4\pi^2 \omega} \frac{\varepsilon_0''}{\varepsilon_0' \mu_0'' + \varepsilon_0'' \mu_0'} \int_{k_v}^{\infty} \frac{k_\rho^3 dk_\rho}{|k_{z1}|} \times \{\mu_0''[(1 - |r_{10}^{TM}|^2) - (1 - |r_{10}^{TE}|^2)] + 2\mu_0'[\mathrm{Im}(r_{10}^{TM}) + \mathrm{Im}(r_{10}^{TE})]\} e^{-2|k_{z1}|\Delta} \tag{A8b}$$

$$\rho^m_{\omega,prop} = \frac{1}{4\pi^2 \omega} \frac{\mu_0'' k_v^2}{\varepsilon_0' \mu_0'' + \varepsilon_0'' \mu_0'} \int_0^{k_v} \frac{k_\rho dk_\rho}{|k_{z1}|} \times \{\varepsilon_0'[(1 - |r_{10}^{TM}|^2) + (1 - |r_{10}^{TE}|^2)] + 2\varepsilon_0''[\mathrm{Im}(r_{10}^{TM}) - \mathrm{Im}(r_{10}^{TE})]\} \tag{A8c}$$

$$\rho^m_{\omega,evan}(\Delta) = \frac{1}{4\pi^2 \omega} \frac{\mu_0''}{\varepsilon_0' \mu_0'' + \varepsilon_0'' \mu_0'} \int_{k_v}^{\infty} \frac{k_\rho^3 dk_\rho}{|k_{z1}|} \times \{\varepsilon_0''[(1 - |r_{10}^{TE}|^2) - (1 - |r_{10}^{TM}|^2)] + 2\varepsilon_0'[\mathrm{Im}(r_{10}^{TE}) + \mathrm{Im}(r_{10}^{TM})]\} e^{-2|k_{z1}|\Delta} \tag{A8d}$$

where the superscripts e and m specify whether the LDOS is due to the electric or magnetic dipole oscillations, respectively, while the subscripts *prop* and *evan* specify whether the LDOS is a result of propagating or evanescent waves. For nonmagnetic materials, i.e., $\mu_0 = 1$, Eqs. (A8c) and (A8d) are equal to zero meaning that there is no contribution from magnetic dipole oscillations to thermal emission. Additionally, for nonmagnetic materials, the term $\varepsilon_0''/(\varepsilon_0' \mu_0'' + \varepsilon_0'' \mu_0')$ converges to unity in Eqs. (A8a) and (A8b).

A summation of each of the electric and magnetic components results in a closed-form expression of the LDOS:

$$\rho_{\omega,prop} = \frac{k_v^2}{4\pi^2 \omega} \int_0^{k_v} \frac{k_\rho dk_\rho}{|k_{z1}|}[(1 - |r_{10}^{TM}|^2) + (1 - |r_{10}^{TE}|^2)] \tag{A9a}$$

$$\rho_{\omega,evan}(\Delta) = \frac{1}{2\pi^2 \omega} \int_{k_v}^{\infty} \frac{k_\rho^3 dk_\rho}{|k_{z1}|} [\mathrm{Im}(r_{10}^{TM}) + \mathrm{Im}(r_{10}^{TE})] \times e^{-2|k_{z1}|\Delta} \tag{A9b}$$

The LDOS given by Eq. (4) in Section 2 is the summation of contributions from propagating waves (Eq. (A9a)) and evanescent waves (Eq. (A9b)).

References

[1] S. Basu, Z.M. Zhang, C.J. Fu, Review of near-field radiation and its application to energy conversion, International Journal of Energy Research 33 (2009) 1203–1232.

[2] J.R. Howell, R. Siegel, M.P. Mengüç, Thermal Radiation Heat Transfer, 5th ed., CRC Press, Boca Raton, 2011.

[3] C.R. Otey, W.T. Lau, S. Fan, Thermal rectification through vacuum, Physical Review Letters 104 (15) (2010) 154301.

[4] S. Basu, M. Francoeur, Near-field radiative transfer based thermal rectification using doped silicon, Applied Physics Letters 98 (2011) 113106.

[5] H. Iizuka, S. Fan, Rectification of evanescent heat transfer between dielectric-coated and uncoated silicon carbide plates, Journal of Applied Physics 112 (2012) 024304.

[6] L. Zhu, C.R. Otey, S. Fan, Negative differential thermal conductance through vacuum, Applied Physics Letters 100 (2012) 044104.

[7] Y. De Wilde, F. Formanek, R. Carminati, B. Gralak, P.-A. Lemoine, K. Joulain, J.-P. Mulet, Y. Chen, J.-J. Greffet, Thermal radiation scanning tunneling microscopy, Nature 444 (2006) 740–743.

[8] R.S. DiMatteo, P. Greiff, S.L. Finberg, K.A. Young-Waithe, H.K.H. Choy, M.M. Masaki, C.G. Fonstad, Enhanced photogeneration of carriers in a semiconductor via coupling across a nonisothermal nanoscale vacuum gap, Applied Physics Letters 79 (2001) 1894–1896.

[9] M.D. Whale, E.G. Cravalho, Modeling and performance of microscale thermophotovoltaic energy conversion devices, IEEE Transactions on Energy Conversion 17 (2002) 130–142.

[10] M. Laroche, R. Carminati, J.-J. Greffet, Near-field thermophotovoltaic energy conversion, Journal of Applied Physics 100 (2006) 063704.

[11] K. Park, S. Basu, W.P. King, Z.M. Zhang, Performance analysis of near-field thermophotovoltaic devices considering absorption distribution, Journal of Quantitative Spectroscopy & Radiative Transfer 109 (2008) 305–316.

[12] M. Francoeur, R. Vaillon, M.P. Mengüç, Thermal impacts on the performance of nanoscale-gap thermophotovoltaic power generators, IEEE Transactions on Energy Conversion 26 (2011) 686–698.

[13] V.G. Veselago, The electrodynamics of substances with simultaneously negative values of ε and μ, Soviet Physics Uspekhi 10 (1968) 509–514.

[14] D.R. Smith, W.J. Padilla, D.C. Vier, S.C. Nemat-Nasser, S. Schulz, Composite medium with simultaneously negative permeability and permittivity, Physical Review Letters 84 (2000) 4184–4187.

[15] R.A. Shelby, D.R. Smith, S. Schultz, Experimental verification of a negative index of refraction, Science 292 (2001) 77–79.

[16] L. Solymar, E. Shamonina, Waves in Metamaterials, Oxford University Press, New York, 2009.

[17] W. Cai, V. Shalaev, Optical Metamaterials: Fundamentals and Applications, Springer, New York, 2010.

[18] C.J. Fu, Z.M. Zhang, D.B. Tanner, Planar heterogeneous structures for coherent emission of radiation, Optics Letters 30 (2005) 1873–1875.

[19] B.J. Lee, L.P. Wang, Z.M. Zhang, Coherent thermal emission by excitation of magnetic polaritons between periodic strips and metallic film, Optics Express 16 (2008) 11328–11336.

[20] C.J. Fu, Z.M. Zhang, Further investigation of coherent thermal emission from single negative materials, Nanoscale and Microscale Thermophysical Engineering 12 (2008) 83–97.

[21] J.A. Mason, S. Smith, D. Wasserman, Strong absorption and selective thermal emission from a midinfrared metamaterial, Applied Physics Letters 98 (2011) 241105.

[22] G. D'Aguanno, N. Mattiucci, A. Alù, C. Argyropoulos, J.V. Foreman, M.J. Bloemer, Thermal emission from a metamaterial wire medium slab, Optics Express 20 (2012) 9784–9789.

[23] K. Joulain, J. Drevillon, P. Ben-Abdallah, Noncontact heat transfer between two metamaterials, Physical Review B 81 (2010) 165119.

[24] Z. Zheng, Y. Xuan, Theory of near-field radiative heat transfer for stratified magnetic media, International Journal of Heat and Mass Transfer 54 (2011) 1101–1110.

[25] Z. Zheng, Y. Xuan, Near-field radiative heat transfer between general materials and metamaterials, Chinese Science Bulletin 56 (2011) 2312–2319.

[26] S. Basu, M. Francoeur, Penetration depth in near-field radiative heat transfer between metamaterials, Applied Physics Letters 99 (2011) 143107.

[27] M. Francoeur, S. Basu, S.J. Petersen, Electric and magnetic surface polariton mediated near-field radiative heat transfer between metamaterials made of silicon carbide particles, Optics Express 19 (2011) 18774–18788.

[28] D.R. Smith, D. Schurig, Electromagnetic wave propagation in media with indefinite permittivity and permeability tensors, Physical Review Letters 90 (2003) 077405.

[29] I.S. Nefedov, C.R. Simovski, Giant radiation heat transfer through micron gaps, Physical Review B 84 (2011) 195459.

[30] S.-A. Biehs, M. Tschikin, P. Ben-Abdallah, Hyperbolic metamaterials as an analog of a blackbody in the near field, Physical Review Letters 109 (2012) 104301.

[31] C.L. Cortes, W. Newman, S. Molesky, Z. Jacob, Quantum nanophotonics using hyperbolic metamaterials, Journal of Optics 14 (2012) 063001.

[32] Y. Guo, C.L. Cortes, S. Molesky, Z. Jacob, Broadband super-Planckian thermal emission from hyperbolic metamaterials, Applied Physics Letters 101 (2012) 131106.

[33] S.-A. Biehs, M. Tschikin, R. Messina, P. Ben-Abdallah, Super-Planckian near-field thermal emission with phonon-polaritonic hyperbolic metamaterials, 2013 arXiv:1302.3782v1.

[34] Y. Guo, Z. Jacob, Thermal hyperbolic metamaterials, 2013 arXiv:1302.2965v3.

[35] M. Tschikin, S.-A. Biehs, R. Messina, P. Ben-Abdallah, On the limits of the effective description of hyperbolic materials in presence of surface waves, 2013 arXiv:1302.3719v1.

[36] S.-A. Biehs, D. Reddig, M. Holthaus, Thermal radiation and near-field energy density of thin metallic films, European Physical Journal B 55 (2007) 237–251.

[37] K. Joulain, C. Henkel, The near-field correlation spectrum of a metallic film, Applied Physics B: Lasers and Optics 93 (2008) 151–158.

[38] P. Ben-Abdallah, K. Joulain, J. Drevillon, G. Domingues, tailoring the local density of states of nonradiative field at the surface of nanolayered materials, Applied Physics Letters 94 (2009) 153117.

[39] P. Ben-Abdallah, K. Joulain, J. Drevillon, G. Domingues, Near-field heat transfer mediated by surface wave hybridization between two films, Journal of Applied Physics 106 (2009) 044306.

[40] M. Francoeur, M.P. Mengüç, R. Vaillon, Near-field radiative heat transfer via surface phonon polaritons coupling in thin films, Applied Physics Letters 93 (2008) 043109.

[41] M. Francoeur, M.P. Mengüç, R. Vaillon, Local density of electromagnetic states within a nanometric gap formed between two thin films supporting surface phonon polaritons, Journal of Applied Physics 107 (2010) 034313.

[42] M. Francoeur, M.P. Mengüç, R. Vaillon, Spectral tuning of near-field radiative heat flux between two thin silicon carbide films, Journal of Physics D: Applied Physics 43 (2010) 075501.

[43] C.J. Fu, W.C. Tan, Near-field radiative heat transfer between two plane surfaces with one having a dielectric coating, Journal of Quantitative Spectroscopy & Radiative Transfer 110 (2009) 1027–1036.

[44] A. Narayanaswamy, G. Chen, Direct computation of thermal emission from nanostructures, Annual Review of Heat Transfer 14 (2005) 169–195.

[45] M. Francoeur, M.P. Mengüç, R. Vaillon, Solution of near-field thermal radiation in one-dimensional layered media using dyadic Green's functions and the scattering matrix method, Journal of Quantitative Spectroscopy & Radiative Transfer 110 (2009) 2002–2018.

[46] K. Joulain, R. Carminati, J.-P. Mulet, J.-J. Greffet, Definition and measurement of the local density of electromagnetic states close to an interface, Physical Review B 68 (2003) 245405.

[47] S. Basu, B.J. Lee, Z.M. Zhang, Near-field radiation calculated with an improved dielectric function model for doped silicon, Journal of Heat Transfer 132 (2010) 023302.

[48] M. Francoeur, M.P. Mengüç, R. Vaillon, Control of near-field radiative heat transfer via surface phonon-polariton coupling in thin films, Applied Physics A: Materials Science & Processing 103 (3) (2011) 547–550.

[49] S.-A. Biehs, Thermal heat radiation, near-field energy density and near-field radiative heat transfer of coated materials, European Physical Journal B 58 (2007) 423–431.

[50] S.M. Rytov, Y.A. Kravtsov, V.I. Tatarskii, Principles of Statistical Radiophysics 3: Elements of Random Fields, Springer, Verlag, Berlin, 1989.
[51] J.D. Jackson, Classical Electrodynamics, John Wiley and Sons, New York, 1999.
[52] T.J. Cui, J.A. Kong, Time-domain electromagnetic energy in a frequency-dispersive left-handed medium, Physical Review B 70 (2004) 205106.
[53] L. Mandel, E. Wolf, Optical Coherence and Quantum Optics, Cambridge University Press, New York, 1995.
[54] L. Novotny, B. Hecht, Principles of Nano-optics, Cambridge University Press, New York, 2006.
[55] J. Skaar, On resolving the refractive index and the wave vector, Optics Letters 31 (2006) 3372–3374.
[56] Z.M. Zhang, Nano/Microscale Heat Transfer, McGraw-Hill, New York, 2007.
[57] J.B. Pendry, A.J. Holden, W.J. Stewart, I. Youngs, Extremely low frequency plasmons in metallic mesostructures, Physical Review Letters 76 (1996) 4773–4776.
[58] J.B. Pendry, A.J. Holden, D.J. Robbins, W.J. Stewart, Magnetism from conductors an enhanced nonlinear phenomena, IEEE Transactions on Microwave Theory and Techniques 47 (1999) 2075–2084.
[59] M.S. Wheeler, A scattering-based approach to the design, analysis, and experimental verification of magnetic metamaterials made from dielectrics, Ph.D. Thesis, University of Toronto, 2010.
[60] C.F. Bohren, D.R. Huffman, Absorption and Scattering of Light by Small Particles, Wiley, New York, 2004.
[61] M.S. Wheeler, J.S. Aitchison, J.I.L. Chen, G.A. Ozin, M. Mojahedi, Infrared magnetic response in a random silicon carbide micropowder, Physical Review B 79 (2009) 073103.
[62] M.S. Wheeler, J.S. Aitchison, M. Mojahedi, Three-dimensional array of dielectric spheres with an isotropic negative permeability at infrared frequencies, Physical Review B 72 (2005) 193103.
[63] K. Joulain, J.-P. Mulet, F. Marquier, R. Carminati, J.-J. Greffet, Surface electromagnetic waves thermally excited: radiative heat transfer, coherence properties and Casimir forces revisited in the near field, Surface Science Reports 57 (2005) 59–112.
[64] S. Basu, M. Francoeur, Maximum near-field radiative heat transfer between thin films, Applied Physics Letters 98 (2011) 243120.

CHAPTER 3

TUNING NEAR-FIELD THERMAL RADIATIVE PROPERTIES BY QUANTIFYING SENSITIVITY OF MIE RESONANCE-BASED METAMATERIAL DESIGN PARAMETERS

Journal of Quantitative Spectroscopy and Radiative Transfer (2013) **129**, 277–286.

Journal of Quantitative Spectroscopy & Radiative Transfer 129 (2013) 277–286

Contents lists available at ScienceDirect

Journal of Quantitative Spectroscopy & Radiative Transfer

journal homepage: www.elsevier.com/locate/jqsrt

Tuning near-field thermal radiative properties by quantifying sensitivity of Mie resonance-based metamaterial design parameters

Spencer J. Petersen [a], Soumyadipta Basu [b], Bart Raeymaekers [c], Mathieu Francoeur [a,*]

[a] Radiative Energy Transfer Lab, Department of Mechanical Engineering, University of Utah, Salt Lake City, UT 84112, USA
[b] Assembly Technology Development, Intel Corporation, Chandler, AZ 85226, USA
[c] Nano-Tribology and Precision Engineering Laboratory, Department of Mechanical Engineering, University of Utah, Salt Lake City, UT 84112, USA

ARTICLE INFO

Article history:
Received 22 December 2012
Received in revised form
13 May 2013
Accepted 29 June 2013
Available online 9 July 2013

Keywords:
Near-field radiative transfer
Mie resonance-based metamaterials
Local density of electromagnetic states

ABSTRACT

The possibility of engineering near-field thermal radiative properties is investigated by adjusting design parameters of Mie resonance-based metamaterials. The sensitivities of surface polariton resonance frequencies, in both transverse magnetic and transverse electric polarizations, to parameters such as host medium relative permittivity and particle size and spacing (volume filling fraction) is determined. The sensitivity analysis is performed using a design of experiments method in combination with Mie resonance calculations and Clausius–Mossotti mixing relations. Particle size has the greatest effect on the resonance frequencies, while the volume filling fraction has the least. Based on the results from the sensitivity analysis, three metamaterials are selected for further analysis. The physics of these metamaterials is explored by calculating local density of electromagnetic states and surface polariton dispersion relation. As predicted by the sensitivity analysis, the local density of electromagnetic states and dispersion relation calculations show that Mie resonance-based metamaterials can be tuned to exhibit surface polariton resonance in the near-infrared spectrum. Energy density calculations show that surface polariton resonance in the near-infrared can be activated at temperatures as low as 800 K. Finally, a pathway to implementation of these metamaterials into macroscale engineering applications is proposed. Such metamaterials, with near-infrared surface polariton resonance, will significantly impact the development of nanoscale-gap thermophotovoltaic power generators for recycling waste heat into electricity.

1. Introduction

Due to increasing worldwide energy demand, great interest has been placed in the development of low-cost high-efficiency renewable energy generation technologies [1]. Thermophotovoltaic (TPV) power generation is one such technology that converts radiative energy into electric power via a TPV cell [2]. This is appealing as a renewable energy method because wasted heat can be recycled into usable power. When the separation between the radiator and the TPV cell is smaller than Wien's wavelength, radiation heat transfer enters the near-field regime [3–11]. In the near field, blackbody predictions can be exceeded by orders of magnitude as a result of evanescent wave tunneling. Also, resonant electromagnetic surface waves referred to as surface polaritons (SPs) can produce quasimonochromatic radiative transfer [12,13]. In addition to the inherent benefits of a TPV device

* Corresponding author. Tel.: +1 8015815721.
E-mail address: mfrancoeur@mech.utah.edu (M. Francoeur).

0022-4073/$ - see front matter © 2013 Elsevier Ltd. All rights reserved.
http://dx.doi.org/10.1016/j.jqsrt.2013.06.028

(quiet, low maintenance, nonpollutant, etc.), a nanoscale-gap TPV system capitalizing on the enhanced quasimonochromatic radiant energy exchange that occurs in the near field can significantly increase electrical energy generation. A number of theoretical [14–19] and experimental [20–22] analyses have been performed showing this enhanced energy exchange. A recent study has shown, however, that limitations are inherent with currently proposed nanoscale-gap TPV systems [23]. TPV cells have absorption bandgaps around 0.7 eV (1.8 μm), which is in the near-infrared (NIR) spectrum. Radiation at frequencies below the bandgap of a given cell is not sufficient to generate electron–hole pairs and results in thermal losses via absorption by the lattice and the free carriers. Similarly, excess radiative energy, greater than the bandgap, is also lost to heat by thermalization [23]. The resultant heating of the cell due to these aforementioned mechanisms, combined with heat dissipation via recombination of electron–hole pairs, induce a significant decrease in nanoscale-gap TPV power output and efficiency [23]. Therefore, it is imperative that a monochromatic radiation source in the NIR be found in order to develop viable, highly efficient nanoscale-gap TPV devices.

Biehs et al. [24], Joulain and Henkel [25], Ben-Abdallah et al. [26,27], Francoeur et al. [28–30], and Fu and Tan [31] have explored the possibility of tuning the frequency of SP driven monochromatic emission. They analyzed the near-field radiative exchange between various combinations of multilayered media, showing that, by varying layer thicknesses and compositions, near-field radiative emission can be spectrally tuned. Rodríguez et al. [32] analyzed the tunability of near-field emission via photonic crystals with various surface geometry patterns. Ilic et al. [33] showed that heat exchange by SPs can be tuned by varying manufacturing parameters of graphene. None of the materials studied in these works, however, demonstrated monochromatic NIR emission. West et al. [34] showed that conductive metal oxides are the only known material to sustain SP resonance in the NIR. However, their electromagnetic response depends heavily on the fabrication process. In summary, NIR resonance is rarely attained with naturally occurring materials.

Exotic properties that are not found in natural materials such as negative refractive index are attainable in electromagnetic metamaterials [35,36]. Metamaterials are artificial media consisting of subwavelength, customizable units, or "meta-atoms," that manipulate incoming electromagnetic fields. Research applications that are significantly affected by the study of metamaterials include, but are not limited to, superlenses [36,37] and optical cloaking [36,38]. Customizing the electromagnetic properties of metamaterials makes possible the design of near-field thermal radiative properties, such as media exhibiting resonance in the NIR.

Joulain et al. [39] analyzed near-field radiative heat transfer between identical metamaterials consisting of arrays of metallic wires and split ring resonators. Similar studies were performed by Zheng and Xuan [40,41]. Basu and Francoeur [42] explored the penetration depth of near-field heat transfer when exchanged between two semi-infinite bulks of split ring resonator-wire metamaterial. All three groups showed that radiative heat exchange was dominated by SPs in both transverse magnetic (TM) and transverse electric (TE) polarizations. This additional channel through which radiative energy transfer occurs (the TE-polarized SP) is a direct result of macroscale magnetic responses manifest in these metamaterials, which consist of microscopically nonmagnetic materials. No mention was made of tuning electromagnetic properties in any of these studies.

As an alternative to metal-based metamaterials, Mie resonance-based metamaterials are made up of particles within a host medium that manipulate incoming electromagnetic fields by scattering. Zhao et al. [43] performed theoretical analyses on metamaterials consisting of dielectric cubes made of a mixture of a ceramic material ($Ba_{0.5}Sr_{0.5}TiO_3$) and magnesium oxide in a Teflon host. Qiu and Gao [44] predicted radiative properties of metamaterials consisting of metallic-coated and uncoated dielectric nanospheres. The meta-atoms studied by both of these groups were arranged in ordered lattices. Wheeler et al. [45] showed experimentally that radiative properties can be customized via Mie resonance-based metamaterials with a random arrangement of dielectric particles. Since the meta-atoms are nothing more than particles and a host medium, the macroscopic electromagnetic properties of these metamaterials are isotropic. Additionally, the fabrication of Mie resonance-based metamaterials is potentially simpler than for metal-based metamaterials, as discussed at the end of this article.

Francoeur et al. [46] provided the first study in tuning near-field thermal properties of Mie resonance-based metamaterials where they considered silicon carbide nanoparticles within a potassium bromide host medium. Petersen et al. [47] performed local density of electromagnetic states (LDOS) calculations for the same metamaterial. Again, energy exchange was dominated by SPs in both TM and TE polarizations, showing that macroscale magnetic properties were manifest in these Mie resonance-based metamaterials. Recent studies have discussed the importance of high-permittivity, low-loss dielectric materials as candidates for metamaterial components with resonance in the infrared (IR) [45,48–55]. García-Etxarri et al. [56] addressed the possibility of employing silicon (Si) particles. In spite of the moderate permittivity of Si (~3.5) in the NIR, they were able to show that it is sufficient to induce resonances via a metamaterial made up of spherical Si particles with a radius $r_s = 200$ nm.

The objective of this work is to demonstrate the tunability of near-field thermal emission by Mie resonance-based metamaterials in the NIR bandwidth while showing the sensitivity of emission to adjustable metamaterial parameters, namely, particle diameter, host medium permittivity, and particle volume filling fraction. The metamaterials analyzed are made up of Si nanospheres. A design of experiments (DOE) analysis is performed to quantify the effects of varying each parameter on the SP resonance frequencies ω_r of the metamaterials. The effect of varying these parameters on the radiative properties is thoroughly explored by LDOS, SP dispersion relation, and energy density analyses on selected metamaterials.

A method for the direct calculation of near-field thermal emission by particulate media, e.g., Mie resonance-based metamaterials, is not currently found in the literature. Therefore, quantities such as LDOS and energy density are predicted in this paper using effective medium properties determined with the Clausius–Mossotti (CM) mixing relation. In spite of limiting assumptions in the formulation of the CM relation, the results will provide general trends and significant insights into SP resonance frequencies of metamaterials. Additionally, the results from these predictions will be beneficial when assessing the validity of the effective medium theory when direct calculation of near-field thermal emission by particulate media will be possible.

This paper is structured as follows. Following this introduction, the physical and mathematical description of the problem is given. Then, in the results section, three metamaterials are selected for further exploration based on the DOE analysis. LDOS, dispersion relation, and energy density calculations are performed on these three metamaterials and the results are discussed. In the fourth section, a technique for fabricating the Mie resonance-based metamaterials discussed in this paper is proposed. This technique is based on directed self-assembly using ultrasound waves. Finally, the results of the analyses are summarized in the conclusions.

2. Physical and mathematical description of the problem

Considered herein is an emitting bulk material in vacuum. The bulk is assumed semi-infinite with the bulk-vacuum (medium 1–medium 0) interface being smooth (see Fig. 1). Assuming a cylindrical coordinate system, the interface is azimuthally symmetric (along the θ direction) and infinite along the radial ρ direction. Therefore, results from these analyses depend solely on the z direction. The emitter is in local thermodynamic equilibrium and at temperature T_1. Electromagnetic properties of the emitter are homogeneous, isotropic, and described by spatially local and frequency-dependent relative electric permittivity $\varepsilon_1(=\varepsilon_1^{'}+i\varepsilon_1^{''})$ and relative magnetic permeability $\mu_1(=\mu_1^{'}+i\mu_1^{''})$. For convenience, from this point forward, the term "relative" will be omitted when referring to permittivity and permeability.

The thermal near field generated by the bulk at a distance Δ in vacuum, as shown in Fig. 1, is characterized by the energy density. The spectral energy density for

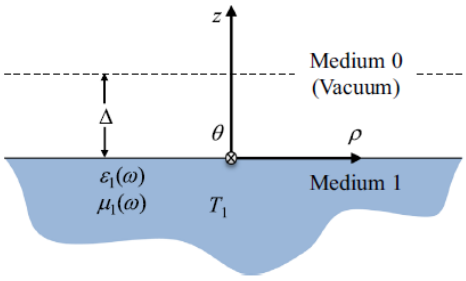

Fig. 1. Problem geometry and configuration.

media with arbitrary permittivity and permeability, derived from fluctuational electrodynamics, is [47]:

$$u_\omega(\Delta,T_1)=\frac{\Theta(\omega,T_1)}{4\pi^2\omega}\left\{k_v^2\int_0^{k_v}\frac{k_\rho dk_\rho}{|k_{z0}|}\left[(1-|r_{01}^{TM}|^2)+(1-|r_{01}^{TE}|^2)\right]\right.$$
$$\left.+2\int_{k_v}^{\infty}\frac{k_\rho^3 dk_\rho}{|k_{z0}|}[\mathrm{Im}(r_{01}^{TM})+\mathrm{Im}(r_{01}^{TE})]e^{-2|k_{z0}|\Delta}\right\} \quad (1)$$

where k_v is the vacuum wavevector, k_ρ and k_z are respectively the parallel and normal components of the wavevector, while r_{01}^{TM} and r_{01}^{TE} are the medium 0–1 interface Fresnel reflection coefficients in TM and TE polarization, respectively. The spectral energy density can also be written as the product of the spectral LDOS $N_\omega(\Delta)$ and the mean energy of a Planck oscillator in thermal equilibrium $\Theta(\omega,T_1)$. Throughout these analyses, LDOS contributions from the emitting medium only are considered. LDOS contributions from free space and those reflected by the interface are intentionally omitted since the principal purpose of this work is to evaluate harvestable energy from the bulk. Just as the LDOS provides the possible energy that may be harvested from an emitting surface, the energy density quantifies the thermally activated energy for a specific temperature T_1 [4].

The emitting bulk is a Mie resonance-based metamaterial, defined by a number of parameters such as host permittivity and particle permittivity, size, size distribution, shape, orientation, arrangement, and spacing. The effective permittivity and permeability of the bulk are calculated using the scattering-corrected CM relations [57]:

$$\frac{\varepsilon_1}{\varepsilon_h}=1+N\left[\frac{k_h^3}{i6\pi}\left(\frac{1}{a_1}-1\right)-\frac{N}{3}\right]^{-1}, \quad (2a)$$

$$\frac{\mu_1}{\mu_h}=1+N\left[\frac{k_h^3}{i6\pi}\left(\frac{1}{b_1}-1\right)-\frac{N}{3}\right]^{-1} \quad (2b)$$

where ε_h and μ_h are, respectively, the permittivity and permeability of the host medium, $N(=1/a^3)$ is the number of inclusions per unit volume, a is the lattice constant, k_h is the magnitude of the wavevector in the host medium, and a_1 and b_1 are the first order Mie scattering coefficients [58]. Wheeler has shown that, when within the long-wavelength regime, i.e., $\lambda_h \gg a > 2r_s$ with λ_h as the wavelength in the host medium, the permittivity and permeability can be considered isotropic [57]. Note that the CM model is only applicable to meta-atom configurations in which the volume filling fraction is significantly smaller than unity [36]. Effective medium calculations are the foundation of electromagnetic metamaterial studies as they draw from the microscale properties of the constituents to determine a macroscale homogeneous set of effective properties for the composite medium. However, at scales on the order of the meta-atom the effective medium approach loses accuracy, resulting in spatially dependent electromagnetic properties. Although such might be the case for near-field calculations, a full analysis of these spatial effects is beyond the scope of this work and is left to a future effort.

In this work, a number of metamaterial parameters are constrained, leaving three as variables for the sensitivity study. Si is selected as the particle material since it demonstrates moderate NIR permittivity and, thus, the potential for strong resonance in that bandwidth [56]. Note that over a large portion of the NIR spectrum, the complex refractive index of Si is obtained from the experimental work of Basu et al. [13]. At IR frequencies between 0.5×10^{15} and 3.5×10^{15} rad/s (0.5–3.8 μm) for which these data are lacking, properties from Palik [59] are used. Due to the assumptions of the CM model, the general geometric configuration of the meta-atom is fixed as spheres of uniform size arranged in a simple cubic lattice. The spacing, and hence the volume filling fraction, and size of the spheres are not fixed. In summary, host permittivity ε_h, sphere radius, and volume filling fraction F are selected as variable design parameters of a Mie resonance-based metamaterial.

Additionally, dispersion relation analyses are performed to understand the physics of an emitting metamaterial bulk. Petersen et al. [47] detailed the derivation of the SP dispersion relation that accounts for losses in the emitter for both polarization states. The following conditions apply to TM polarized SP dispersion:

1. $n_1' n_1''$ must be close to zero,
2. ε_1'' must be close to zero,
3. the tangential wavevector k_ρ must be defined as

$$k_\rho^2 = k_v^2 \frac{\varepsilon_1'^2 n_0'^2 - \varepsilon_0'^2 (n_1'^2 - n_1''^2)}{\varepsilon_1'^2 - \varepsilon_0'^2}, \tag{3}$$

4. and, for emitting into vacuum,

$$\varepsilon_1' < -1 \text{ and } n_1'^2 - n_1''^2 < 1 \tag{4a}$$

or

$$-1 < \varepsilon_1' < 0 \text{ and } n_1'^2 - n_1''^2 > 1 \tag{4b}$$

where $n_i\,(=n_i'+in_i'=\sqrt{\varepsilon_i\mu_i})$ is the refractive index of medium i and ε_0 $(=1)$ is the vacuum permittivity. Note that the above discussion is equally applicable for TE polarized SPs when ε terms are replaced with μ.

The most significant contribution to near-field energy exchange emerges from the resonance of SPs when $|dk_\rho/d\omega|\to\infty$ where ω is the angular frequency. The denominator of Eq. (3) shows that this occurs when $\varepsilon_1'=-1$ (or when $\mu_1'=-1$ for TE polarization). However, conditions 1 and 2 also state that the losses must be small for SPs to exist and, hence, for resonance to occur.

3. Results

3.1. Design of experiments

The primary intent of this work is to explore the sensitivity of Mie resonance-based metamaterial design parameters on the TM and TE polarized SP resonance frequencies $\omega_{r,TM}$ and $\omega_{r,TE}$, respectively. DOE is often used to determine the effects of input variation on a set of experiments. As discussed in Section 2, the variable inputs for this sensitivity study are sphere radius, host permittivity, and volume filling fraction and the experiments are theoretical calculations of SP resonance frequencies. These calculations are carried out by first using Mie coefficients and the CM mixing equations to predict the effective permittivity and permeability of the metamaterial
(Eqs. (2a) and (2b)). With the effective properties known, the resonance frequencies are determined by locating where, for TM polarization, $\varepsilon_1'=-1$ and $n_1'n_1''$ and ε_1'' are small and, for TE polarization, $\mu_1'=-1$ and $n_1'n_1''$ and μ_1'' are small.

It is important to note that these effective medium calculations are meant to establish only a first order projection of the relationship between the variable inputs and the SP resonance frequencies. Since, as mentioned above, only the first order Mie coefficients for Si spheres are employed in the DOE analysis. Higher order Mie coefficients are required to accurately predict the electromagnetic response of a sphere the size of which is similar to the field wavelength. Hence, the more detailed LDOS analyses, described in Section 3.2, include a thorough review of the higher order Mie coefficients to maximize the accuracy of the results.

Since a DOE analysis includes calculating the variation of an output due to the perturbation of its inputs, ranges must be established for each of the input variables. A minimum sphere radius of 141 nm is selected since it is the smallest sphere radius that produces a resonance within the NIR spectral band ($0.75–2.51\times10^{15}$ rad/s or 0.75–2.50 μm). A maximum sphere radius of 500 nm is near the largest size of Si spheres that is easily procured from current nanoparticle suppliers. Larger Si spheres are manufacturable, but at considerable cost and effort. A volume filling fraction range of from 0.1 to 0.4 is chosen to thoroughly explore the limits of the CM mixing equations. The host permittivity ranges from 1 (that of vacuum) to 5.96, which is the maximum that results in a NIR resonance.

The only information extracted from the DOE analysis is the main effects, i.e., the sensitivity of the three metamaterial design parameters on the SP resonances. The main effect of a given design parameter is the average change in predicted resonance frequency for all other design parameter combinations in which the given parameter changes from its minimum to its maximum [60]. For example, the main effect of sphere radius on TM resonance is the average change in TM resonance accompanying a change in sphere radius from 141 (minimum) to 500 nm (maximum) over four separate cases: (i) $\varepsilon_h=1.00$ (minimum) and $F=0.1$ (minimum); (ii) $\varepsilon_h=1.00$ (minimum) and $F=0.4$ (maximum); (iii) $\varepsilon_h=5.96$ (maximum) and $F=0.1$ (minimum); (iv) $\varepsilon_h=5.96$ (maximum) and $F=0.4$ (maximum). The 2^3 factorial analysis is a form of DOE analysis that involves calculating every combination of the maxima and minima of three variable design parameters, making the total number of resonance predictions eight $(=2^3)$. This combination of predictions provides sufficient data to successfully evaluate the main effects as defined above.

For each of the three metamaterial parameters, main effects for both the TM and TE SP resonances are calculated. Table 1 shows the results for the TM and TE predictions. The larger the magnitude of the main effect,

the more strongly the design parameter correlates with the resonance frequency. A negative main effects value implies that the resonance, on average, decreases with an increase in the design parameter. As can be seen in Table 1, sphere radius has the most significant effect on the resonance in both polarizations. Conversely, the effect of the filling fraction is two orders of magnitude smaller than that of the sphere radius. For TM polarization, both volume filling fraction and host permittivity show main effects nearly two orders of magnitude smaller than sphere radius. The host medium permittivity has a greater influence on the TM resonance than on the TE.

Since the sensitivity to the volume filling fraction is relatively small, the resonances can be visualized with two-dimensional surface contours as functions of sphere radius and host medium permittivity. Six sphere radii and six host permittivities (making $6^2=36$ resonance calculations for each polarization) equally-spaced within the ranges specified for the DOE analysis are analyzed and charted as the response surfaces. The volume filling fraction for these calculations is held at 0.4. The surfaces are shown in Fig. 2.

As seen in Fig. 2, the TM polarized SP resonance frequency is less affected by variations in the host permittivity than the TE, which is also observed in Table 1. Figure 2 shows that the sphere radius is the most significant contributor to the tunability of resonance frequencies in the metamaterial. At a host relative permittivity of about 4.5, an overlap occurs where both TM and TE resonances appear at the same frequency. This overlap is also relatively independent of sphere radius.

Using the results from the DOE analysis, three metamaterials of interest are selected for further exploration.

Table 1
Results of TM and TE polarized SP resonance frequency DOE analysis.

Design parameter	TM main effect (rad/s)	TE main effect (rad/s)
Sphere radius r_s	-1.39×10^{15}	-1.10×10^{15}
Volume filling fraction F	-2.30×10^{13}	2.16×10^{13}
Host medium permittivity ϵ_h	-6.20×10^{13}	2.79×10^{14}

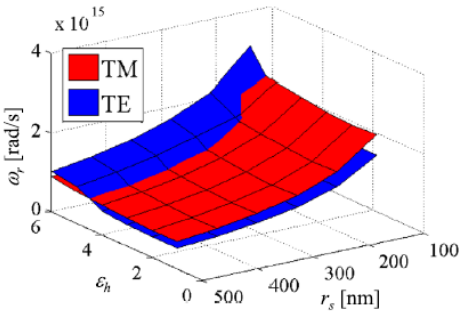

Fig. 2. TM and TE polarized SP resonance frequency as functions of sphere radius and host medium permittivity.

These metamaterials are strategically selected to further prove, with a more in-depth analysis, two of the conclusions from the sensitivity analysis: the volume filling fraction is weakly correlated with the SP resonance frequency and the sphere radius strongly. Metamaterial #1 is made up of 230-nm radius particles within a theoretical nonmagnetic host medium with a permittivity of 1.0; the volume filling fraction is 0.4. The particles in Metamaterial #2 are also 230 nm in radius. The host permittivity is also 1.0 and the volume filling fraction 0.1. Metamaterial #3 consists of 150-nm radius particles in a host of permittivity 1.0 with a volume filling fraction of 0.4. To better understand the physics of what is predicted by the effective property calculations, LDOS and dispersion relation analyses are performed on these three metamaterials.

It is important to note that a large number of metamaterials described by the contours shown in Fig. 2 should not be further analyzed unless a method is employed that accounts for multipole phenomena. These metamaterials result in significant higher order Mie coefficients that render the CM mixing relation insufficient as it is described herein. Among said metamaterials are those aligned with the TE and TM polarized SP resonance frequency overlap at ϵ_h~4.5.

3.2. LDOS calculations

In this section, the aforementioned metamaterials are analyzed further via LDOS profiles. Higher order Si sphere Mie coefficients are thoroughly reviewed for each of the metamaterials to justify the use of only the first order coefficients in Eqs. (2a) and (2b). According to the criteria for the existence of SPs listed in Section 2, dispersion relation analyses are also performed [47]. Results are overlaid with the spectral LDOS per unit tangential wavevector $N_\omega(k_\rho)$. The maximum allowable wavevector for electromagnetic waves in amorphous Si, based on the approximate atomic spacing of 2.7 Å, is 3.7×10^9 rad/m [61,62]. All data presented herein fall below this critical value.

3.2.1. Metamaterial #1

The spectral LDOS per unit tangential wavevector (at $\Delta=50$ nm) and dispersion relation for Metamaterial #1 are shown in Fig. 3(a), while the spectral LDOS (integrated over all tangential wavevectors) are shown in Fig. 3(b). The vacuum light line is compared to the metamaterial light line and the dispersion relation (Eq. (3)) for TE polarized SPs $k_{\rho,TE}$. Note that the emitter and vacuum light lines k_e and k_v, respectively, are included in the analysis to delineate the different wave modes at the interface 1–0. Assume the vacuum light line is smaller than that of the emitter. Waves found to the left of the vacuum light line are propagating on both sides of the interface. Total internal reflection (TIR) occurs between the vacuum and metamaterial light lines, where evanescent waves are found on the vacuum side and reflected propagating waves on the emitter side of the interface. Waves are evanescent on both sides of the interface when located to the right of the emitter light line, where SPs may exist.

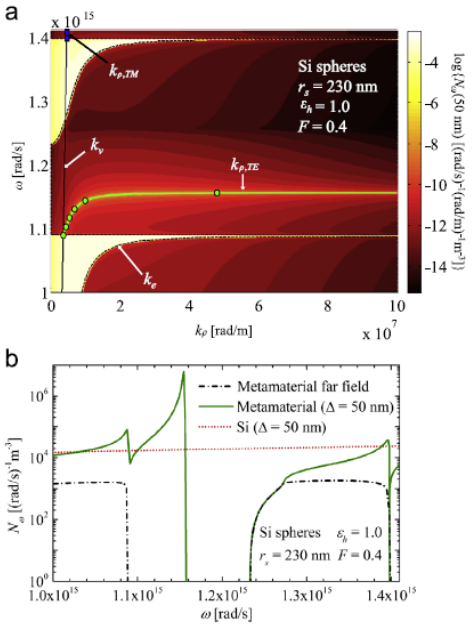

Fig. 3. (a) Metamaterial #1 spectral LDOS per unit tangential wavevector at $\Delta = 50$ nm and SP dispersion relation. (b) Metamaterial #1 spectral LDOS. Near- (green solid) and far-field (black dash–dot) spectra for the metamaterial are compared to the near-field spectra of a Si bulk (red dot). (For interpretation of the references to color in this figure legend, the reader is referred to the web version of this article.)

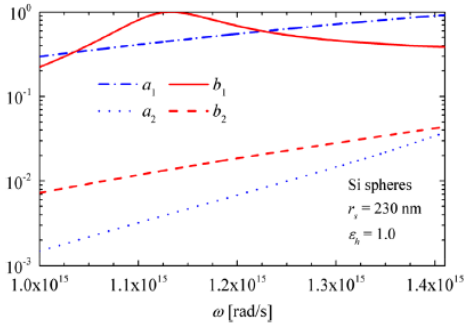

Fig. 4. Metamaterial #1 spectral first and second order Mie coefficients.

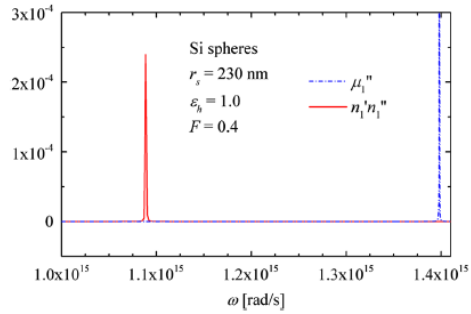

Fig. 5. Metamaterial #1 losses.

Finally, TIR is not possible if the vacuum light line is greater than the emitter light line.

Figure 4 shows the spectral distribution of the first and second order Mie coefficients (a_1, b_1, a_2, and b_2) for a 230-nm Si sphere between 1.00×10^{15} and 1.41×10^{15} rad/s (1.88 and 1.34 μm). The first order Mie coefficient b_1 reaches a maximum at 1.13×10^{15} rad/s, which coincides well with the TE polarized SP resonance frequency found at 1.16×10^{15} rad/s. Over this spectral band, the second order coefficients (a_2 and b_2) are never more than 10% of the first order coefficients, showing that higher order contributions to Eqs. (2a) and (2b) can be neglected.

As seen in Fig. 3(a), horizontal quasiasymptotes in the metamaterial light line at 1.09×10^{15} and 1.40×10^{15} rad/s (1.73 and 1.35 μm) result in significant LDOS due to TIR. The prefix "quasi" is used since the dispersion relation analysis conducted herein accounts for losses and an infinite wavevector is impossible in a lossy medium. A potential NIR resonance frequency is shown at 1.16×10^{15} rad/s (1.62 μm) where the TE polarized SP dispersion relation reaches a quasiasymptote. A close inspection of the losses for this metamaterial (see Fig. 5) shows that the quasiasymptote at 1.16×10^{15} rad/s is indeed SP-driven since μ_1'' and $n_1' n_1''$ are close to zero (2.07×10^{-9} and 5.88×10^{-10}, respectively) at that frequency. Immediately neighboring the TIR region that peaks at 1.40×10^{15} rad/s is a grouping of TM polarized SPs that do not reach a resonance within this spectral band.

Near- (at $\Delta = 50$ nm) and far-field spectral LDOS are compared with near-field LDOS (also at $\Delta = 50$ nm) for a Si bulk in Fig. 3(b). At 50 nm, the metamaterial shows a significant LDOS peak at 1.16×10^{15} rad/s, which agrees perfectly with the resonance frequency calculated by the dispersion relation analysis (see Fig. 3(a)). This peak is accompanied by a smaller local maximum, which aligns with one of the TIR regions in Fig. 3(a). The far-field LDOS distribution is smaller over the entire bandwidth, as expected, since evanescent waves do not contribute to the electromagnetic states at large distances from the emitter. Within the SP bandwidth, the far-field LDOS is negligible. A close observation of the Si distribution relative to that of the metamaterial shows how much near-field energy exchange enhancement is possible due to metamaterial sustained SPs.

3.2.2. *Metamaterial #2*

The SP dispersion relation and spectral LDOS per unit tangential wavevector (at $\Delta = 50$ nm) for Metamaterial #2 are shown in Fig. 6(a). A SP dispersion relation quasiasymptote is seen at 1.14×10^{15} rad/s (1.65 μm) in TE polarization. The losses for this metamaterial are small at this frequency ($\mu_1'' = 1.00 \times 10^{-8}$, $n_1' n_1'' = 6.98 \times 10^{-9}$); therefore,

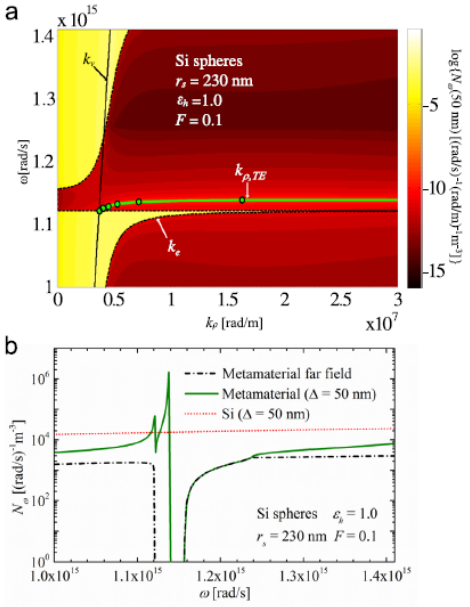

Fig. 6. (a) Metamaterial #2 spectral LDOS per unit tangential wavevector at Δ = 50 nm and SP dispersion relation. (b) Metamaterial #2 spectral LDOS. Near- (green solid) and far-field (black dash–dot) spectra for the metamaterial are compared to the near-field spectra of a Si bulk (red dot). (For interpretation of the references to color in this figure legend, the reader is referred to the web version of this article.)

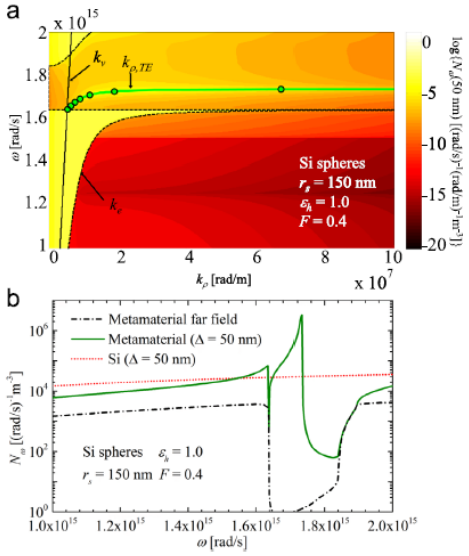

Fig. 7. (a) Metamaterial #3 spectral LDOS per unit tangential wavevector at Δ = 50 nm and SP dispersion relation. (b) Metamaterial #3 spectral LDOS. Near- (green solid) and far-field (black dash–dot) spectra for the metamaterial are compared to the near-field spectra of a Si bulk (red dot). (For interpretation of the references to color in this figure legend, the reader is referred to the web version of this article.)

it is deemed a SP resonance. A horizontal quasiasymptote in the metamaterial light line at 1.12×10^{15} rad/s aligns with significant LDOS due to TIR and is adjacent to the SP resonance. As previously stated, the first order Mie coefficient b_1 for a 230-nm Si sphere is maximum at 1.13×10^{15} rad/s, which is closely aligned with the TE polarized SP resonances of both Metamaterial #1 (1.16×10^{15} rad/s) and #2 (1.14×10^{15} rad/s). The slight discrepancy between Metamaterials #1 and #2 indicates that, although the Mie coefficients drive the predictions, applying the CM mixing relation results in amplification of the resonance frequencies. Also mentioned previously, second order Mie coefficients are no more than 10% of the first order coefficients within this spectral band.

The Metamaterial #2 spectral LDOS for both the near (at Δ = 50 nm) and far field is shown in Fig. 6(b) and compared with that of a Si bulk at 50 nm. A significant peak in the metamaterial near-field LDOS is found at 1.14×10^{15} rad/s, which agrees perfectly with the resonance predictions from the dispersion relation analysis (see Fig. 6(a)). Metamaterial #1 exhibits SP resonance at nearly the same frequency -1.16×10^{15} rad/s (see Fig. 3(b)), further proving that the volume filling fraction has little effect on the SP resonance since the only configurational difference between Metamaterials #1 and #2 is the volume fraction (0.4 and 0.1, respectively). A smaller local maximum accompanies this resonance peak at 1.12×10^{15} rad/s, which aligns with the TIR region seen in Fig. 6(a). Far-field LDOS is smaller than that of the near field and at all SP frequencies is negligible. A comparison between the Si and metamaterial LDOS distributions again shows the possible marked improvements to near-field energy exchange by Mie resonance-based metamaterials

3.2.3. Metamaterial #3

Figure 7(a) charts the spectral LDOS per unit tangential wavevector (at Δ = 50 nm) and SP dispersion relation for Metamaterial #3. A horizontal quasiasymptote is found on the metamaterial light line at 1.64×10^{15} rad/s (1.15 μm), where significant LDOS due to TIR is also found. A SP dispersion relation quasiasymptote found at 1.73×10^{15} rad/s (1.09 μm) corresponds with small losses ($\mu_1''=3.71\times10^{-4}$, $n_1n_1''=6.54\times10^{-4}$), making it a true SP resonance. The first order Mie coefficient b_1 for a 150-nm Si sphere reaches a maximum at 1.70×10^{15} rad/s, which is closely aligned with this TE polarized SP resonance. Higher order 150-nm Si sphere Mie coefficients are small enough, relative to the first order coefficients, that their contribution is negligible over this spectral band. Neither the spectral losses nor higher order Mie coefficients are shown herein.

Spectral LDOS for Metamaterial #3 in the far field and at 50 nm are compared to that of a Si bulk at 50 nm in Fig. 7(b). A significant near-field LDOS peak for the metamaterial is found at 1.73×10^{15} rad/s, which aligns with the dispersion relation analysis resonance prediction (see Fig. 7(a)). A more

significant change in the SP resonance frequency with respect to Metamaterial #1 (1.16×10^{15} rad/s—see Fig. 3(b)) is evident with Metamaterial #3 than with #2 (1.14×10^{15} rad/s—see Fig. 6(b)), showing that the sphere radius has a larger effect on the SP resonance frequency than the volume fraction. A smaller local maximum at 1.64×10^{15} rad/s aligns well with the emitter light line horizontal quasiasymptote in the dispersion relation and is attributed to TIR. The far-field metamaterial LDOS is again negligible over the SP domain. Outside of the SP domain, the metamaterial maintains far-field LDOS markedly smaller than in the near field as expected. The Si bulk shows near-field LDOS similar to but only slightly smaller than the metamaterial over the majority of the bandwidth since, with such a relatively large volume fraction of Si particles, the metamaterial is expected to approach the characteristics of bulk Si. The only exception to this observation is within the SP and TIR regions, where near-field effects dominate the LDOS.

An additional exploration of Metamaterial #3 is conducted by calculating the energy density to examine the temperature dependence on thermal activation of the nearly monochromatic TE polarized SP resonances discussed above. Figure 8 shows the energy density of Metamaterial #3 for $T_1=700$, 800, and 900 K with $\Delta=50$ nm. At 700 K, the peak energy density is at the edge of the spectral band, 1.00×10^{15} rad/s (1.88 μm). The SP resonance at 1.73×10^{15} rad/s is not significantly activated at this temperature. When the temperature is increased to 800 K, the SP resonance barely dominates the density spectra, overcoming the local maximum found at 1.00×10^{15} rad/s. By the time the temperature reaches 900 K, the local peak at 1.00×10^{15} rad/s is completely drowned out by the resonance by almost a factor of three. Without the resonance – that is now shown to be easily tuned using Mie resonance-based metamaterials – thermal activation of 1.73×10^{15} rad/s would not occur until $T_1=2660$ K. A low-temperature NIR resonance such as this will significantly impact nanoscale-gap TPV power generation, as it can allow for electrical power generation by these devices at temperatures 1760 K lower than with commonly employed materials.

A close inspection of the distributions in Figs. 3(a), 6(a), and 7(a) reveals that the immense LDOS values surrounding the SP dispersion relations are barely visually perceivable. In other words, a large, narrow peak of LDOS follows these dispersion curves. In order to generate the corresponding spectral distributions shown in Figs. 3(b), 6(b), 7(b), and 8, integration over all tangential wavevectors in Figs. 3(a), 6(a), and 7(a) is required (see Eq. (1)). Since the LDOS peaks are so narrow near the SP dispersion, a standard discretization scheme, starting with $k_\rho=0$, marching toward $k_\rho\to\infty$, with a small Δk_ρ proves extremely inefficient. Unless Δk_ρ is dramatically small, which significantly effects the computation time, the entire LDOS peak is overlooked. To both mitigate this inaccuracy and decrease computation time, the integrations are performed starting at the LDOS peak maxima (according to the SP dispersion relation (Eq. (3))), marching outwards, in both directions, until convergence.

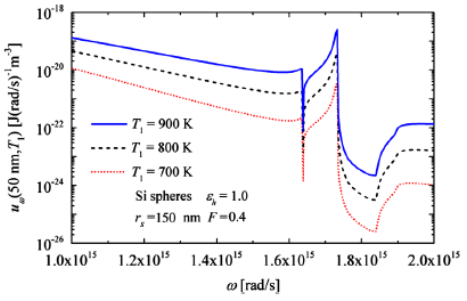

Fig. 8. Metamaterial #3 energy density spectra at $T_1=700$, 800, and 900 K.

4. Fabrication of Mie resonance-based metamaterials

To take advantage of the exotic properties of Mie resonance-based metamaterials in real engineering applications, fabrication of macroscale specimens is necessary. Very few experimental works have been reported in the literature that demonstrate fabrication of dielectric metamaterials. Schuller et al. [53] measured IR extinction spectra of single whisker-shaped silicon carbide particles, and identified three resonant modes. The authors showed that these modes may be employed for designing dielectric-based metamaterials with negative index of refraction. Wheeler et al. [45,57] performed IR measurements on metamaterial samples prepared by mixing silicon carbide and potassium bromide powders pressed into a pellet. The reflectance spectrum, in good agreement with the theoretical predictions, showed that the metamaterial exhibits electric and magnetic resonances in the IR. Ginn et al. [63] measured transmittance and reflectance of metamaterials made of tellurium cubic inclusions coated on a film. The samples were fabricated using lithography techniques. However, none of the fabricated samples described in [45,53,57,63] can be used for real engineering applications because of scale and other restrictions. Electron beam lithography [64] has also been suggested as a fabrication technique for dielectric-based metamaterials. This technique allows covering a macroscale area, but the thickness of the resulting samples is limited. Increasing the thickness requires accurate alignment between different individual layers of material subsequently deposited. Furthermore, it was suggested that fabrication techniques used for metamaterials with metallic inclusions [65] are transferrable to the fabrication of dielectric (Mie resonance-based) metamaterials, such as interferometric lithography [66], and two photon polymerization [64]. A careful review of recent literature shows that no demonstration of macroscale (volume) dielectric metamaterial fabrication exists.

A novel method to manufacture macroscale metamaterial specimens is proposed here. This approach promises a solution for the scalability limitation of existing fabrication methods, and is based on the acoustic radiation force associated with a standing pressure wave. Gor'kov [67] showed that in an inviscid medium, the acoustic radiation force acting on a spherical particle with radius R can be

expressed as the negative gradient of the force potential $F = -\nabla U$ for an arbitrary direction x:

$$F_x = \frac{\pi R^3}{3} p_{0x}^2 k_x \beta_m \phi \sin(2k_x x), \tag{5}$$

where p_{0x} is the peak pressure amplitude, $k_x = 2\pi/\lambda_x$, is the wave number, and λ_x is wavelength in the x-direction. $\beta_m = 1/\rho_m c_m^2$ is the compressibility of the medium, ρ_m and c_m are the density and the sound propagation velocity of the medium. The subscript x refers to the propagation direction of the wave. As a result of the acoustic radiation force, particles are driven towards the nodes ($\Phi > 0$) or the antinodes ($\Phi < 0$) of the standing pressure wave [68]. Φ is the acoustic contrast factor given by

$$\Phi = \frac{5\rho_p - 2\rho_m}{2\rho_p + \rho_m} - \frac{\beta_p}{\beta_m}, \tag{6}$$

where $\beta_p = 1/\rho_p c_p^2$ is the compressibility, ρ_p the density, and c_p the sound propagation velocity of the spherical particle.

Using three orthogonal resonators, piezoelectric crystals in this instance, a 3D standing wave pattern can be established in a square reservoir containing a dispersed solution of particles and a polymer host medium. The 3D standing wave pattern can be designed to match the designs of the metamaterials described in Sections 2 and 3 of this paper. The acoustic radiation force associated with the ultrasound standing wave pattern drives the dispersed particles to the nodes of the interference pattern where they accumulate. This has previously been demonstrated in Ref. [69] and is conceptually illustrated in Fig. 9. When the particles have accumulated at the nodes of the standing wave interference pattern, the polymer is cross-linked to fixate the clusters of particles in place, constituting a macroscale Mie resonance-based metamaterial.

5. Conclusions

The tunability of the electromagnetic properties of Mie resonance-based metamaterials is demonstrated. A DOE analysis is conducted to quantify the sensitivity of adjustable metamaterial design parameters, i.e., particle size and spacing and host permittivity, on TM and TE polarized SP resonances. The DOE analysis, in conjunction with Mie resonance calculations and CM mixing relations, shows that particle size has the greatest effect on resonance frequencies by nearly an order of magnitude. When host permittivity is approximately 4.5, TM and TE polarized SP resonances are found at the same frequency.

Three metamaterials are selected from the results of the sensitivity analysis to further explore their near-field physics. LDOS and SP dispersion relation analyses are performed on these metamaterials to confirm the existence of resonance conditions. NIR resonance frequencies in TE polarization are found with these metamaterials at 1.14×10^{15}, 1.16×10^{15} and 1.73×10^{15} rad/s. The two metamaterials showing nearly identical SP resonances (#1 at 1.16×10^{15} and #2 at 1.14×10^{15} rad/s) differed only by volume filling fraction (0.4 and 0.1, respectively). Metamaterial #3 shows a different resonance frequency at 1.73×10^{15} rad/s and differs from the other two by the sphere radius (150 nm for #3 vs. 230 nm for #1 and #2). These results further prove the conclusions set forth by the DOE analysis that the volume filling fraction has little effect on the SP resonance while the sphere radius has a larger effect.

One of the Mie resonance-based metamaterials studied in this paper demonstrates thermally activated SP resonance at temperatures more than 1700 K lower than in Si. This metamaterial shows a SP resonance in the NIR that is activated at 800 K, dominating the spectral distribution of energy density. Without the SP resonance, a dominant energy density in the NIR does not occur until 2660 K.

The results presented in this paper show that near-field radiative properties of Mie resonance-based metamaterials are tunable by adjusting design parameters such as host permittivity and particle size and spacing. A fabrication method is proposed for implementing these metamaterial designs in macroscale engineering applications. And, with the advent of these metamaterials in the fabrication of nanoscale energy devices, SP resonances can be tuned to within the NIR, making monochromatic energy transfer available at temperatures as low as 800 K.

The validity of the effective medium theory technique employed in these analyses, the CM mixing relation, is questionable in the near field of metamaterials. However, this approach is the only method currently available for predicting near-field thermal emission by particulate media. SP resonance frequency trends presented herein will provide significant insight into near-field capabilities of thermally emitting metamaterials. Additionally, these results will aid in assessing the validity of the effective medium theory when direct calculation of near-field thermal emission by particulate media will be tractable.

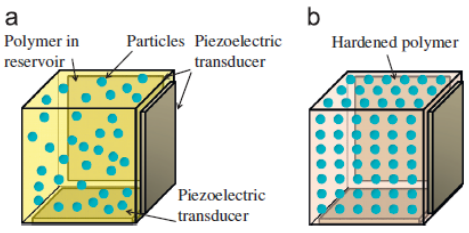

Fig. 9. 3D macroscale metamaterial fabrication technique based on ultrasound standing pressure waves.

Acknowledgments

This work was partially sponsored by the National Science Foundation under Grant no. DMR 11-21252.

References

[1] Baxter J, Bian Z, Chen G, Danielson D, Dresselhaus MS, Fedorov AG, et al. Energy Environ Sci 2009;2:559–88.
[2] Bauer T. Thermophotovoltaics: basic principles and critical aspects of system design. Berlin: Springer; 2011.
[3] Joulain K, Mulet J–P, Marquier F, Carminati R, Greffet J–J. Surf Sci Rep 2005;57:59–112.

[4] Zhang ZM. Nano/microscale heat transfer. New York: McGraw-Hill; 2007.
[5] Hu L, Narayanaswamy A, Chen X, Chen G. Appl Phys Lett 2008;92:133106.
[6] Basu S, Zhang ZM, Fu CJ. Int J Energy Res 2009;33:1203–32.
[7] Rousseau E, Siria A, Jourdan G, Volz S, Comin F, Chevrier J, et al. Nat Photonics 2009;3:514–7.
[8] Shen S, Narayanaswamy A, Chen G. Nano Lett 2009;9:2909–13.
[9] Howell JR, Siegel R, Mengüç P. Thermal radiation heat transfer. 5th ed. Boca Raton: CRC Press; 2011.
[10] Ottens RS, Quetschke V, Wise S, Alemi AA, Lundock R, Mueller G, et al. Phys Rev Lett 2011;107:014301.
[11] Shen S, Mavrokefalos A, Sambegoro P, Chen G. Appl Phys Lett 2012;100:133114.
[12] Mulet J–P, Joulain K, Carminati R, Greffet J–J. Microscale Therm Eng 2002;6:209–22.
[13] Basu S, Lee BJ, Zhang ZM. J Heat Transfer 2010;132:023301.
[14] Whale MD. [Ph.D. dissertation]. Massachusetts Institute of Technology, 1997.
[15] Whale MD, Cravalho EG. IEEE Trans Energy Conver 2002;17:130–42.
[16] Narayanaswamy A, Chen G. Appl Phys Lett 2003;82:3544–6.
[17] Laroche M, Carminati R, Greffet J–J. J Appl Phys 2006;100:063704.
[18] Park K, Basu S, King WP, Zhang ZM. J Quant Spectrosc Radiat Transfer 2008;109:305–16.
[19] Ilic O, Jablan M, Joannopoulos JD, Celanovic I, Soljačić M. Opt Express 2012;20:A366–84.
[20] DiMatteo RS, Greiff P, Finberg SL, Young-Waithe KA, Choy HKH, Masaki MM, et al. Appl Phys Lett 2001;79:1894–6.
[21] DiMatteo RS, Greiff P, Seltzer D, Meulenber G, Brown E, Carlen E, et al. AIP Conf Proc 2004;738:42–51.
[22] Hanamura K, Mori K. AIP Conf Proc 2007;890:291–6.
[23] Francoeur M, Vaillon R, Mengüç MP. IEEE Trans Energy Conver 2011;26:686–98.
[24] Biehs S–A, Reddig D, Holthaus M. Eur Phys J B 2007;55:237–51.
[25] Joulain K, Henkel C. Appl Phys B—Lasers Opt 2008;93:151–8.
[26] Ben-Abdallah P, Joulain K, Drevillon J, Domingues G. Appl Phys Lett 2009;94:153117.
[27] Ben-Abdallah P, Joulain K, Drevillon J, Domingues G. J Appl Phys 2009;106:044306.
[28] Francoeur M, Mengüç MP, Vaillon R. Appl Phys Lett 2008;93:043109.
[29] Francoeur M, Mengüç MP, Vaillon R. J Appl Phys 2010;107:034313.
[30] Francoeur M, Mengüç MP, Vaillon R. J Phys D Appl Phys 2010;43:075501.
[31] Fu CJ, Tan WC. J Quant Spectrosc Radiat Transfer 2009;110:1027–36.
[32] Rodríguez AW, Ilic O, Bermel P, Celanovic I, Joannopoulos JD, Soljačić M, et al. Phys Rev Lett 2011;107:114302.
[33] Ilic O, Jablan M, Joannopoulos JD, Celanovic I, Buljan H, Soljačić M. Phys Rev B 2012;85:155422.
[34] West PR, Ishii S, Naik GV, Emani NK, Shalaev VM, Boltasseva A. Laser Photonics Rev 2010;1–13:795–808.
[35] Veselago VG. Sov Phys—Usp 1968;10:509–14.
[36] Cai W, Shalaev V. Optical metamaterials: fundamentals and applications. New York: Springer; 2010.
[37] Pendry JB. Phys Rev Lett 2000;85:3966–9.
[38] Pendry JB, Schurig D, Smith DR. Science 2006;312:1780–2.
[39] Joulain K, Drevillon J, Ben-Abdallah P. Phys Rev B 2010;81:165119.
[40] Zheng Z, Xuan Y. Int J Heat Mass Transfer 2011;54:1101–10.
[41] Zheng Z, Xuan Y. Chin Sci Bull 2011;56:2312–9.
[42] Basu S, Francoeur M. Appl Phys Lett 2011;99:143107.
[43] Zhao Q, Kang L, Du B, Zhao H-J, Xie Q, Li B, et al. Chin Sci Bull 2008;53:3272–6.
[44] Qiu C–W, Gao L. J Opt Soc Am B 2008;25:1728–37.
[45] Wheeler MS, Aitchison JS, Chen JIL, Ozin GA, Mojahedi M. Phys Rev B 2009;79:073103.
[46] Francoeur M, Basu S, Petersen S. Opt Express 2011;19:18774–88.
[47] Petersen SJ, Basu S, Francoeur M. Photonic Nanostruct 2013. http://dx.doi.org/10.1016/j.photonics.2013.03.002, in press.
[48] Huang KC, Povinelli ML, Joannopoulos JD. Appl Phys Lett 2004;85:543–5.
[49] Wheeler MS, Aitchison JS, Mojahedi M. Phys Rev B 2005;72:193103.
[50] Yannopapas V, Moroz A. J Phys: Condens Matter 2005;17:3717–34.
[51] Jylhä L, Kolmakov I, Maslovski S, Tretyakov S. J Appl Phys 2006;99:043102.
[52] Peng L, Ran L, Chen H, Zhang H, Kong JA, Grzegorczyk TM. Phys Rev Lett 2007;98:157403.
[53] Schuller JA, Zia R, Taubner T, Brongersma ML. Phys Rev Lett 2007;99:107401.
[54] Ahmadi A, Mosallaei H. Phys Rev B 2008;77:045104.
[55] Vynck K, Felbacq D, Centeno E, Dabuz AI, Cassagne D, Guizal B. Phys Rev Lett 2009;102:133901.
[56] García-Etxarri A, Gómez-Medina R, Froufe-Pérez LS, López C, Chantada L, Sheffold F, et al. Opt Express 2011;19:4815–26.
[57] Wheeler MS. [Ph.D. thesis]. University of Toronto, 2010.
[58] Bohren CF, Huffman DR. Absorption and scattering of light by small particles. New York: Wiley; 2004.
[59] Palik ED. Handbook of optical constants of solids. San Diego: Academic Press; 1998.
[60] Box GE, Hunter WG, Hunter JS. Statistics for experimenters. Toronto: John Wiley & Sons; 1978.
[61] Volokitin AI, Persson BNJ. Phys Rev B 2004;69:045417.
[62] Basu S, Zhang ZM. J Appl Phys 2009;105:093535.
[63] Ginn JC, Brener I, Peters DW, Wendt JR, Stevens JO, Hines PF, et al. Phys Rev Lett 2012; 108: 097402.
[64] Formanek F, Takeyasu N, Tanaka T, Chiyoda K, Ishikawa A, Kawata S. Opt Express 2006;14:800–9.
[65] Boltasseva A, Shalaev VM. Proc Soc Photo-Opt Ins 2008;1:1–17.
[66] Zhang S, Fan W, Malloy KJ, Brueck SRJ, Panoiu NC, Osgood RM. J Opt Soc Am B 2006;23:434–8.
[67] Gor'kov LP. Sov Phys Dokl 1962;6:773.
[68] Yosioka K, Kawasima Y. Acustica 1955;5:167–73.
[69] Raeymaekers B, Pantea C, Sinha DN. J Appl Phys 2011;109:014317.

CHAPTER 4

FABRICATION AND CHARACTERIZATION OF THREE-DIMENSIONAL MACROSCALE DIELECTRIC MIE RESONANCE-BASED METAMATERIALS

In pursuit of realizable dielectric Mie resonance-based (DMRB) metamaterials, researchers have proposed and employed numerous methodologies. Wheeler et al. [1] were the first to fabricate a three-dimensional (3D) macroscale DMRB metamaterial. They fabricated their samples by compressing a mixture of silicon carbide and potassium bromide pellets and characterized the diffuse reflectance thereof with a Fourier transform infrared (FTIR) spectrometer. Both electric and magnetic dipole resonances were observed in the diffuse reflectance results (at 0.10–0.12 eV and ~0.10 eV, respectively). Engineering metamaterials manufactured with this process are limited to material combinations with such cohesive and adhesive properties as to ensure the compressed pellet mixture will be structurally resilient.

Ginn et al. [2] and Liu et al. [3] fabricated metamaterials consisting of a single layer of frustum-shaped Mie resonance-based 2-μm tellurium resonators using electron beam lithography. They characterized their metamaterials with hemispherical directional reflectometer measurements, which indicated electric resonances at ~0.13–0.17 eV and magnetic resonances at ~0.11–0.16 eV. The metamaterial characterized by Moitra et al. [4] was a single layer of cylindrical silicon resonators on a silicon/silicon dioxide

substrate, also fabricated by electron beam lithography. The measured spectral reflectance indicated electric resonances between 0.62 and 0.99 eV and magnetic resonances between 0.55 and 0.99 eV. Valentine et al. [5] fabricated an optical cloak comprised of a single layer of 110-nm holes in a silicon slab. The holes were machined using focused ion beam milling. Due to the large cost and time requirements of these fabrication techniques, assembling more than a few layers of these metamaterials will prove difficult, falling short of a 3D DMRB metamaterial, where dimensions in the three principle directions are of the same order of magnitude.

Within the existing literature, researchers have attempted to successfully prove a fabrication concept of a 3D DMRB metamaterial. Existing methodologies include limitations such as restricted material selections or fabrication in only two principal directions. Inasmuch as within the previous three chapters of this dissertation is outlined the successful theoretical application of DMRB metamaterials in nanoscale gap TPV (nano-TPV) devices, it is crucial that this technology be demonstrated in reality. Hence, the purpose of this chapter is to describe and review the results of a proposed fabrication technique for these materials.

The fabrication techniques explored in this effort were incrementally developed and intermingled with periodic experimental results. The development of the fabrication process, each step stemming from the predecessor thereof, is described and discussed herein, along with associated experimental results.

4.1 Experimental Characterization and Theoretical Calculations

Metamaterial samples were characterized by quantifying spectral normal transmission. The general test configuration for measuring transmission is shown in Figure 4.1.

Measured spectral transmission was compared with theoretical spectra to validate the predictive capability of the mixing equations and/or the metamaterial fabrication technique. Predictions were made with Equation (2.10) and a simplified form of the single layer transmittance $\bar{T}_1$ equation [6], averaged over the two polarizations γ (transverse magnetic (TM) and transverse electric (TE)),

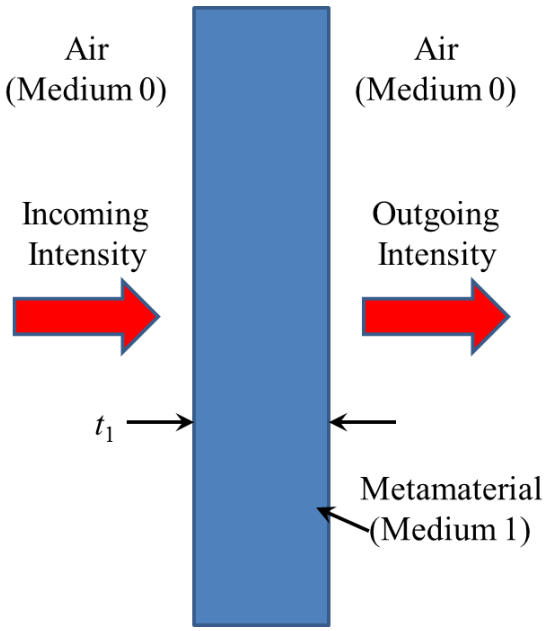

Figure 4.1. General test configuration for measuring metamaterial sample transmission. The metamaterial sample – of thickness t_1 – is surrounded by air. Light intensity is measured prior to entering and again after passing through the sample. The transmission is defined as the ratio of the incoming to outgoing intensities.

$$\overline{T_1} \sim \frac{1}{2}\sum_{\gamma} t_{01}^{\gamma} t_{10}^{\gamma} e^{ik_{z1}t_1} \tag{4.1}$$

where t_{ij}^{γ} is the γ polarized Fresnel transmission coefficient at the *i*-*j* interface. Subscripts 0 and 1 represent the air and the metamaterial, respectively. Hence, k_{z1} is the normal component of the wavevector in the metamaterial and t_1 the thickness of the sample. The Fresnel transmission coefficients are defined as

$$t_{ij}^{TE} = \frac{2k_{zi}}{k_{zi} + k_{zj}} \tag{4.2}$$

and

$$t_{ij}^{TM} = \frac{2\sqrt{\varepsilon_i \varepsilon_j}\, k_{zi}}{\varepsilon_j k_{zi} + \varepsilon_i k_{zj}} \tag{4.3}$$

where k_{zi} is the parallel component of the wavevector and ε_i the relative electric permittivity, both in medium *i*. Both media are assumed nonmagnetic, i.e., the magnetic permeability is equal to 1. The simplified form of the transmittance equation, used for these calculations, is only applicable when the thickness of the specimen is much larger than the vacuum wavelength of interest, which is the case for all specimens described herein. For normal incidence, transmission is equal to the square of the magnitude of the transmittance and is related to the energy in the beam, a real quantity, while transmittance is related to the field, a complex quantity.

4.2 Fabrication

As a first step towards developing a realizable manufacturing process for 3D macroscale DMRB metamaterials, samples were assembled by mixing various

combinations of commercially available dielectric particles and adhesives. One purpose for selecting such a technique is to obtain 3D DMRB metamaterials in which particles are dispersed randomly three-dimensionally within the medium; another is to produce macroscale (~1 cm × 1 cm × 1 cm) metamaterial samples for potential use in real engineering devices. Particles consisted of silicon, silica, germanium, graphite, and alumina, some of which were spherical, while others were randomly shaped, e.g., sandpaper grit, ranging in size from 70 to 1000 nm. Analytical predictions, using Equations (4.1)–(4.3), indicated that such particles would result in a measureable reduction – the size of which depending on the particle volume fraction – to the baseline spectral transmission of epoxy adhesives.

Particles were mixed with multiple two part epoxies, i.e., Smooth-Cast® 300 and 310 liquid plastics and EpoxAcast® 690 epoxy, clear polyester, marine vinyl ester, water clear surfboard, and EPO-TEK® 301-1 epoxy resins, all of which are visually semitransparent. The 3D DMRB metamaterial samples were then analyzed using a UV/VIS/NIR spectrophotometer, a Fourier transform infrared (FTIR) spectrometer, and/or a scanning electron microscope (SEM).

The fabrication process initially employed to fabricate the 3D DMRB metamaterials was to hand mix the particles into a premixed two part epoxy. Each combination was hand mixed until uniformly dispersed, by visual inspection, and then poured into a plastic cup, where the epoxy was allowed to cure (see Figure 4.2a). The particle volume fraction was controlled; the amount of particles added to the uncured resin was selected to result in a visually distinguishable range of volume fractions for the samples. Samples generated with this preliminary technique varied in thickness between

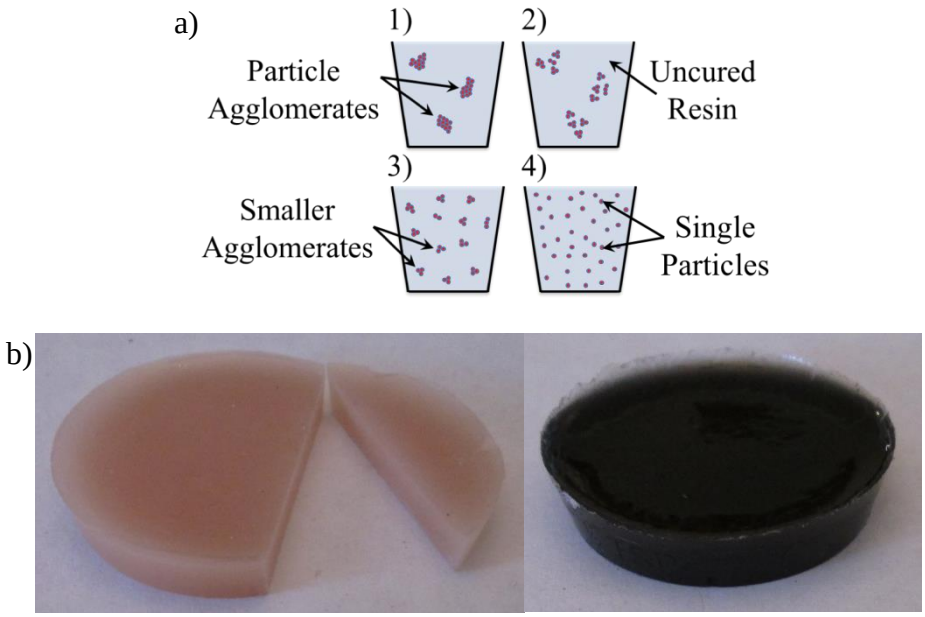

Figure 4.2. a) Initial fabrication procedure for DMRB metamaterials: 1) particles are combined with uncured liquid resin; 2) components are hand mixed; 3) hand mixing is repeated until mixture is uniform; 4) resin is cured. b) Samples fabricated by hand mixing alumina particles in marine vinyl ester resin (left) and graphite particles in EPO-TEK 301-1 epoxy resin (right).

~2.5 and 7.6 mm, some of which are shown in Figure 4.2b.

4.3 Characterization

Samples of similar constituency and geometry were analyzed and compared with an OLIS-modernized Cary 14 (UV/VIS/NIR spectrophotometer) to quantify any change in normal transmission with respect to the corresponding baselines, i.e., empty epoxies (no particles). Any agreement with corresponding predicted transmission values would reflect the uniformity of samples due to the hand mixing process. Since the measurements were taken in air, the first necessary step for using the spectrophotometer was to establish a baseline transmission spectrum. Without a sample in the spectrophotometer chamber, a transmission spectrum was averaged over *n* measurements at each vacuum wavelength. Using this spectrum as a baseline, another transmission spectrum was measured with an

empty chamber, averaged over *n* measurements. If the latter spectrum deviated by no more than 1% from zero, the former was kept as the baseline. Otherwise, *n* was increased and the process repeated until the magnitude of the latter was no greater than 1%. A baseline spectrum was collected for each set of transmission measurements taken after powering the spectrophotometer.

After obtaining an acceptable baseline spectrum, transmission spectra were measured for material samples. A sample was placed in the spectrophotometer and a number of transmission measurements taken at each vacuum wavelength, of which the averages were recorded. A second spectrum was measured with a larger number of measurements at each wavelength. If the change in transmission (between the first and second spectra) was less than 1% over the entire bandwidth, the second spectrum was accepted as the final result. Otherwise, spectra were repeatedly measured, each with an increasing number of measurements, until a 1% convergence was reached, at which point the spectrum corresponding with the largest sample size was considered the final result.

Transmission results for 100-nm silicon particles in an epoxy resin are shown along the ordinate in Figure 4.3 over a near infrared bandwidth of 0.62–1.55 eV on the abscissa, where transmission is defined as the ratio of the measured sample incoming to outgoing light intensities.

The transmission data shown in Figure 4.3 intuitively indicate that increasing the volume fraction generally reduces the transmission. However, significant variation in transmission is apparent for nearly identical samples ($F = 1.61\times10^{-4}$ (#1 and #2)). Therefore, it was presumed that either the surfaces were excessively rough, the particles were insufficiently dispersed, or both. Similar results were obtained for metamaterial

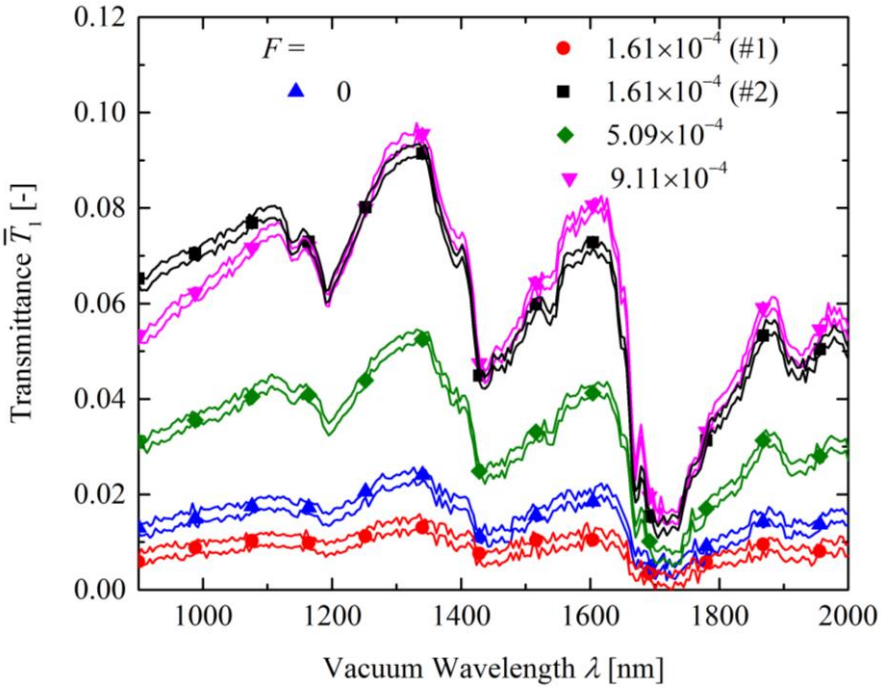

Figure 4.3. Spectrophotometer transmission results for hand mixed metamaterial samples consisting of 100-nm silicon particles and EPO-TEK 301-1 epoxy resin. Volume fraction varies between 0 and 9.1×10^{-4}. Solid lines indicate measurement uncertainty bounds. Sample thicknesses vary between 3.9 and 5.7 mm.

samples consisting of other particle materials and sizes.

In the following set of metamaterial samples, for increased particle dispersion, hand mixing was alternated with a sonication step until the particles were uniformly dispersed within the epoxy resin. To focus on improving the fabrication process, these samples were comprised solely of the 100-nm silicon particles in the EPO-TEK 301-1 epoxy resin. Sonication was performed using a Branson 250 (digital sonifier) at 73% power level. To decrease the surface roughness, samples were cured in plastic molds (see Figure 4.4). Resulting near infrared transmission measurements for 100-nm silicon particles embedded in resin are compared to theoretical predictions in Figure 4.5.

With respect to Figure 4.3, the intuitive trend of decreasing transmission with

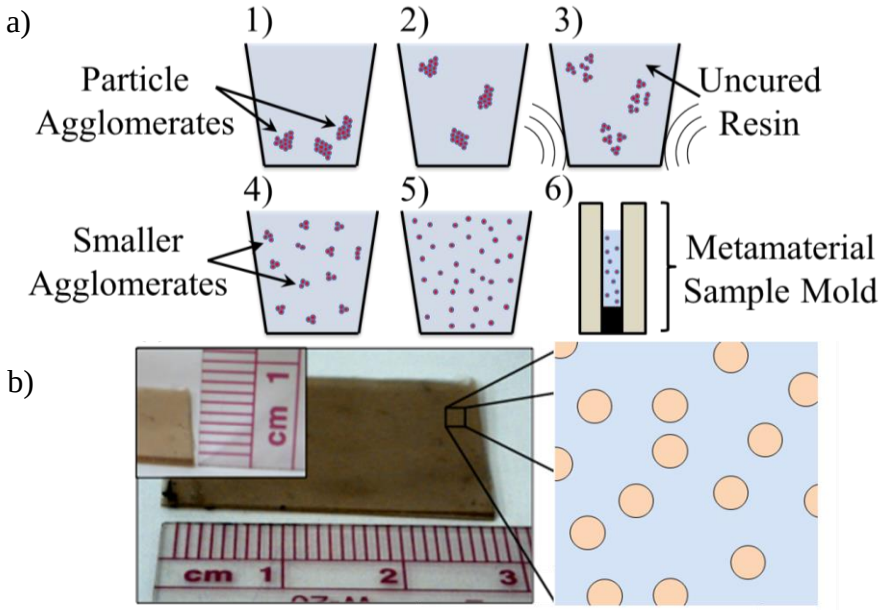

Figure 4.4. a) Final fabrication procedure for DMRB metamaterials: 1) particles are combined with uncured liquid resin; 2) components are hand mixed; 3) mixture is sonicated; 4) and 5) mixing and sonication are repeated until mixture is uniform; 6) mixture is deposited into mold and cured. b) Photograph and schematic of DMRB metamaterial sample: 1) approximate width and thickness (inset) of sample; 2) magnified view of metamaterial showing randomly positioned particles in the resin host medium.

increasing volume fraction is more clear and consistent in Figure 4.5. The improved processing, i.e., sonication and mold fabrication, also indicate better repeatability for transmission through nearly identical samples. However, measured transmission data were contradictory to the predictions. Yet more samples were fabricated with the same process as described above. The resulting near infrared transmission data were measured with a second instrument (Thermo Fisher Scientific Nicolet™ iS™50 (FTIR spectrometer)) to confirm previously seen disagreement with predictions (see Figure 4.5). A comparison of these data with those from the spectrophotometer and the predicted spectrum for the larger volume fraction is shown in Figure 4.6.

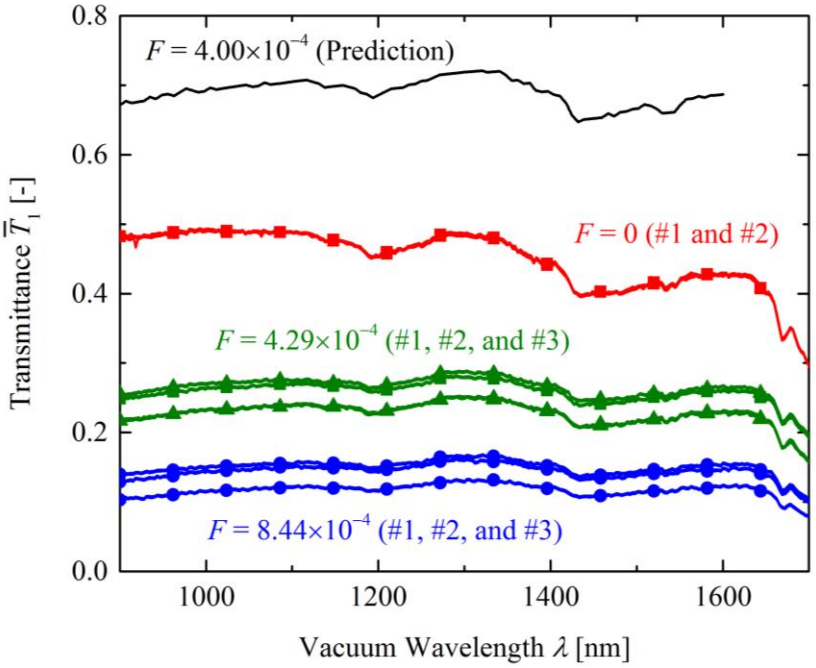

Figure 4.5. Spectrophotometer transmission results for hand mixed/sonicated metamaterial samples consisting of 100-nm silicon particles and EPO-TEK 301-1 epoxy resin. Volume fraction varies between 0 and 8.8×10^{-4}. Solid lines indicate measurement uncertainty bounds (visually undiscernible since uncertainty is approximately 0.001). Sample thicknesses are 0.52 mm. Samples were fabricated in a mold to minimize surface roughness.

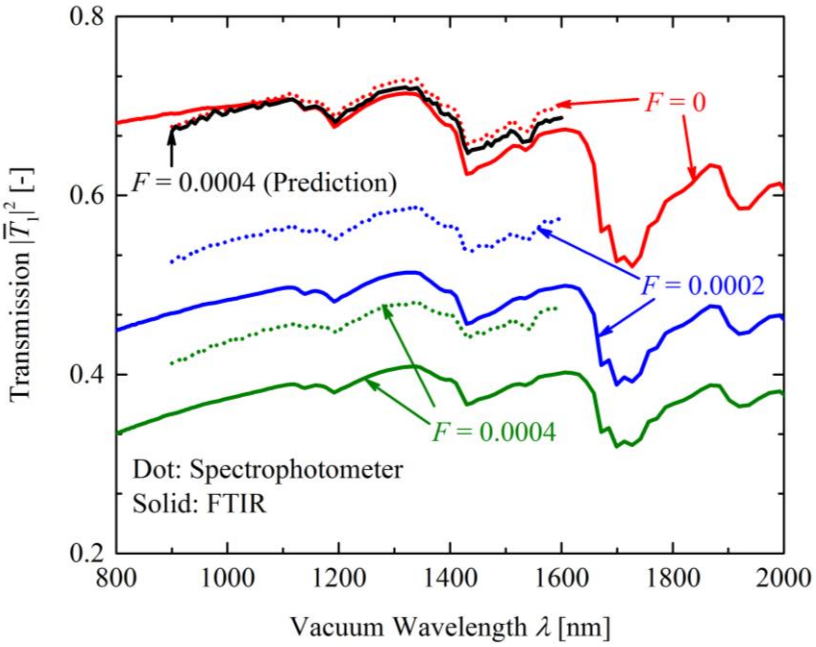

Figure 4.6. Spectrophotometer and FTIR transmission results for hand mixed/sonicated metamaterial samples consisting of 100-nm silicon particles and EPO-TEK 301-1 epoxy resin compared to the prediction. Volume fraction varies between 0 and 4.0×10^{-4}. Sample thicknesses are 0.52 mm. Results from both a spectrophotometer and an FTIR are compared.

As can be seen in Figure 4.6, decreasing transmission with increasing volume fraction trends are observed by both instruments; however, spectra are markedly different between the instruments for the same samples. The effect of volume fraction on transmission is greater in the FTIR. Neither instrument measured transmission data that agree with predictions. It was presumed that the reason for such disagreement between predicted and measured transmission is still insufficient particle dispersion. Nonuniformity in the samples, due to the presumed lack of dispersion, was blamed for the difference between the spectrophotometer and FTIR measurements; i.e., the transmission data were likely measured at different locations on the samples with each instrument. Further efforts were directed toward examining more closely the state of the particles within the cured epoxy resin.

4.4 Particle Dispersion

Reindl [7] showed that silicon particles exhibit substantial dispersion in toluene with fish oil as a surfactant. The following set of metamaterial samples was made following procedures from above, with an added quantity of supermarket fish oil. With the sole intent of observing the configuration of the silicon nanoparticles within the resin matrix, the samples were dissected and then observed in an FEI Quanta 600 FEG (SEM). One of the resulting scanning electron micrographs is shown in Figure 4.7.

Figure 4.7 illustrates that the fish oil surfactant did not sufficiently disperse the silicon particles within the epoxy matrix. Particle agglomerates (such as the one seen in this micrograph) are still maintained at up to ~5 μm in size. These results drove conversations with personnel at the Utah Nanofab facility at the University of Utah, an expert in the field of particle dispersion, Paulo Perez [8]. His recommendation for

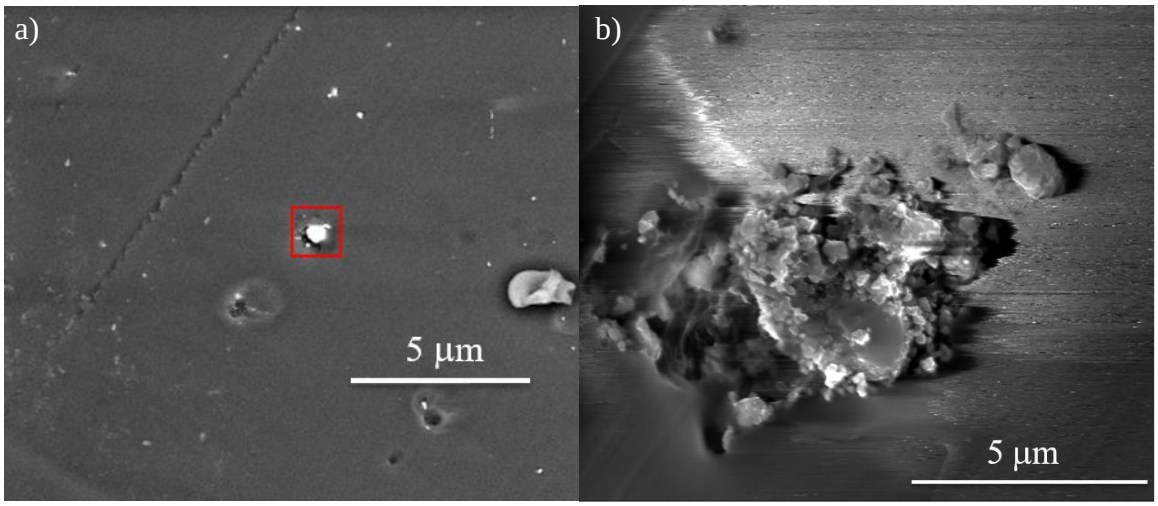

Figure 4.7. Scanning electron micrograph of 100-nm silicon particles in epoxy medium at a) 800X and b) 10,511X magnifications. Red box in a) indicates higher magnification region shown in b). Particles were unsuccessfully dispersed by sonication and hand mixing with the aid of a fish oil surfactant.

increasing the dispersion of the silicon particles in the metamaterial samples was to employ methanol as a surfactant. The silicon particles were added to a solution of toluene and methanol, sonicated, and deposited on glass slides. After evaporation of the solution, scanning electron micrographs were captured of the particles on the glass slides, one of which is shown in Figure 4.8.

The incorporation of methanol as a surfactant did not, with respect to the fish oil surfactant, improve the silicon particle dispersion as can be seen in Figure 4.8. The smaller, ~100-nm particles that occupy the majority of the micrograph are tightly grouped around a larger particle, a condition prevalent along the entire glass substrate. A lack of particle dispersion may have resulted in a significant difference between measured and predicted transmission values for these metamaterials.

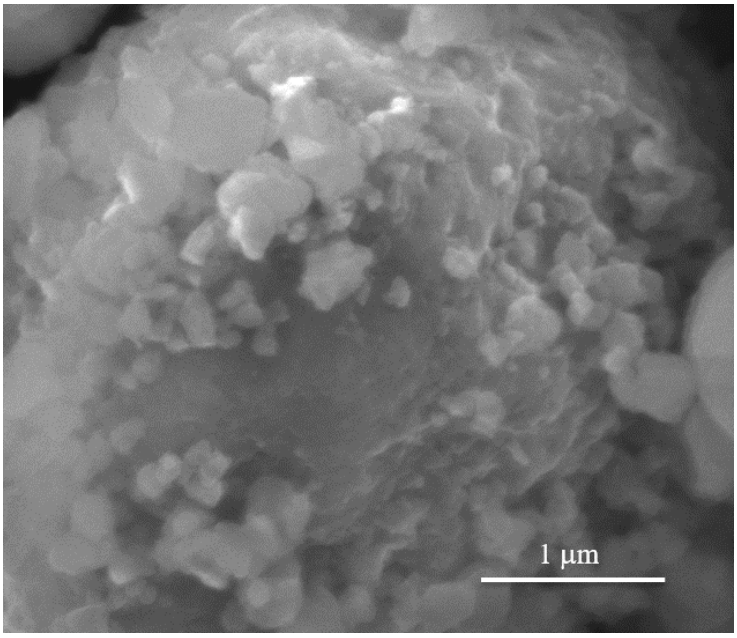

Figure 4.8. Scanning electron micrograph of 100-nm silicon particles on a glass substrate. Particles were unsuccessfully dispersed by sonication in a solution of toluene with a methanol surfactant.

4.5 Conclusion

After significant efforts, it was determined that a viable fabrication process for 3D DMRB metamaterials will require substantial further effort, beyond the funding availability of the author. Metamaterial samples were initially fabricated by hand mixing two part epoxy resins with commercially available nanoparticles. Transmission measurements were inconsistent and markedly different from predictions. To increase the quality of the samples, sonication was added to the manufacturing process for better particle dispersion and the epoxy resin was cured in plastic molds to decrease surface roughness. Transmission measurements became more consistent, but continued to diverge from predictions. Using SEM microscopy, a thorough investigation of surfactants showed that significant effort remains for ensuring adequate particle dispersion. The poor particle dispersion likely prevented measured transmission values from agreeing with those predicted for 3D DMRB metamaterials. Therefore, to further the development of a viable fabrication process for 3D DMRB metamaterials, it is crucial that a deep understanding of dispersion and particle-resin interaction be obtained, an effort beyond the scope of this PhD research project.

4.6 References

[1] M.S. Wheeler, J.S. Aitchison, J.I.L. Chen, G.A. Ozin, and M. Mojahedi, Phys. Rev. B **79** 073103 (2009).

[2] J.C. Ginn, I. Brener, D.W. Peters, J.R. Wendt, J.O. Stevens, P.F. Hines, L.I. Basilio, L.K. Warne, J.F. Ihlefeld, P.G. Clem, and M.B. Sinclair, Phys. Rev. Lett. **108** 097402 (2012).

[3] S. Liu, J.F. Ihlefeld, J. Domínguez, E.F. Gonzales, J.E. Bower, D.B. Burckel, M.B. Sinclair, and I. Brener, Appl. Phys. Lett. **102** 161905 (2013).

[4] P. Moitra, B.A. Slovick, Z.G. Yu, S. Krishnamurthy, and J. Valentine, Appl. Phys.

Lett. **104** 171102 (2014).

[5] J. Valentine, J. Li, T. Zentgraf, G. Bartal, and X. Zhang, Nat. Mater. **8** 568 (2009).

[6] J.I. Pankove, Optical Processes in Semiconductors (Courier Corporation, 2012).

[7] A. Reindl, A. Voronov, P.K. Gorle, M. Rauscher, A. Roosen, and W. Peukert, Colloid. Surface. **320** 183 (2008).

[8] P. Perez (personal communication).

CHAPTER 5

NEAR-FIELD THERMAL EMISSION DUE TO SURFACE POLARITON RESONANCE FROM AN INDIUM TIN OXIDE BULK IN THE NEAR INFRARED

5.1 Introduction

Significant emphasis has been placed on the development of renewable energy source technologies that are both efficient and inexpensive [1]. Since it involves the conversion of waste thermal energy into useful electric current in a thermophotovoltaic (TPV) cell, TPV power generation has become a strong candidate as a viable low cost, highly efficient renewable energy source [2]. A system exchanging thermal radiative energy is said to be in the near-field regime when the separation distance between the radiator and the receiver is less than the dominant emitting wavelength, i.e., Wien's wavelength [3–11]. Blackbody limit can be exceeded by orders of magnitude in this regime due to evanescent wave tunneling. Additionally, in the near-field regime, considerable, nearly or "quasi" monochromatic, energy transfer may result from resonant evanescent waves termed surface polaritons (SPs) [12,13]. Therefore, relative to the classical TPV system, a nanoscale gap TPV (nano-TPV) system can markedly increase electrical energy generation by exploiting these phenomena. Both theoretical [14–21] and experimental [22–24] explorations have shown this enhanced radiative exchange at small scales. However, inherent limitations of the nano-TPV design have been discovered and analyzed [19,21]. Radiative energy lower than the bandgap of a

TPV cell (typically ~0.7 eV (1.8 μm), within the near infrared (NIR), which is typically between 0.5 and 1.5 eV) results in thermal losses by absorption into the lattice and free carriers since it is insufficient to generate electron hole pairs and, hence, electric current. Conversely, radiation energy greater than the bandgap will result in thermalization and nonradiative recombination of electron-hole pairs that result in thermal losses. Such inherent limitations to the TPV concept beg for a NIR quasimonochromatic radiation source to optimize highly efficient nano-TPV devices.

Ilic et al. [25] analyzed the spectral tunability of surface phonon polaritons – a type of SP that is generated by a phonon – induced heat exchange with variable manufacturing parameters of graphene. Biehs et al. [26], Joulain and Henkel [27], Ben-Abdallah et al. [28,29], Francoeur et al. [30–32], and Fu and Tan [33] showed that SP driven monochromatic emission is also tunable by varying combinations of thicknesses and compositions in layered media. Rodríguez et al. [34] explored the prospect of tuning near-field radiative emission with photonic crystals by varying surface geometry. None of these materials exhibited monochromatic emission in the NIR.

Electromagnetic metamaterials are artificial media exhibiting exotic properties not found in naturally occurring materials [35,36]. Mie resonance-based metamaterials consist of subwavelength repeating units called “meta-atoms,” which entail a nearly spherical particle (aspect ratio near unity) surrounded by a host medium. Results from Chapter 3 [37] were the first to demonstrate the tunability of NIR SP resonance in dielectric Mie resonance-based metamaterials, in which a spherical particle in the meta-atom is comprised of silicon. Resonance in the silicon Mie resonance-based metamaterials was predicted to occur within the NIR between 0.75 and 1.14 eV.

However, these materials do not exist in nature and, as described in Chapter 4, the fabrication thereof is not straightforward.

West et al. [38] showed that a promising naturally occurring material manifesting NIR monochromatic emission is indium tin oxide (ITO). However, the electromagnetic properties thereof – plasma frequency ω_p, damping coefficient Γ, and infinite permittivity ε_∞, when employing the Drude model – which determine the spectral location of the surface plasmon polariton (SPP) resonance, are heavily dependent on the fabrication process. Numerous researchers have experimentally demonstrated this dependence, results of which are summarized in Table 5.1.

Other researchers have theoretically shown the variability of ITO electromagnetic properties with fabrication parameters. Using Density Functional Theory, Brewer and Franzen [50], for high temperatures (6300 K), predicted the ITO $\hbar\omega_p$ to be between 0.48 and 5.12 eV by varying the Sn doping level and between 2.66

Table 5.1. Fabrication process dependent electromagnetic properties of ITO.

Author(s)	**Fabrication Method**	$\hbar\omega_p$ **(eV)**	$\hbar\Gamma$ **(eV)**	ε_∞
Fan and Bachner [39]	Sputtered	0.77	0.08	4.5
Ohhata and Yoshida [40] and Yoshida [41]	Sputtered	0.71	0.12	4.0
Ohhata et al. [42]	Sputtered	-	-	2.8–4.0
Hamberg and Granqvist [43]	E-beam Evaporation	0.22–0.90	0.20	-
Brewer and Franzen [44]	Commercially Available	1.82–2.13	0.09–0.16	-
Solieman and Aegerter [45]	Sputtered	1.87	0.07	-
Rhodes et al. [46]	Self Assembled Monolayer	1.08	-	-
Rhodes et al. [47]	Sputtered	1.87	0.07	-
	Spin Coated	1.58	0.18	-
Michelotti et al. [48]	Commercially Available	1.91	0.12	-
Mendelsberg et al. [49]	Commercially Available	1.65–1.74	-	-

and 2.87 eV by varying the lattice parameter of $In_{28}Sn_4O_{48}$. For a baseline comparison, $\hbar\omega_p$ for $In_{28}Sn_4O_{48}$ at 300 K was predicted to be 1.24 eV, indicating the additional potential effect of temperature on the electromagnetic properties of ITO. Later, Franzen [51], using a standard Drude model, calculated $\hbar\omega_p$ for ITO to be 2.19 eV.

The objective of the chapter described herein is to explore the tunability of the electromagnetic properties of ITO that drive near-field radiative energy exchange phenomena. By engineering plasma frequency, damping coefficient, and infinite permittivity, all of which depend on the ITO fabrication process, the spectral location of the SPP resonance can be tuned to occur within the NIR bandwidth. The ITO analyzed falls within the population observed in the literature and, hence, the properties of which are bounded by those listed in Table 5.1. A sensitivity analysis is performed to enumerate the effects of varying these properties on the SPP resonance of ITO. Local density of electromagnetic states (LDOS), SPP dispersion relation, and energy density analyses are performed on selected ITO configurations to more fully explore the sensitivity analysis results.

This chapter is structured as follows. The physical and mathematical configuration of the problem is first described. In the results section, stemming from the sensitivity assessment, two ITO configurations are selected for further analysis. Therein, LDOS, dispersion relation, and energy density calculation results are presented and discussed. Finally, results and discussion are summarized in the conclusions.

5.2 Problem Description

A semiinfinite bulk material, emitting into vacuum, is considered. The vacuum-bulk (Medium 0-Medium 1) interface is smooth (see Figure 5.1). The interface is assumed azimuthally symmetric along the θ direction and infinite along the ρ direction in a cylindrical coordinate system, driving the results to be solely dependent on the z direction. The emitter (Medium 1) is at temperature T_1 and is in thermodynamic equilibrium. A spatially local and angular frequency (ω) dependent relative electric permittivity ε_1 (= $\varepsilon_1' + i\varepsilon_1''$) describes the electromagnetic properties of the nonmagnetic (relative permeability of unity) emitter, which are assumed homogeneous and isotropic. From this point forward, the term "relative" will be omitted when referring to permittivity for convenience. Note that the imaginary component of the permittivity ε_1''

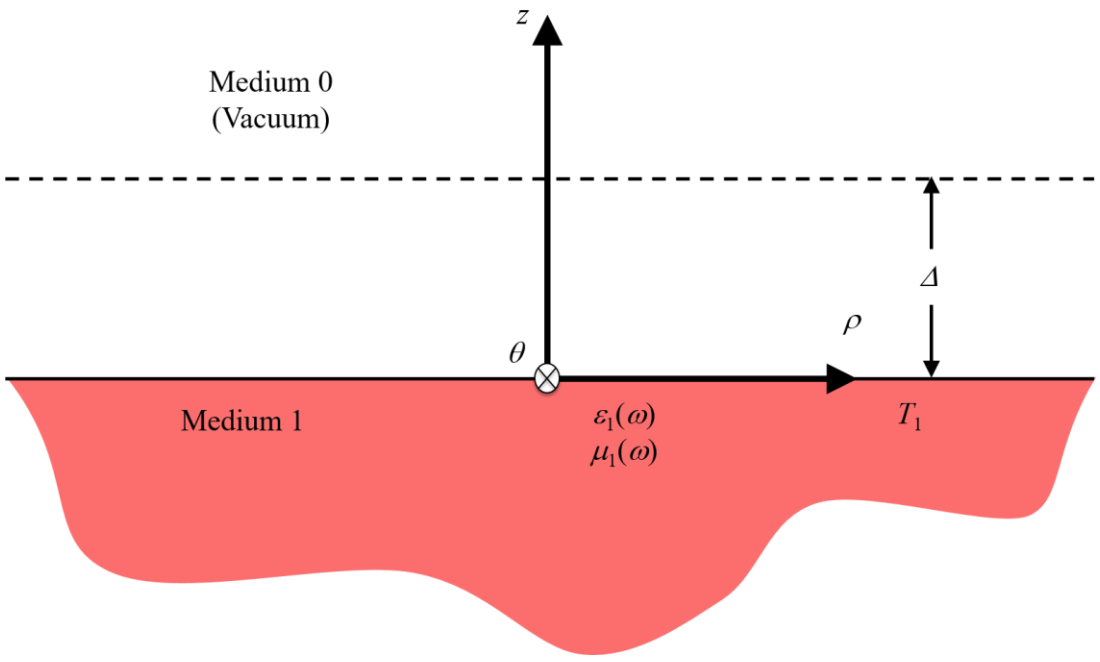

Figure 5.1. Problem geometry and configuration.

represents the electromagnetic losses of the material.

The energy density is a characterization of the thermal near field generated by the emitter at a distance Δ into the vacuum, as shown in Figure 5.1. Using fluctuational electrodynamics, Joulain et al. [52] derived the spectral energy density for nonmagnetic media with arbitrary permittivity:

$$u_\omega(\Delta,T_1)=\frac{\Theta(\omega,T_1)}{4\pi^2\omega}\left\{\begin{array}{l} k_v^2\int_0^{k_v}\frac{k_\rho \mathrm{d}k_\rho}{|k_{z0}|}\left[\left(1-\left|r_{01}^{TM}\right|^2\right)+\left(1-\left|r_{01}^{TE}\right|^2\right)\right] \\ +2\int_{k_v}^{\infty}\frac{k_\rho^3 \mathrm{d}k_\rho}{|k_{z0}|}\left[\mathrm{Im}\left(r_{01}^{TM}\right)+\mathrm{Im}\left(r_{01}^{TE}\right)\right]e^{-2|k_{z0}|\Delta} \end{array}\right\} \tag{5.1}$$

where k_v is the vacuum wavevector, k_ρ is the parallel component of the wavevector, k_{zi} is the perpendicular component of the wavevector in medium i, and r_{01}^{TM} and r_{01}^{TE} are, respectively, the Medium 0-1 interface Fresnel reflection coefficients in transverse magnetic (TM) and transverse electric (TE) polarization. The spectral energy density may also be expressed as: $u_\omega(\Delta,T_1) = N_\omega(\Delta)\Theta(\omega,T_1)$, where $N_\omega(\Delta)$ is the spectral LDOS and $\Theta(\omega,T_1)$ is the mean energy of a Plank oscillator in thermal equilibrium. Contributions to the LDOS from reflections by the 0-1 interface and from free space are neglected in this analysis. LDOS contributions from the emitting medium only are considered since the primary purpose of this work is to quantify the harvestable energy yield from the bulk. Inasmuch as the LDOS characterizes the energy that may be gathered from the emitting bulk, the energy density quantifies the thermally activated energy as a function of the bulk temperature T_1.

The emitter, Medium 1, is ITO and is electromagnetically characterized by the Drude permittivity model described by Rhodes et al. [47]:

$$\varepsilon_1(\omega) = \varepsilon_\infty - \frac{\omega_p^2}{\omega^2 + i\omega\Gamma} \tag{5.2}$$

The plasma frequency is defined as:

$$\omega_p^2 = \frac{n_e e^2}{\mu \varepsilon_v} \tag{5.3}$$

where n_e is the electronic doping level, e the elementary charge (1.60×10^{-19} C), μ the free charge effective mass (defined by $\varepsilon_\infty\mu = 1.4m$ for this analysis [43]) with m being the free electron mass (9.11×10^{-31} kg), and ε_v the absolute permittivity of free space (8.85×10^{-12} A•s•V^{-1}m^{-1}).

Provided the definition of the free charge effective mass from above, the three remaining properties defining a specific ITO configuration, i.e., infinite permittivity ε_∞, damping coefficient Γ, electronic doping level n_e, were selected as variables for the sensitivity analysis described herein. Note that the damping coefficient is directly related to the electromagnetic losses in the material.

As described in Section 5.1, a thorough review of the state of the art of ITO electromagnetic models was conducted to explore credible values for three electromagnetic ITO properties. Reported plasma frequencies range between 0.22 and 2.19 eV (corresponding with, according to Equation (5.3), n_e between 2.0×10^{20} and 9.0×10^{20} cm^{-3}), damping coefficients 0.07 and 0.20 eV, and infinite permittivities 2.8 and 4.0. In this sensitivity analysis, these three electromagnetic properties of ITO are varied over the corresponding ranges.

Dispersion relation analyses are also conducted to understand the physics of a thermally emitting ITO bulk. The derivation of an SP dispersion relation that addresses

losses in the emitting medium was detailed in Chapter 2 [53]. Therein, it is stated that, for SPs to exist in TM polarization, the following must be true:

1. $n_1' n_1''$ must be near zero,
2. ε_1'' must be near zero,
3. the tangential wavevector k_ρ must be defined by

$$k_\rho^2 = k_v^2 \frac{\varepsilon_1'^2 n_0'^2 - \varepsilon_0'^2 \left(n_1'^2 - n_1''^2\right)}{\varepsilon_1'^2 - \varepsilon_0'^2} \tag{5.4}$$

4. and, for emitting into vacuum,

$$\varepsilon_1' < -1 \text{ and } n_1'^2 - n_1''^2 < 1 \tag{5.5a}$$

or

$$-1 < \varepsilon_1' < 0 \text{ and } n_1'^2 - n_1''^2 > 1 \tag{5.5b}$$

where n_i (= $n_i' + i n_i''$ = $\varepsilon_i^{1/2}$) is the refractive index of medium i and ε_0 (= 1) is the vacuum permittivity.

Resonance of SPs occurs when $|dk_\rho/d\omega| \rightarrow \infty$ and is the most significant contributor to near-field energy exchange. According to Equations (5.4) and (5.5), TM polarized SP resonance takes place when $\varepsilon_1' = -1$; however, conditions 1 and 2 must also be satisfied. For a nonmagnetic medium, $\varepsilon_i'' = 2 n_i' n_i''$, therefore condition 2 implies condition 1.

5.3 Results

5.3.1 Sensitivity analysis

Numerous fabrication techniques have resulted in varieties of ITO exhibiting an array of electromagnetic property combinations of infinite permittivity, damping

coefficient, plasma frequency, and electronic doping level, as described in Section 5.1. Since it depends on such properties, the near-field thermal radiative capability of ITO can be engineered by specifying the fabrication technique. The purpose of this effort is to determine the tunability of the ITO SPP resonance. Therefore, an analysis is performed on the sensitivity of the infinite permittivity, plasma frequency, and electronic doping level, which are directly affected by the ITO fabrication technique, on the resonance.

A 2^3 factorial analysis, a type of design of experiments analysis, is performed to determine the predicted spectral location of SPP resonance at each combination of the electromagnetic property maxima and minima listed in Section 5.2. The results are used to determine the main effect of each property on the resonance. The main effect of a given electromagnetic property is, in this case, the average change in resonance over all combinations of the other two property maxima and minima at which the given changes from minimum to maximum [37,54]. For example, the main effect of infinite permittivity on resonance is the average change in resonance accompanying a change in infinite permittivity from 2.8 (minimum) to 4.0 (maximum) over four distinct cases: (i) $\hbar\Gamma$ = 0.07 eV (minimum) and n_e = 2.0×10^{20} cm^{-3} (minimum); (ii) $\hbar\Gamma$ = 0.07 eV (minimum) and n_e = 9.0×10^{20} cm^{-3} (maximum); (iii) $\hbar\Gamma$ = 0.20 eV (maximum) and n_e = 2.0×10^{20} cm^{-3} (minimum); and (iv) $\hbar\Gamma$ = 0.20 eV (maximum) and n_e = 9.0×10^{20} cm^{-3} (maximum).

Main effects for resonance are shown in Table 5.2. The larger the main effect, the more sensitive the spectral location of the SPP resonance is to the corresponding electromagnetic property. Negative main effects indicate that, on average, the resonance

Table 5.2. Results of predicted ITO SPP resonance main effects analysis.

Electromagnetic property	**Main effect (eV)**
Damping coefficient $\hbar\Gamma$	−0.03
Infinite permittivity ε_∞	−0.10
Electronic doping level n_e	0.53

frequency decreases with an increase in the corresponding electromagnetic property. According to Table 5.2, the resonance is most sensitive to the doping level, which exhibits an absolute main effect (0.53 eV) nearly an order of magnitude greater than that of the infinite permittivity (−0.10 eV) and even more so than that of the damping coefficient (−0.03 eV). Due to the significant difference between the two largest main effects, further analyses described herein include the assumption that the doping level is the sole ITO electromagnetic property driving the spectral location of the resonance.

5.3.2 LDOS analysis

The LDOS near an ITO bulk is calculated for two different electronic doping levels (4.5×10^{20} and 1.1×10^{20} cm^{-3}) according to Equations (5.1) and (5.2). These doping levels are selected to explore the effect they have not only on the spectral location of resonance but also on the strength thereof. Dispersion relation analyses are also performed for each doping level, according to the conditions described in Section 5.2 for the existence of SPPs. The SPP dispersion relations are then overlaid with contour plots of wavevector-resolved spectral LDOS $N_\omega(k_\rho)$.

To maximize the possibility of SPP resonance in both ITO types, the damping coefficient is maintained at 0.07 eV, which is the smallest value found to date in the literature [45]. Hamburg states that an infinite permittivity of 3.8 is appropriate for most

configurations of ITO [43].

5.3.2.1 ITO Type 1 ($n_e = 4.5\times10^{20}$ cm^{-3})

The wavevector-resolved spectral LDOS (at Δ = 10 nm) and SPP dispersion relation for ITO Type 1 are displayed in Figure 5.2. The vacuum and ITO light lines are included in the chart to discern between the LDOS resulting from different wave modes at the vacuum-ITO interface. For bandwidths over which the vacuum light line is located to the left of the ITO light line, waves identified to the left of the vacuum light line are propagating on both sides of the interface. Between the two light lines, waves are propagating on the ITO side and evanescent on the vacuum, a phenomenon termed total internal reflection. To the right of the ITO light line, waves are evanescent on both sides of the interface, making it a candidate bandwidth for the existence of SPPs. For the remaining bandwidths, over which the vacuum light line is located to the right of the

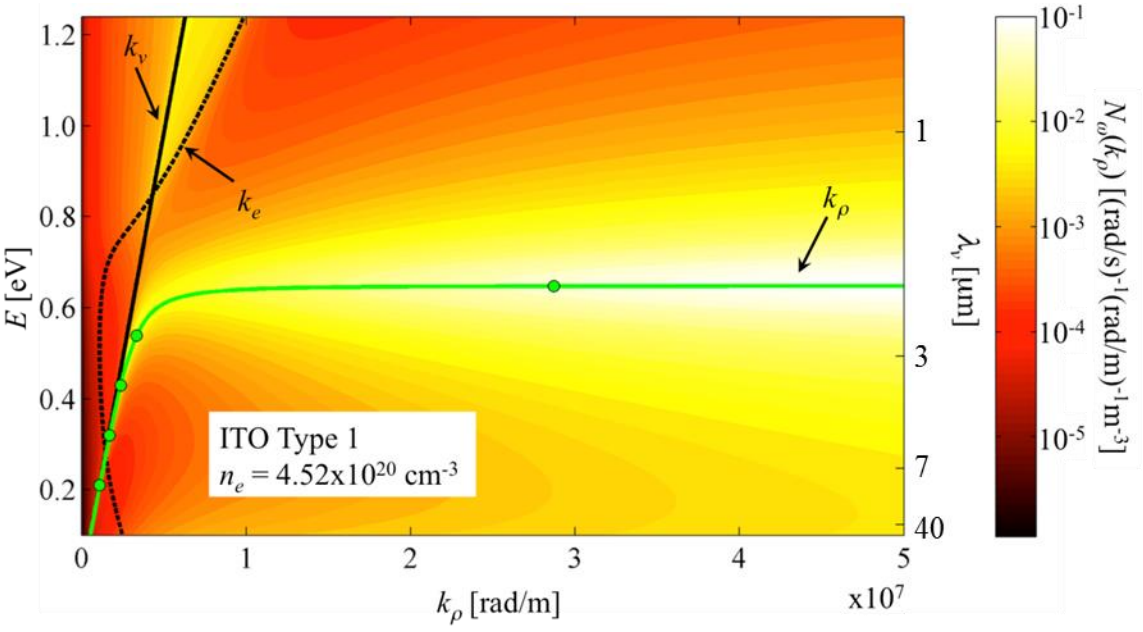

Figure 5.2. ITO Type 1 wavevector resolved spectral LDOS at Δ = 10 nm and SPP dispersion relation.

ITO light line, total internal reflection cannot occur. The spectral LDOS (integrated over all tangential wavevectors) for ITO Type 1 with variable damping coefficients is shown in Figure 5.3.

The SPP dispersion relation analyses described herein account for losses in the emitting medium. Since an infinite wavevector is impossible in a real, i.e., lossy, medium, the apparently horizontal asymptotes displayed in the figures are prefixed with the term "quasi."

A horizontal quasiasymptote is shown in Figure 5.2 at 0.65 eV where a high LDOS is aligned, making it a candidate resonance in the NIR. The imaginary part of the

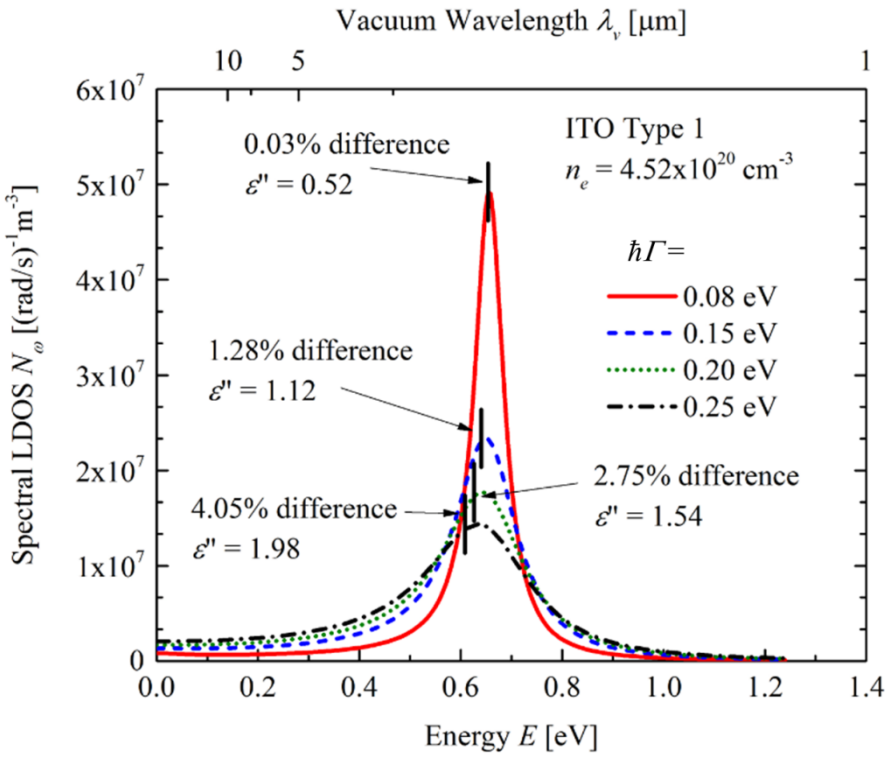

Figure 5.3. ITO Type 1 spectral LDOS (integrated over all tangential wavevectors). The red curve indicates the distribution of ITO Type 1 ($\hbar\Gamma$ = 0.08 eV); the others for increasing values of $\hbar\Gamma$. The scribe marks align with the predicted resonances for each of the respective $\hbar\Gamma$ values. Percent differences between the predicted resonances and LDOS maxima are indicated as well as the corresponding ε'' values.

permittivity for this ITO type is 0.52, which, intuitively, is not “near zero” as required for SPP resonance (see Section 5.2), over the bandwidth where the candidate resonance is located.

As stated in Section 5.2, resonance only occurs when the loss terms are “near zero” – a rather vague statement. Before ascertaining whether the loss terms of a given emitting material are sufficiently small to result in a “significant” resonance, a definition of “significant” must first be established. Each spectral LDOS distribution in Figure 5.3 is scribed at the energy where the candidate resonance is predicted, i.e., where $\varepsilon' = -1$ (Eqs. (5.4) and (5.5)). As the damping coefficient increases, the spectral LDOS maximum both decreases and diverges from the predicted resonance, indicating that the resonance strength, or significance, is directly related to how close the spectral LDOS maximum is to the predicted resonance for ITO. Therefore, a proposed definition of “significant” SPP resonance: the difference between the predicted SPP resonance and the LDOS local maximum must be no greater than 1%. One percent is selected arbitrarily as a small deviation since a justifiable value cannot be selected until devices have been fabricated and tested to indicate how much electromagnetic loss results in insignificant SPP resonance, i.e., values predicted by the dispersion relation analysis to be candidate resonances that do not result in large amounts of energy exchange or LDOS.

Using the above proposed definition for significant SPP resonance, and according to the results shown in Figure 5.3, the maximum allowable ε'' value is between 0.52 and 1.12 for a significant resonance to occur. Since its baseline damping coefficient results in an ε'' of 0.52 and, conversely, a difference between predicted

resonance and LDOS local maximum of 0.03% (<1%), ITO Type 1 is deemed as exhibiting a significant SPP resonance in the NIR. The weak dependence – described in Section 5.2 – of the predicted resonance on damping coefficient is also clear in Figure 5.3.

To further explore the practicality of ITO Type 1 as a radiating material for nano-TPV devices, an examination of the temperature dependence on thermal activation of the SPP resonances is found in Figure 5.4, where the energy density (Eq. (5.1)) at Δ = 10 nm is shown for ITO Type 1 at T_1 = 1200, 1300, and 1400 K. At 1200 K, the SPP resonance at 0.65 eV is not significantly activated and the peak energy density is located at the edge of the displayed spectral band, 0.0 eV. With a temperature increase to 1300 K, the energy density local maximum at 0.65 eV is nearly equivalent to that at 0.0 eV,

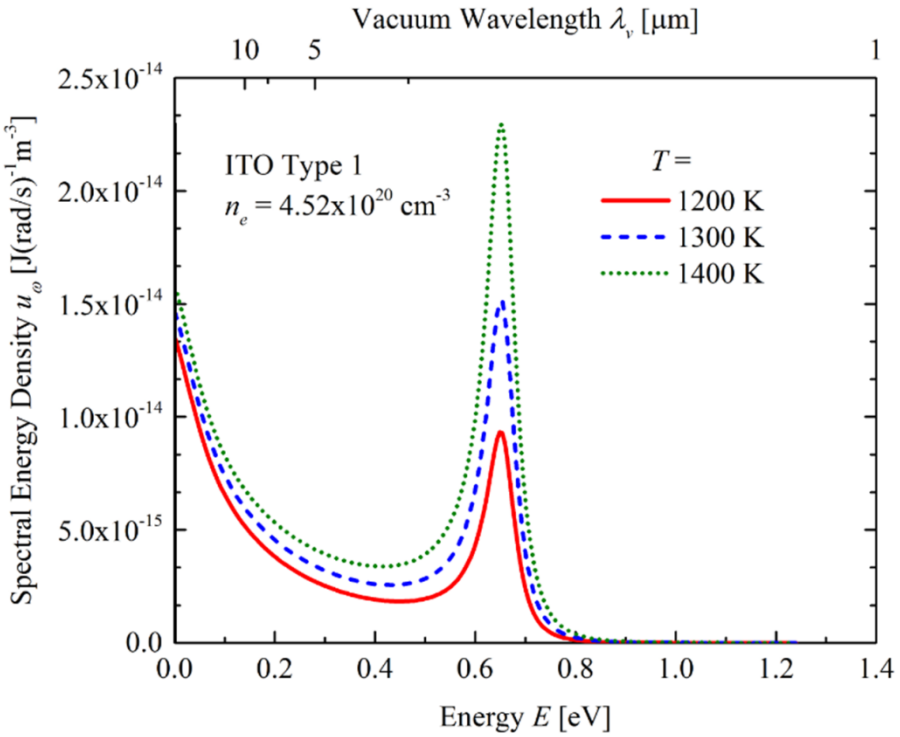

Figure 5.4. Energy density of ITO Type 1 at Δ = 10 nm.

indicating that the SPP resonance is nearly dominating the spectral band. At 1400 K, the SPP resonance completely dominates the spectral band in terms of energy density. In addition, since absorption by the lattice and free carriers below the bandgap of a TPV cell is negligible [19], the energy density peak near 0.0 eV would translate into virtually zero near-field energy flux. Therefore, a low-energy SPP resonance such as this will markedly affect nano-TPV power generation, allowing for relatively low-temperature, nearly monochromatic energy transfer.

5.3.2.2 ITO Type 2 ($n_e = 1.2\times10^{20}$ cm^{-3})

Figure 5.5 depicts the wavevector-resolved spectral LDOS (at Δ = 10 nm) and SPP dispersion relation for ITO Type 2. The SPP dispersion relation exhibits a horizontal quasiasymptote at 0.33 eV, where significant LDOS is also located, giving it

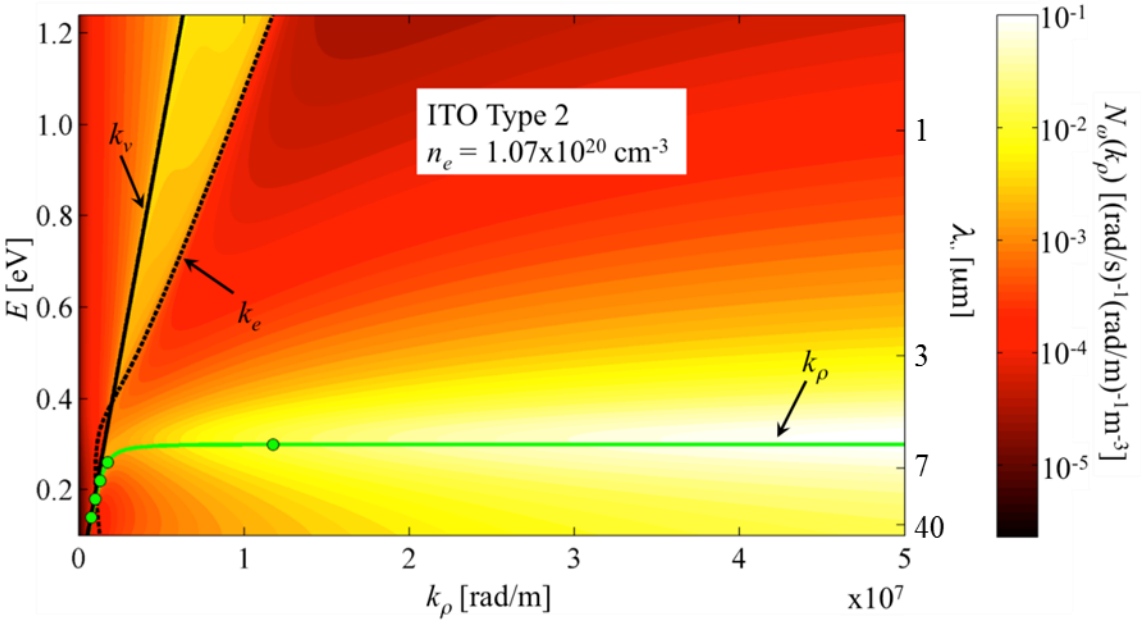

Figure 5.5. ITO Type 2 wavevector resolved spectral LDOS at Δ = 10 nm and SPP dispersion relation.

the potential to be an SPP resonance. The spectral LDOS for ITO Type 2 is shown in Figure 5.6, along with the distribution for an additional loss coefficient, 0.15 eV. The predicted resonance energy (0.33 eV) differs from that of the LDOS local maximum (0.34 eV) by 1.9%. Also indicated in Figure 5.6 is ε'' for both configurations of ITO Type 2. At the spectral location of the candidate resonance, ε'' is 1.70, greater than that of ITO Type 1 and greater than what is suggested as being the maximum allowable ε'' for significant SPP resonance (between 0.52 and 1.12). Therefore, ITO Type 2 is

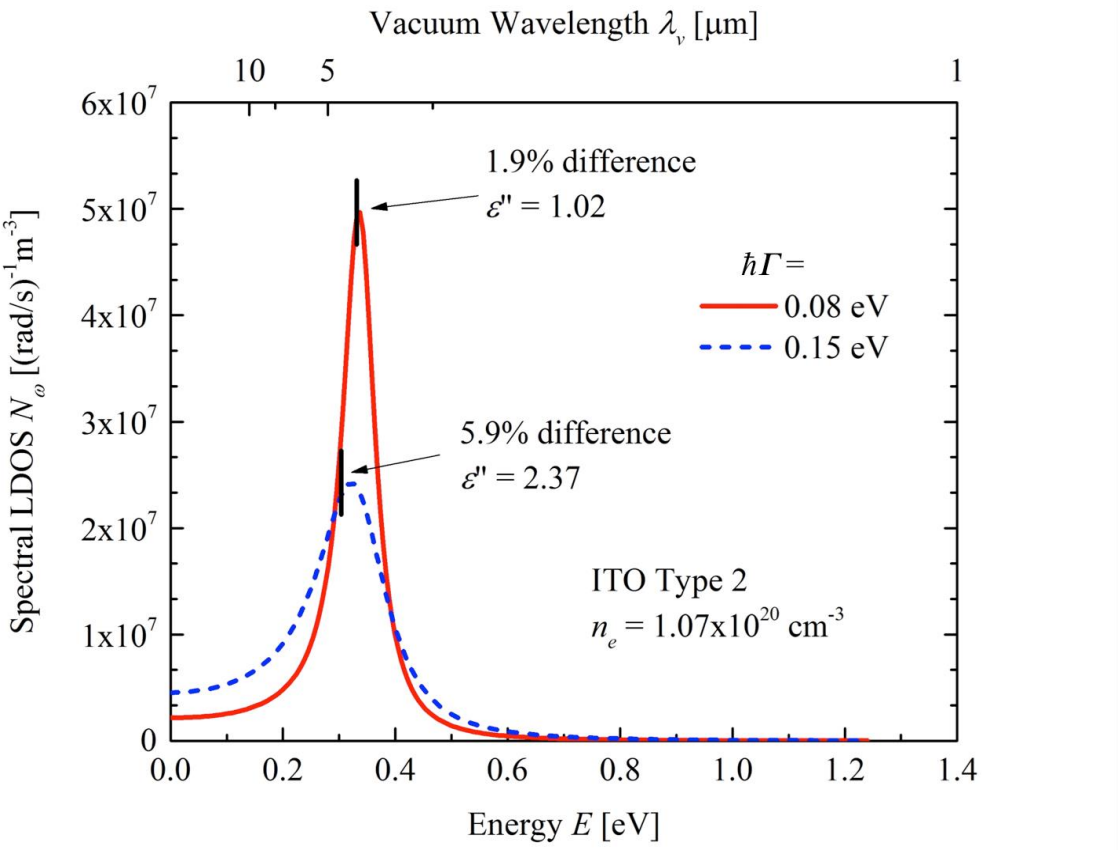

Figure 5.6. ITO Type 2 spectral LDOS (integrated over all tangential wavevectors). The black curve indicates the distribution of ITO Type 2 ($\hbar\Gamma$ = 0.07 eV); the other for $\hbar\Gamma$ = 0.15 eV. The scribe marks align with the predicted resonances for each of the respective $\hbar\Gamma$ values. Percent differences between the predicted resonances and LDOS maxima are indicated as well as the corresponding ε'' values.

deemed as not exhibiting a significant SPP resonance in the NIR.

5.4 Conclusions

The tailorability of the near-field thermal radiative properties of ITO is quantified. A sensitivity analysis is performed to measure the effect of fabrication process sensitive electromagnetic properties – plasma frequency, damping coefficient, and infinite permittivity – on the spectral locations of SPP resonances. The sensitivity analysis demonstrates that the electronic doping level has the most significant effect on resonance frequencies by nearly an order of magnitude.

Based on the results of the sensitivity analysis, two ITO configurations are selected to examine the corresponding near-field physics. To confirm resonance conditions, LDOS and SPP dispersion relation analyses are performed on these ITO configurations. A definition is established for "significant" SPP resonance and a significant NIR resonance frequency is found with ITO Type 1 (where $n_e = 4.5\times10^{20}$ cm^{-3}) at $\hbar\omega_p = 0.65$ eV. ITO Type 2 (where $n_e = 1.2\times10^{20}$ cm^{-3}) exhibits an insignificant resonance at $\hbar\omega_p = 0.34$ eV. The demonstrated ITO Type 1 NIR SPP resonance at 0.65 eV dominates the energy density spectral distribution at 1400 K.

The results presented herein show that the near-field radiative properties of ITO may be engineered by specifying the fabrication process. According to the Drude model, process sensitive electromagnetic properties, such as plasma frequency, damping coefficient, and infinite permittivity, drive the ITO radiative properties. Since these fabrication processes, and the corresponding electromagnetic properties, have previously been demonstrated, NIR monochromatic energy transfer is available at temperatures as low as 1400 K.

5.5 References

[1] J. Baxter, Z. Bian, G. Chen, D. Danielson, M.S. Dresselhaus, A.G. Fedorov, T.S. Fisher, C.W. Jones, E. Maginn, U. Kortshagen, A. Manthiram, A. Nozik, D.R. Rolison, T. Sands, L. Shi, S. Sholl, and Y. Wu, Energy Environ. Sci. **2** 559 (2009).

[2] T. Bauer, *Thermophotovoltaics: Basic Principles and Critical Aspects of System Design* (Springer, Berlin, 2009).

[3] K. Joulain, J.-P. Mulet, F. Marquier, R. Carminati, and J.-J. Greffet, Surf. Sci. Rep. **57** 59 (2005).

[4] Z.M. Zhang, *Nano/microscale Heat Transfer* (McGraw-Hill, New York, 2007).

[5] I. Hu, A. Narayanaswamy, X. Chen, and G. Chen, Appl. Phys. Lett. **92** 133106 (2008).

[6] S. Basu, Z.M. Zhang, and C.J. Fu, I. J. Energ. Res. **33** 1203 (2009).

[7] E. Rousseau, A. Siria, G. Jourdan, S. Volz, F. Comin, J. Chevrier, J.-J. Greffet, Nat. Photonics **3** 514 (2009).

[8] S. Shen, A. Narayanaswamy, and G. Chen, Nano Lett. **9** 2909 (2009).

[9] J.R. Howel, M.P. Mengüç, and R. Siegel, *Thermal Radiation Heat Transfer*, 6th ed. (CRC Press, Boca Raton, 2015).

[10] R.S. Ottens, V. Quetschke, W. Wise, A.A. Alemi, R. Lundock, G. Mueller, H. Reitze, D.B. Tanner, and B.F. Whiting, Phys. Rev. Lett. **107** 014301 (2011).

[11] S. Shen, A. Mavrokefalos, P. Sambegoro, and G. Chen, Appl. Phys. Lett. **100** 133114 (2012).

[12] J.-P. Mulet, K. Joulain, R. Carminati, and J.-J. Greffet, Microscale Therm. Eng. **6** 209 (2002).

[13] S. Basu, B.J. Lee, and Z.M. Zhang, J. Heat Transf. **132** 023302 (2010).

[14] M.D. Whale, *A Fluctuational Electrodynamics Analysis of Microscale Radiative Heat Transfer and the Design of Microscale Thermophotovoltaic Devices*, PhD Thesis (Massachusetts Institute of Technology, Cambridge, 1997).

[15] M.D. Whale and E.G. Cravalho, IEEE T. Energy Conver. **17** 130 (2002).

[16] A. Narayanaswamy and G. Chen, Appl. Phys. Lett. **82** 3544 (2003).

[17] M. Laroche, R. Carminati, and J.-J. Greffet, J. Appl. Phys. **100** 063704 (2006).

[18] K. Park, S. Basu, W.P. King, and Z.M. Zhang, J. Quant. Spectrosc. Ra. **109** 305

(2008).

[19] M. Francoeur, R. Vaillon, and M.P. Mengüç, IEEE T. Energy Conver. **26** 686 (2011).

[20] O. Ilic, M. Jablan, J.D. Joannopoulos, I. Celanovic, and M. Soljačić, Opt. Express **20** A366 (2012).

[21] M.P. Bernardi, O. Dupré, E. Blandre, P.-O. Chapuis, R. Vaillon, and M. Francoeur, Sci. Rep. **5** (2015).

[22] R.S. DiMatteo, P. Greiff, S.L. Finberg, K.A. Young-Waithe, H.K.H. Choy, M.M. Masaki, and C.G. Fonstad, Appl. Phys. Lett. **79** 1894 (2001).

[23] R.S. DiMatteo, P. Greiff, D. Seltzer, G. Meulenber, E. Brown, E. Carlen, K. Kaiser, S. Finberg, H. Nguyen, J. Azarkevich, P. Baldasero, J. Beausang, L. Danielson, M. Dashiell, D. DePoy, H. Ehsani, W. Topper, and K. Rahner, Proceedings of the 5th Conference on Thermophotovoltaic Generation of Electricity 232 (2003).

[24] K. Hanamura, and K. Mori, Proceedings of the ASME/JSME 2011 8th Thermal Engineering Joint Conference, 457 (2011).

[25] O. Ilic, M. Jablan, J.D. Joannopoulos, I. Celanovic, H. Buljan, and M. Soljačić, Phys. Rev. B **85** 155422 (2012).

[26] S.-A. Biehs, D. Reddig, and M. Holthaus, Eur. Phys. J. B **55** 237 (2007).

[27] K. Joulain, and C. Henkel, Appl. Phys. B **93** 151 (2008).

[28] P. Ben-Abdallah, K. Joulain, J. Drevillon, and G. Domingues, J. Appl. Phys. **106** 044306 (2009).

[29] P. Ben-Abdallah, K. Joulain, J. Drevillon, and G. Domingues, Appl. Phys. Lett. **94** 15117 (2009).

[30] M. Francoeur, M.P. Mengüç, and R. Vaillon, Appl. Phys. Lett. **93** 143109 (2008).

[31] M. Francoeur, M.P. Mengüç, and R. Vaillon, J. Appl. Phys. **107** 034313 (2010).

[32] M. Francoeur, M.P. Mengüç, and R. Vaillon, J. Phys. D Appl. Phys. **43** 075501 (2010).

[33] C.J. Fu, and W.C. Tan, J. Quant. Spectrosc. Ra. **110** 1027 (2009).

[34] A.W. Rodríguez, O. Ilic, P. Bermel, I. Celanovic, J.D. Joannopoulos, M. Soljačić, and S.G. Johnson, Phys. Rev. Lett. **107** 114302 (2011).

[35] V.G. Veselago, Sov. Phys. Usp. **10** 509 (1968).

[36] W. Cai, and V. Shalaev, Optical Metamaterials: Fundamentals and Applications (Springer, New York, 2010).

[37] S.J. Petersen, S. Basu, B. Raeymaekers, and M. Francoeur, J. Quant. Spectrosc. Ra. **129** 277 (2013).

[38] P.R. West, S. Ishii, G.V. Naik, N.K. Emani, V.M. Shalaev, and A. Boltasseva, Laser Photon. Rev. **4** 795 (2010).

[39] J.C.C. Fan, and F.J. Bachner, J. Electrochem. Soc. **122** 1719 (1975).

[40] Y. Ohhata, and S. Yoshida, Jpn. J. Appl. Phys. **46** 43 (1977).

[41] S. Yoshida, Appl. Optics **17** 145 (1978).

[42] Y. Ohhata, F. Shinoki, and S. Yoshida, Thin Solid Films **59** 255 (1979).

[43] I. Hamberg and C.G. Granqvist, J. Appl. Phys. **60** R123 (1986).

[44] S.H. Brewer and S. Franzen, J. Phys. Chem. B **106** 12986 (2002).

[45] A. Solieman and M.A. Aegerter, Thin Solid Films **502** 205 (2006).

[46] C. Rhodes, S. Franzen, J.-P. Maria, M. Losego, D.N. Leonard, B. Laughlin, G. Duscher, and S. Weibel, J. Appl. Phys. **100** 054905 (2006).

[47] C. Rhodes, M. Cerutti, A. Efremenko, M. Losego, D.E. Aspnes, J.-P. Maria, and S. Franzen, J. Appl. Phys. **103** 093108 (2008).

[48] F. Michelotti, L. Dominici, E. Descrovi, N. Danz, and F. Menchini, Opt. Lett. **34** 839 (2009).

[49] R.J. Mendelsberg, G. García, and D.J. Milliron, J. Appl. Phys. **111** 063515 (2012).

[50] S.H. Brewer and S. Franzen, Chem. Phys. **300** 285 (2004).

[51] S. Franzen, J. Phys. Chem. C **112** 6027 (2008).

[52] K Joulain, R. Carminati, J.-P. Mulet, and J-J. Greffet, Phys. Rev. B **68** 245405 (2003).

[53] S.J. Petersen, S. Basu, and M. Francoeur, Photonic. Nanostruct. **11** 167 (2013).

[54] G.E. Box, H.G. Hunter, and J.S. Hunter, *Statistics for Experimenters* (John Wiley and Sons, Toronto, 1978).

CHAPTER 6

CONCLUSIONS

The following were the objectives for this dissertation:

1. Dielectric Mie resonance-based (DMRB) metamaterials are theoretically analyzed. They exhibit surface polariton (SP) resonance in the near infrared (NIR), making them viable candidates as an emission source for nanoscale gap thermophotovoltaic (nano-TPV) devices.

2. Three-dimensional DMRB metamaterial specimens are fabricated and characterized. Spectral transmission characterization results do not agree with predictions. Geometric characterization suggests that the nanoparticles are not sufficiently dispersed.

3. A second class of material, indium tin oxide (ITO), is explored theoretically as another candidate emission source for nano-TPV devices, also exhibiting SP resonance in the NIR. Therefore, ITO is another good candidate for an emission source in nano-TPV devices.

6.1 Exploration of DMRB Metamaterials as Candidate Emission Sources in Nano-TPV Power Generation

6.1.1 Summary

To date, heat transfer analyses have been employed for assessing the potential of a material for use as an emission source in nano-TPV devices [1–5]. However, heat transfer depends heavily on the material properties of both the emission source and the receiver.

The local density of electromagnetic states (LDOS) represents the potential harvestable energy from a surface [6–10], independent of the receiving material, and a spectral analysis thereof may reveal whether transverse electric and/or transverse magnetic SPs can be supported. In Chapter 2, LDOS was quantified for a silicon carbide (SiC) DMRB metamaterial. The metamaterial consisted of 2-μm SiC spheres within a potassium bromide host medium, where the spheres were spaced such that the volume filling fraction was 0.4. Clausius-Mossotti mixing relations, in concert with Mie scattering coefficients, were employed to model the effective medium properties of this metamaterial, effectively transforming this composite matrix into a uniform, homogeneous medium.

A spectral LDOS analysis revealed that the SiC metamaterial could sustain SPs in both transverse electric and transverse magnetic polarization. However, the predicted resonance of these SPs occurred outside the NIR bandwidth at vacuum wavelengths of 11.1 and 13.2 μm, eliminating the SiC DMRB metamaterial as a candidate for use in nano-TPV devices.

In Chapter 3, LDOS analyses, similar to those discussed in Chapter 2, were conducted on another DMRB metamaterial. Therein, metamaterials consisting of silicon (Si) spheres within a dielectric host medium were explored. A sensitivity analysis was performed to quantify the effect of three metamaterial configuration parameters – host permittivity, volume filling fraction, and particle radius – on the predicted effective SP resonances (for both transverse magnetic and transverse electric polarizations).

The analysis showed that Si DMRB metamaterials are expected to exhibit SP resonance frequencies in the NIR, making them viable candidate emission sources for

nano-TPV devices. It was shown that, of the three parameters explored, particle radius had the greatest effect on SP resonance frequencies, an indication of the tunability of the electric response of DMRB metamaterials. And finally, it was concluded that the effective medium theory employed in Chapters 2 and 3 is questionable for DMRB metamaterial near-field calculations since the distance from the emitting bulk at which the LDOS was calculated is on the same order as the general dimensions of the repeating unit structures within the metamaterials [11–13].

6.1.2 Recommendations

As described above, the Clausius-Mossotti mixing relations, in concert with the Mie scattering coefficients, were employed as an effective medium theory for DMRB metamaterial predictions. It was also mentioned that the effective medium theory is nonideal for these predictions since the distance from the emitting bulk at which the LDOS was calculated is similar to the dimensions of the meta-atoms within the metamaterials. However, it is certain that a resonance must occur in these metamaterials, in the least, due to Mie scattering. Therefore, it is proposed that further analyses be pursued, similar to those described in Chapters 2 and 3, in which near-field thermal emission is directly calculated without using effective medium theory such as References 11 and 14.

To more firmly validate the effective medium results discussed above, it is imperative that DMRB metamaterials be fabricated and characterized, which is the topic of the following section.

6.2 Fabrication of 3D Macroscale DMRB Metamaterials

6.2.1 Summary

Researchers have successfully fabricated and characterized DMRB metamaterials in a number of planar configurations [15–18], in which metamaterial constituent dimensions in only two principle directions are of the same order of magnitude.

Wheeler et al. [19] were the first to fabricate a 3D macroscale DMRB metamaterial. They successfully fabricated and characterized metamaterials consisting of SiC particles in a potassium bromide host medium. Wheeler et al. characterized the diffuse reflectance of their specimens with a Fourier transform (FTIR) spectrometer, showing good agreement with predicted dipole resonance frequencies. However, a limited number of material types are compatible with the fabrication process they followed.

In Chapter 4, the evolution of a 3D macroscale DMRB metamaterial fabrication process was described. Particles of various shapes, sizes, and material were hand mixed with various two part epoxies. Metamaterial configurations – combinations of particle size, material, and spacing and host material – were preselected according to Equation (2.10) from such that measureable reductions in NIR transmission were predicted. Transmission measurements obtained with a spectrophotometer disagreed with predicted values, suggesting that the specimens were inadequately prepared. Another series of specimens were fabricated, consisting of silicon particles in a two-part epoxy, cured in plastic molds for smoother surfaces and with an added sonication step to mitigate particle agglomeration. Spectrophotometer transmission measurements were still contradictory to predictions. For further validation of the spectrophotometer results, NIR transmission data were also measured with an FTIR spectrometer. The FTIR results were similar to

those of the spectrophotometer, showing little agreement with the predicted spectra. It was hypothesized that the particles were not being sufficiently dispersed.

Focusing on the particle dispersion, fish oil [20] and methanol were added as surfactants to silicon particle mixtures. Scanning electron microscopy revealed that neither the particle dispersion nor the particle spacing were sufficient to mimic the preselected metamaterial configurations mentioned above.

6.2.2 Recommendations

It is proposed that a trade analysis be conducted to ascertain whether dispersing particles in a host medium, which is conducive of metamaterial configurations predicted to exhibit SP resonance in the NIR, is practical:

1. A thorough literature review of the chemistry related to particle dispersion should be conducted. The mechanics of particle dispersion should be deeply understood.
2. A comprehensive list of nanoparticles should be formed – both commercially available and manufacturable – that will support NIR Mie resonance and that may be successfully dispersed in adequate host media.
3. A comprehensive list of adequate host media in which nanoparticles from 2 may be dispersed and that exhibit the electric permittivities that will help facilitate NIR SP resonance from the resulting metamaterial.
4. Using results from 1–3, it should be determined whether the metamaterial fabrication approach outlined in Chapter 4 is practical.

If it is determined that fabricating DMRB metamaterials in this manner is practical, it is proposed that specimens be manufactured and characterized, both geometrically and spectrally, to validate predictions from the effective medium theory results discussed in

Chapters 2 and 3.

6.3 Exploration of ITO as Candidate Emission Source in Nano-TPV Power Generation

6.3.1 Summary

In the wake of unsuccessfully fabricating and characterizing a DMRB metamaterial, Chapter 5 explored the potential of indium tin oxide as a candidate emission source for nano-TPV devices [21]. Analyses similar to those conducted in Chapters 2 and 3 were detailed, with the primary difference being the material model. Instead of Clausius-Mossotti mixing relations and Mie coefficients to determine effective permittivity and permeability, empirically determined correlations between manufacturing process driven parameters, e.g., damping coefficient, infinite permittivity, and electronic doping level, and the electromagnetic response of ITO were employed [22–26]. A sensitivity analysis was performed, similar to that described in Chapter 3, indicating that the electronic doping level has the greatest effect on SP resonance frequencies in ITO. SP resonance frequencies were predicted to occur within the NIR.

6.3.2 DMRB metamaterials vs. ITO

From Chapter 3, silicon DMRB metamaterials were predicted to exhibit SP resonance between 1.1 and 1.7 μm, while – from Chapter 5 – ITO did so between 1.9 and 3.6 μm, both ranges being within the NIR bandwidth. Energy density analyses showed that the resonances within the DMRB metamaterial can be thermally activated at temperatures as low as 800 K, with those within ITO as low as 1400 K, making the DMRB metamaterial more accessible as a nano-TPV system emission source. In spite of this advantage of DMRB metamaterials over ITO, the uncertainty of the effective

medium theory and the inconclusive experimental results (Chapter 4) reduce confidence in conclusions made regarding the DMRB metamaterials.

6.3.3 Recommendations

It is proposed that ITO specimens be fabricated with the parameters described above, which resulted in predicted SP resonance occurring within the NIR spectral band. Then, to validate predictions reported in Chapter 5, specimens could be characterized by measuring the near-field heat flux using the method described by Bernardi [21].

6.4 References

[1] K. Joulain, J. Drevillon, and P. Ben-Abdallah, Phys. Rev. B **81** 165119 (2010).

[2] Z. Zheng and Y. Xuan, Int. J. Heat Mass Tran. **54** 1101 (2011).

[3] Z. Zheng and Y. Xuan, Chinese Sci. Bull. **56** 2312 (2011).

[4] S. Basu and M. Francoeur, Appl. Phys. Lett. **99** 143107 (2011).

[5] M. Francoeur, S. Basu, and S.J. Petersen, Opt. Express **19** 18774 (2011).

[6] K. Joulain, R. Carminati, J.-P. Mulet, and J.-J. Greffet, Phys. Rev. B **68** 245405 (2003).

[7] S. Basu, B.J. Lee, and Z.M. Zhang, J. Heat Transf. **132** 023302 (2010).

[8] M. Francoeur, M.P. Mengüç, and R. Vaillon, J. Appl. Phys. **107** 034313 (2010).

[9] M. Francoeur, M.P. Mengüç, and R. Vaillon, Appl. Phys. A-Mater. **103** 547 (2011).

[10] M. Tschikin, S.A. Biehs, R. Messina, and P. Ben-Abdallah, J. Opt. **15** 105101 (2013).

[11] B. Liu and S. Shen, Phys. Rev. B **87** 115403 (2013).

[12] X.L. Liu, T.J. Bright, and Z.M. Zhang, J. Heat Transf. **136** 092703 (2014).

[13] A. Didari and M.P. Mengüç, Opt. Express **23** A547 (2015).

[14] S. Edalatpour, M. Čuma, T. Trueax, R. Backman, and M. Francoeur, Phys. Rev. E **91** 063307 (2015).

[15] J. Valentine, J. Li, T. Zentgraf, G. Bartal, and X. Zhang, Nat. Mater. **8** 568 (2009).

[16] J.C. Ginn, I. Brener, D.W. Peters, J.R. Wendt, J.O. Stevens, P.F. Hines, L.I. Basilio, L.K. Warne, J.F. Ihlefeld, P.G. Clem, and M.B. Sinclair, Phys. Rev. Lett. **108** 097402 (2012).

[17] S. Liu, J.F. Ihlefeld, J. Domínguez, E.F. Gonzales, J.E. Bower, D.B. Burckel, M.B. Sinclair, I. and Brener, Appl. Phys. Lett. **102** 161905 (2013).

[18] P. Moitra, B.A. Slovick, Z.G. Yu, S. Krishnamurthy, and J. Valentine, Appl. Phys. Lett. **104** 171102 (2014).

[19] M.S. Wheeler, J.S. Aitchison, J.I.L. Chen, G.A. Ozin, and M. Mojahedi, Phys. Rev. B **79** 073103 (2009).

[20] A. Reindl, A. Voronov, P.K. Gorle, M. Rauscher, A. Roosen, and W. Peukert, Colloid. Surface. **320** 183 (2008).

[21] P.R. West, S. Ishii, G.V. Naik, N.K. Emani, V.M. Shalaev, and A. Boltasseva, Laser Photon. Rev. **4** 795 (2010).

[22] S.H. Brewer and S. Franzen, J. Phys. Chem. B **106** 12986 (2002).

[23] A. Solieman and M.A. Aegerter, Thin Solid Films **502** 205 (2006).

[24] C. Rhodes, S. Franzen, J.-P. Maria, M. Losego, D.N. Leonard, B. Laughlin, G. Duscher, and S. Weibel, J. Appl. Phys. **100** 054905 (2006).

[25] C. Rhodes, M. Cerutti, A. Efremenko, M. Losego, D.E. Aspnes, J.-P. Maria, and S. Franzen, J. Appl. Phys. **103** 093108 (2008).

[26] F. Michelotti, L. Dominici, E. Descrovi, N. Danz, and F. Menchini, Opt. Lett. **34** 839 (2009).

[27] M.P. Bernardi, *Numerical and experimental techniques for enhanced power generation in a nanoscale gap thermophotovoltaic device*, PhD dissertation, University of Utah, Salt Lake City, 2016.